April 2014

Self-Assembly of Block Copolymers for the Fabrication of Functional Nanomaterials

Li Yao
University of Massachusetts - Amherst

SELF-ASSEMBLY OF BLOCK COPOLYMERS FOR THE FABRICATION OF FUNCTIONAL NANOMATERIALS

A Dissertation Presented

by

LI YAO

Submitted to the Graduate School of the
University of Massachusetts Amherst in partial fulfillment
of the requirements for the degree of

DOCTOR OF PHILOSOPHY

February 2014

Department of Polymer Science and Engineering

SELF-ASSEMBLY OF BLOCK COPOLYMERS FOR THE FABRICATION OF FUNCTIONAL NANOMATERIALS

A Dissertation Presented

by

LI YAO

Approved as to style and content by:

James J. Watkins, Chair

Thomas J. McCarthy, Member

Jonathan P. Rothstein, Member

D. A. Hoagland, Department Head
Department of Polymer Science and Engineering

ACKNOWLEDGMENTS

The past five years in the Polymer Science and Engineering Program at UMass Amherst affected me in a variety of ways. I have developed myself from a student who only knew how to learn from teachers in class into a researcher who is becoming an independent scientist. I also improved my communication skills including both oral and written abilities. I enjoyed my time at UMass with the easy-going atmosphere and active academic collaboration.

I thank my research advisor Professor James Watkins. I especially thank him for giving me a lot of freedom in conducting research. At the same time, he always pointed out the right direction for my research and gave me many valuable suggestions. He encouraged me to do a good job rather than demanding results, and he supported my research by providing tremendous resources. He also motivated me with his ability to foster creativity, sharp insight in figuring out a solution for a problem, and excellent leadership skills. I feel very lucky to have had Professor Watkins as my research advisor.

I thank my dissertation committee members, Professor Thomas McCarthy and Professor Jonathan Rothstein for their time and valuable feedback about my research and proposals throughout my PhD journey. I particularly thank Professor Thomas McCarthy for giving me valuable career suggestions and support.

I also thank my collaborators. Without their contribution, a lot of achievements during my PhD could not have been accomplished. First, I thank Dr. Arthur Woll from Cornell University for his discussions and help during my GISAXS measurements at the Cornell High Energy Synchrotron Source. I thank Dr. Xinran Liu from Yale University and Dr. Alex Ribbe from UMass Amherst for their discussions and help with the 3D TEM tomography. I thank Professor Samual Gido for the discussions about gyroid morphology and helical superstructures. I also thank Professor Sam Nugen and Jeff Grimes for the collaboration in microfluidic device fabrication.

I would like to thank Dr. Ying Lin for her time and effort on the project of ultrahigh loading of nanoparticles in polymer additive composites. I thank Nicholas Colella for his help with my writing. I also thank Dr. Vikram Daga for the discussions about the effect of base quencher in lithography resolution improvement. I thank Dr. John

Ell for his time and effort spent teaching me synthesis via atom transfer radical polymerization. I also thank Dr. Nicholas Hendricks, Todd Crosby, Dr. Eunyoung You for the time spent teaching me to use high pressure instruments. I thank Cheng Li for the assistance with GISAXS measurements, Eric Anderson for the assistance with cryo-microtoming, Dr. Curran Chandler for AFM skills, and Dr. Jacob John for RIE. I especially thank Dr. Michael Beaulieu, Dr. Yuying Tang, Dr. Qingshuo Wei, Dr. Guanghao Lu, Dr. Dongpo Song, and Rohit Kothari for the discussions and encouragement during my PhD. I also thank all the other Watkins group members during my time at UMass, Dr. Chris Ziegler, Dr. Dan Miranda, Dr. Alvin Romang, Dr. David Mesguich, Dr. Hao Zhang, Glen Wang, Xue Cai, Yuanlong Zhao, Dr. Gang Qian, Dr. Hongtao Zhang, Takayuki Kobayashi, Dr. Jayanta Baral, Shengkai Li, Brenda Warren, Professor Masashi Haruki, Irene Howell, Feyza Dundar, Yue Gai, and Jacobo Morere Rodriguez.

I would like to thank the Center of Hierarchical Manufacturing at UMass Amherst, a NSF center (CMMI-1025020), for the financial support for my graduate research, the Materials Research Science and Engineering Center (MRSEC) at the UMass Amherst for AFM, SAXS, WAXS, TEM, XRD, DSC, TGA, GPC, NMR, and IR facilities and the Cornell High Energy Synchrotron Source (CHESS) for GISAXS measurements. In particular, I thank Dr. Sekar Thirunavukkarasu for his assistance with AFM, SAXS, WAXS, XRD. I also thank Mr. Louis Raboin for his assistance with TEM and cryo-microtoming. I thank Mr. John Nicholson for his assistance with RIE and mask-aligner.

I would like to thank our current group secretary, Ms. Jo-Ann Bourguignon, for her excellent job in assisting the group with purchasing, scheduling, and financial issues. I also thank our former group secretaries, Ms. Trouble Erin Mandeson and Ms. Barbara Bou for their hard work. I thank our department graduate program manager, Ms. Lisa Groth, for her great job in assisting the department with issues about graduation, defense scheduling, seminars, job information, *etc.* I also thank Ms. Maria Farrington, Ms. Alyssa Kristek, *et al.* for their help during my time at UMass.

I wish to thank all our first year teachers, Professor Murugappan Muthukumar, Professor Bryan Coughlin, Professor Ryan Hayward, Professor Harry Bermudez, Professor Thomas McCarthy, Professor Samual Gido, *et al.* I built my strong knowledge

background in polymer science and engineering because of their hard work. I also appreciate the process of taking the cumulative exam, which is a great strategy to force us to learn more. I also thank all my classmates, Tsunghan Tsai, Lang Chen, Weiyin Gu, Glen Wang, Dayong Chen, Yu Gu, Henry Yang, Feng Liu, Xiaodan Gu, Packy Chantarak, Samantha McRae, Anika Reuter, Michael Lis, Mike Bartlett, Caroline Miesch, Sunzida Ferdous, *et al.* for their help and company through the past five years.

I wish to thank members of the running club (BEN) in Boston. With their encouragement, I consistently bettered myself and successfully finished my first marathon in 2012. The persistence and the ambition to never give up, which are generated through running, supported me in successfully going through my PhD journey and drove me to achieve my research.

Finally, I wish to thank my parents who always support me in various ways, especially encouraging me to overcome any difficulties. Only with their support and comfort was I able to go through challenging times, accomplish my dissertation, and achieve my PhD.

ABSTRACT

SELF-ASSEMBLY OF BLOCK COPOLYMERS FOR THE FABRICATION OF FUNCTIONAL NANOMATERIALS

FEBRUARY 2014

LI YAO, B.S., NANJING UNIVERSITY

M.S., BOSTON COLLEGE

PH.D., UNIVERSITY OF MASSACHUSETTS AMHERST

Directed by: Professor James J. Watkins

This dissertation explores the use of block copolymers which can self-assemble into different morphologies as templates to fabricate nanostructured materials. The first section (Chapters 2-4) reports the formation of mesoporous silica films with spherical, cylindrical and bicontinuous pores up to 40 nm in diameter through replicating the morphologies of the solid block copolymer (BCP) templates, polystyrene-*b*-poly(*tert*-butyl acrylate) (PS-*b*-PtBA), via phase selective condensation of tetraethylorthosilicate in supercritical CO_2. Next, directed self-assembly was used to control the orientation of cylindrical domains in PS-*b*-PtBA templates. Large-area aligned mesochannels in silica films with diameters tunable between 5 and 30 nm were achieved through the replication of oriented templates via $scCO_2$ infusion. The long-range alignment of mesochannels was confirmed through GISAXS with sample stage azimuthal rotation.

In the second section (Chapters 5-6), enantiopure tartaric acid was used as an additive to dramatically improve ordering in poly(ethylene oxide-block-*tert*-butyl acrylate) (PEO-*b*-PtBA) copolymers. Transmission electron microscopy (TEM), atomic

force microscopy (AFM) and X-ray scattering were used to study the phase behavior and morphologies within both bulk and thin films. With the addition of a photo acid generator, photo-induced disorder in the PEO-*b*-PtBA/tartaric acid composite system was achieved upon UV exposure which deprotected the PtBA block to yield poly(acrylic acid) (PAA), which is phase-miscible with PEO. Area-selective UV exposure using a photo-mask was applied with the assistance of trace amounts of base quencher to achieve high-resolution hierarchical patterns. Helical superstructures were observed by TEM in this BCP/chiral additive system with 3D handedness confirmed by TEM tomography.

In the last section (Chapter 7), ultra-high loadings of nanoparticles into target domains of block copolymer composites were achieved by blending the block copolymer hosts with small molecule additives that exhibit strong interactions with one of the polymer chain segments and with the nanoparticle ligands via hydrogen bonding. The addition of 40 wt% D-tartaric acid to poly(ethylene oxide-block-*tert*-butyl acrylate) (PEO-*b*-PtBA) enabled the loading of up to 150 wt% of 4-hydroxythiophenol functionalized Au nanoparticles relative to the mass of the target hydrophilic domain. This was equivalent to over 40% Au by mass of the resulting well ordered composite as measured by thermal gravimetric analysis.

TABLE OF CONTENTS

LIST OF TABLES

Table Page

LIST OF FIGURES

Figure Page

CHAPTER 1

INTRODUCTION AND OVERVIEW

1.1 Introduction

Block copolymer (BCP) self-assembly has emerged in recent years as a very attractive method for the fabrication of functional nanostructured materials[1-4] and also for the development of next-generation lithography[5-8] for the semiconductor industry. By tuning the number of repeat units (N), the segment-segment interaction parameter, known as the Flory-Huggins parameter (χ), and volume fraction (f) of each segment, BCPs can be designed such that they self-assemble into well-ordered periodic morphologies with domain sizes typically on the order of 5 to 30 nm.[9] Long range order and preferred orientation of the domains can further be realized through the use of solvent vapor annealing,[10-16] external fields,[17-20] directed self-assembly[21-31] and/or interfacial interactions.[32-36]

Using the BCP polystyrene-*b*-poly(*tert*-butyl acrylate) (PS-*b*-PtBA) as the templates, mesoporous silica films with cylindrical or spherical pores up to 40 nm in diameter were fabricated. The replication process involves the CO_2-assisted infusion and phase selective condensation of tetraethylorthosilicate within the polymer template. The template structures, including domain packing, orientation and spacing can be controlled by adjusting the molecular weight, volume fraction and polydispersities of the block copolymers and by solvent annealing. This approach separates the template organization away from silica network condensation, making it a better-defined approach compared to those that involve cooperative assembly with simultaneous silica network condensation

for ordering control. The structural details imparted to the template prior to precursor infusion can be well retained in the mesoporous films. Additionally, all of the tricks that have been developed for block copolymer self-assembly can be easily transplanted into rigid metal oxide films. In one example, massively aligned mesochannels were fabricated for applications in microfluidic or molecular-scale devices through the replication of the well aligned PS-*b*-PtBA templates. Directed self-assembly (DSA) using periodic patterns was used to achieve the long-range alignment of the cylinders in PS-*b*-PtBA templates, which were then replicated to yield massively parallel arrays of cylindrical pores with pore diameters up to ~ 20 nm. The ability to tune pore sizes in this range within aligned nanochannels is particularly attractive for applications involving bio-molecules. In another example, PS-*b*-PtBA templates with a double gyroid morphology, which is accessible by tuning the molecular weight and volume fraction, were used as the template to fabricate silica films with bicontinuous mesochannels. This special structure provides permeable channels for molecular separation without the additional alignment step that is necessary for cylindrical morphologies.

Additive driven self-assembly has been used to enhance the microphase separation of BCP systems. The selective interaction between the additive and one of the block copolymer segments can significantly enhance the segregation strength of the BCP. For example,[37-38] a homopolymer, poly(acrylic acid) (PAA), has been used as an additive which interacts with polyethylene oxide blocks using hydrogen bonding to achieve ordered structures with ultra-small domain size (~ 5 nm). Small functional molecules[39-40] or nanoparticles[41] can also interact preferentially with one of the blocks to induce order in

otherwise disordered BCPs. Various applications can be achieved based on the composite materials generated through this approach.

In one example, sub-micron patterns of adjacent, well-ordered and disordered domains were obtained using optical lithography by area-selective, photo-induced disordering transitions within block copolymer composite films. Enantiopure tartaric acid was blended with poly(ethylene oxide-block-*tert*-butyl acrylate) (PEO-*b*-PtBA) copolymers to yield well-ordered films. In the presence of triphenylsulfonium triflate, a photo-acid generator, photo-induced disorder was achieved upon UV-exposure by deprotection of the PtBA block to yield poly(acrylic acid). Poly(acrylic acid) is compatible with both PEO and tartaric acid and de-protection yielded a phase-mixed material and disorder within seconds. Tartaric acid performs two additional functions in this system. First, it increases segregation strength in PEO-*b*-PtBA, enabling well-ordered systems at low BCP molecular weights with small domain sizes and rapid disordering kinetics. Second, the presence of tartaric acid suppresses PEO crystallization, resulting in smooth films and eliminating the influence of PEO crystallization on film morphology.

Through additive driven self-assembly, helical superstructures were achieved in achiral diblock copolymer (BCP) bulk systems by the addition of enantiopure tartaric acid. Previous research on helical superstructures is based on using chiral block copolymers, for example poly(styrene)-*b*-poly(L-lactide) (PS-*b*-PLLA),[42-43] or using the triblock terpolymer, polystyrene-*b*-polybutadiene-*b*-poly(methyl methacrylate) (SBM),[44] to achieve the helical morphology in the bulk system. Complicated BCP synthesis and specific requirement of the BCP segments limits the versatility of the functional blocks used in these approaches. In the new system presented here, the hydrogen bonding

between tartaric acid and polyethylene oxide (PEO) block not only enhances the phase-separation of PEO-based block copolymer but also transfers the chiral information from the additive to the achiral backbone through the Domino effect. The helical phase was formed in the final composite bulk system after thermal annealing. As confirmed *via* transmission electron microscopy measurements, the handedness of helices can be easily tuned through blending the appropriate enantio-isomers of tartaric acids.

Additive driven self-assembly using small molecule additives also proved to be an efficient method to produce well ordered organic/nanoparticle (NP) hybrid materials with over 40 wt% NP core content. By blending the block copolymer hosts with small molecule additives that exhibit strong interactions with one of the polymer chain segments and with the nanoparticle ligands *via* hydrogen bonding, phase selective, ultra-high loadings of nanoparticles into target domains of block copolymer composites were achieved. The additive, tartaric acid, performs three important roles. First, as evidenced by small angle X-ray scattering, it significantly increases the segregation strength of the block copolymer *via* selective interaction with the hydrophilic PEO block. Second, it expands the PEO block and enhances the number and strength of enthalpically favorable interactions between the nanoparticle ligands and the host domain. Finally it mitigates entropic penalties associated with NP incorporation within the target domain of the BCP composite.

1.2 Dissertation Overview

The dissertation includes eight chapters. Chapter 1 (present) is an introduction and overview of the dissertation. In Chapter 2, the fabrication of ultra large-pore mesoporous silica films by 3-D replication of well ordered PS-*b*-PtBA in supercritical

CO_2 is presented. Chapter 3 provides an approach for massively aligned channel formation in mesoporous silica films using the supercritical fluid infusion process, decoupling the long-range alignment generation through directed self-assembly from silica network formation. Chapter 4 introduces the formation of bicontinuous silica films by replicating the double gyroid morphology of PS-*b*-PtBA in $scCO_2$. In Chapter 5, a method to form submicron patterns of adjacent, well-ordered and disordered domains is presented. This method is based on area-selective, photo-induced disordering transitions within block copolymer composite films, which consists of the BCP PEO-*b*-PtBA and enantiopure tartaric acid as the additive. In Chapter 6, the formation of helical superstructures in achiral diblock copolymer bulk systems through blending chiral additives into the system is discussed. Chapter 7 explores the phase selective, ultra-high loading of nanoparticles into target domains of block copolymer composites by blending the block copolymer hosts with small molecule additives that exhibit strong interactions with one of the polymer chain segments and with the nanoparticle ligands *via* hydrogen bonding. Finally, Chapter 8 summarizes the work, and discusses future work and outlook.

CHAPTER 2

FABRICATION OF ULTRA LARGE-PORE MESOPOROUS SILICA FILMS BY 3-D REPLICATION OF TUNABLE BLOCK COPOLYMER ARCHITECTURES IN SUPERCRITICAL CARBON DIOXIDE

2.1 Introduction

Mesoporous metal oxide films with well defined pore structures are of interest for many applications including microelectronics,[45-49] photovoltaics,[50-53] separations,[54-55] catalysis,[56-58] absorption,[59-60] sensors,[61-62] and biomedicine.[63-65] For example, mesoporous silica films with closed pores fabricated through a sol-gel processing technique[49] shows low dielectric constants, which can be potentially used in microelectronics. Separation membranes were also fabricated based on ordered mesoporous and macroporous silica films.[55] Aida and coworkers[58] have used mesoporous silica as microreactor to synthesize crystalline linear polyethylene nanofibers. Due to dielectric response of mesoporous silica films to different gas-phase chemical species, Baskaran and coworkers[62] have built chemical sensors for water vapor and ammonia in air based on mesoporous silica films.

2.1.1 Methods in fabrication of mesoporous silica films

The utility of the films for a specific device is predicated on the ability to match the size, shape, orientation, and potentially the long range order of a pore structure to the specific needs of the application. To date several methods to produce well-ordered films using surfactants.[66-74] As shown in Figure 2.1, in 2000 Honma and coworkers reported using cetyltrimethylammonium (C16TMA)[73] as the surfactant to fabricate mesoporous silica films through co-assembly process on air/water interfaces. Cot and coworkers, in

2000, reported using alkyltrimethylammonium bromides[74] as surfactant and silicon alkoxides as silica precursors to form hexagonal mesoporous silica layers through a sol-gel process templating liquid crystal mesophase. In 2002, Stucky and Chmelka[66] also reported using Pluronic P123 as the strucuture-directing agents to fabricate well ordered mesostructured silica and titania films according to binary water/copolymer phase diagram. Those methods typically involve cooperative assembly and silica precursor condensation from aqueous or alcohol solution such that structure generation *via* self-assembly and silica network formation *via* precursor condensation occur simultaneously and are intimately linked. Consequently, the fabrication processes for films are often subject to kinetic constraints, which can complicate control of morphology during processing.

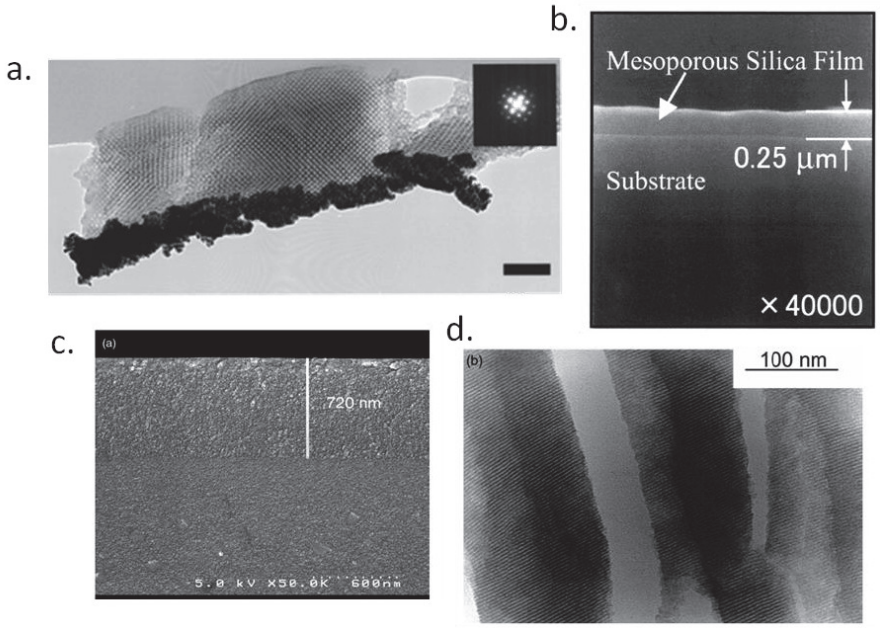

Figure 2.1 (a) TEM characterization of the cross-section of mesostructured silica films fabricated using Pluronic P123 as the strucuture-directing agents. Adapted from Ref.[66] (b) SEM image of the as-calinced mesoporous silica films fabricated through co-assembly process on air/water interfaces using cetyltrimethylammonium (C16TMA) as the surfactant. Adapted from Ref.[73] (c) SEM image and (d) TEM

image of the mesoporous silica film fabricated through so-gel process using alkyltrimethylammonium bromides as surfactant. Adapted from Ref.[74]

2.1.2 Mesoporous silica with ultra-large pores

As shown in Figure 2.1, low molecular weight surfactants were used in the mesoporous silica fabrication which typically yields relatively small (< 5 nm) pores. However, most of the biomelocules have the size up to hundreds of angstrom. Thus, metal oxide films with larger pores need to be designed and fabricated if biomedicine application needed. Recent reports indicate mesoporous materials with relatively large pore sizes can be prepared from solution using high molecular weight block copolymers[70, 75-78] swelling agents and/or discrete condensed objects[79] for surfactant or block copolymer templates. For example, as shown in Figure 2.2, the Chmelka and Stucky group[70] in 1998 fabricated mesoporous silica (SBA-15) with pore sizes up to 30 nm using amphiphilic PEO-PPO-PEO triblock copolymers as the structure directing agent in acidic condition. In 2007, Deng and coworkers applied evaporation-induced self-assembly (EISA) approach to fabricate mesoporous silica with ultra large pore size 30.8 nm using poly(ethylene oxide)-*b*-polystyrene (PEO-*b*-PS) diblock copolymer as the template.[75] However, to date these approaches have not been successfully applied to the formation of mesoporous films. A method[80] using PMMA latex nanoparticles as sacrificial template was developed to fabricate mesoporous silica films with large pore size (30 nm-80 nm), however only disordered spherical pores were achieved as shown in Figure 2.2c.

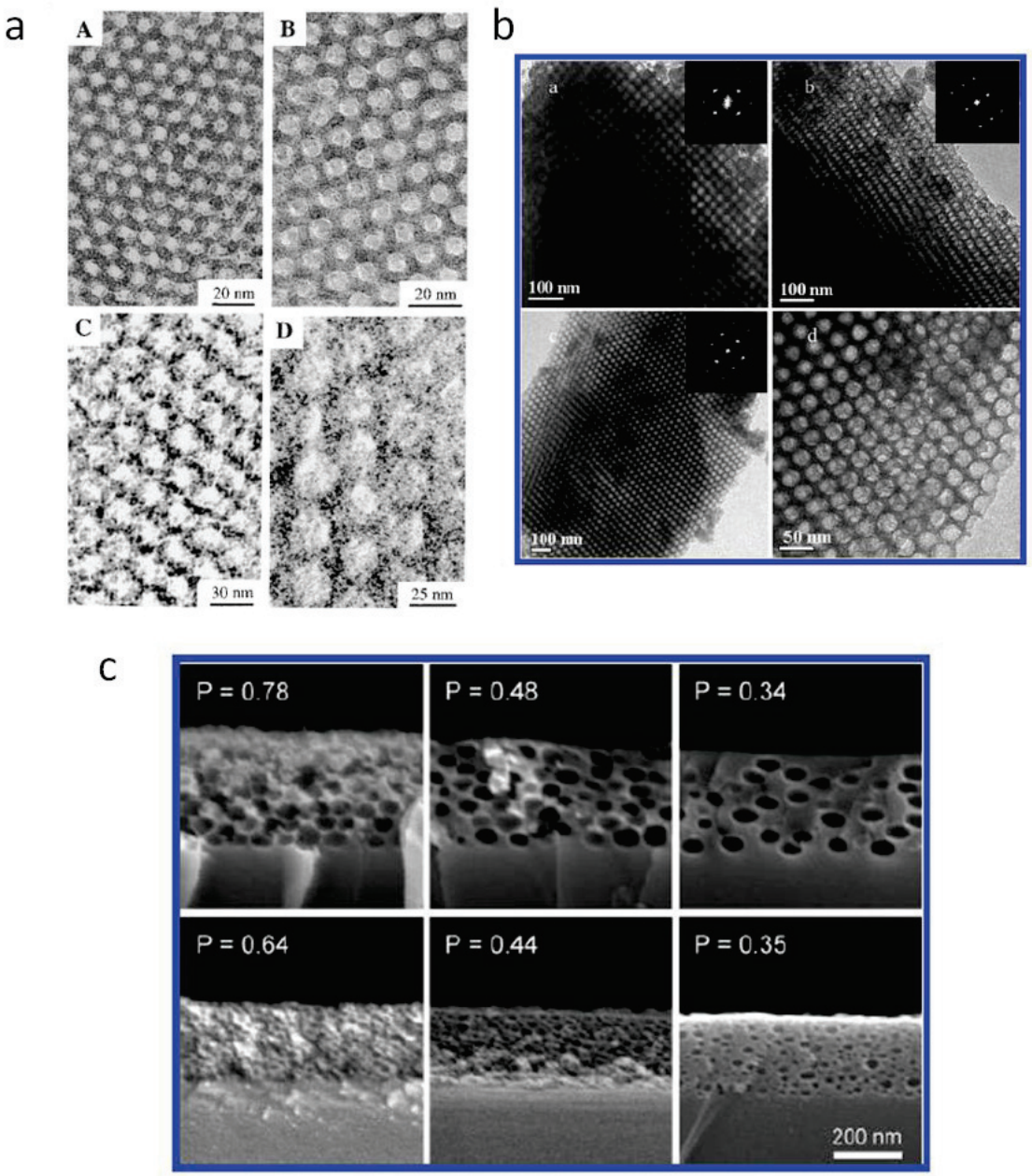

Figure 2.2 (a) TEM characterization for hexagonal SBA mesoporous silica with large pore-size using amphiphilic PEO-PPO-PEO triblock copolymers as the structure directing agent fabricated in acidic condition. Adapted from Ref.[70] (b) TEM images of calcined mesoporous silica with large pore size fabricated through EISA approach using laboratory-made PEO-*b*-PS diblock copolymers as templates. Adapted from Ref.[75] (c) SEM images of mesoporous silica films with ultra-large pores (30 nm~80 nm) fabricated using PMMA latex nanoparticles as sacrificial template. Adapted from Ref.[80]

2.1.3. Mesoporous silica films with hexagonal cylindrical pores

The fabrication of films with well controlled cylindrical pores in mesoporous silica films is of interest for many applications including the fabrication of solid state devices for processing, separation and detection. Couple reports indicate the fabricate of well controlled cylindrical pores in mesoporous silica films,[81-84] but with relatively small pore size (less than or around 10 nm). For example, the most recent report by Bein and coworkers[81] shows that by filling EISA precursor solution into microgrooves made by poly(dimethylsiloxane) stamp as shown in Figure 2.3d, alignment of the mesopores can be achieved in the final mesoporous silica films. Pluronic F127 triblock copolymer was used as the template in this process to achieve meosporous silica film with aligned mesopores, characterized by XRD (Figure 2.3a) and TEM cross-section (Figure 2.3b, c) which is perpendicular to long axes of a silicon bar. However, the pore size is still relatively small with only 7~8 nm. To achieve separation and detection of large molecules, macromolecules and biomolecules, fabrication of meosporous silica films with cylindrical channels over a much larger size scale is necessary.

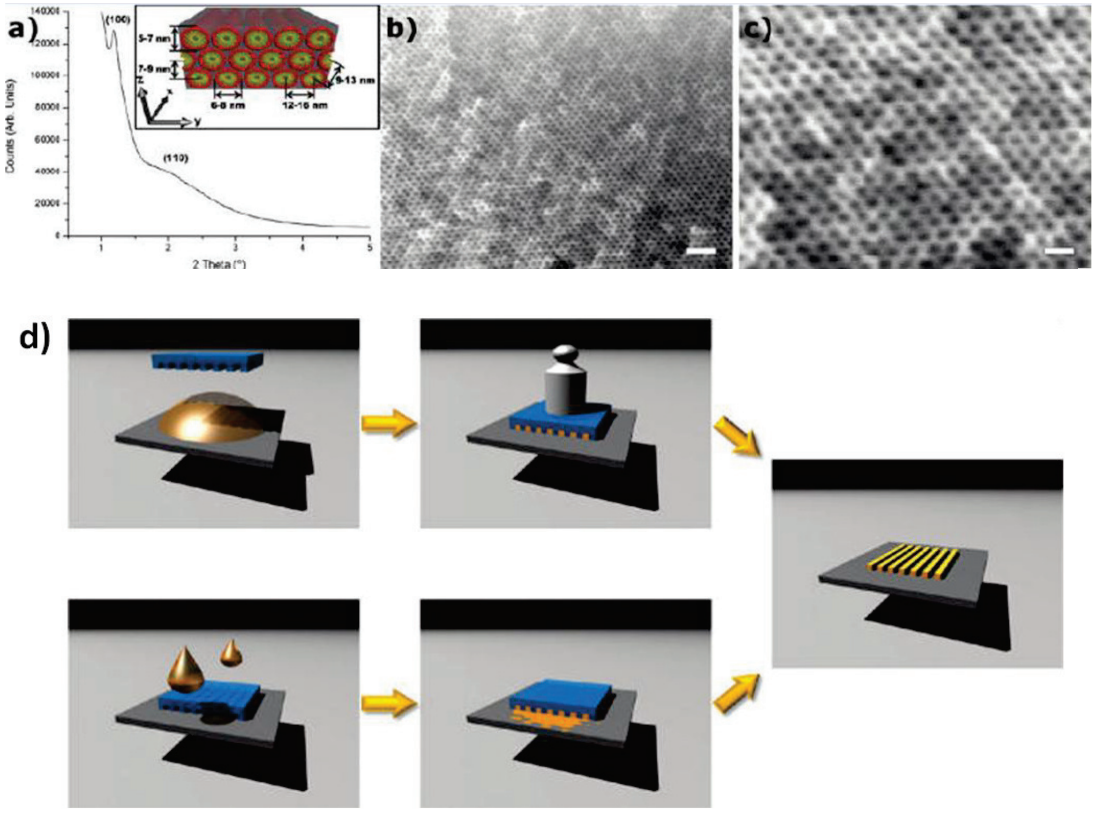

Figure 2.3 (a) XRD pattern for the mesopore silia film. (b, c)HR-SEM images of the cross-section (perpendicular to the silicon bar) of mesoporous silica films with aligned channels. Scale bars are (b) 50 nm and (c) 20 nm. (d) The process for the mesopore alignment through confinement in PDMS microgrooves in two different approaches. Adapted from Ref.[81]

2.1.4. Fabrication of mesoporous silica films by 3-D replication of block copolymer morphology in supercritical CO_2

Previously, our group reported an efficient pathway[85] to well-ordered, robust mesoporous films with tailored morphologies through the infusion and selective condensation of silica and organosilicate precursors[86] within one phase of a pre-formed block copolymer template dilated with supercritical carbon dioxide. The template is subsequently removed from the resulting composite *via* thermal degradation to produce the mesoporous oxide films. The process is shown in Figure 2.4. The role of the supercritical fluid in the process is two-fold. The solubility of the silica precursor in CO_2 enables its infusion into the template and modest dilation of the template with CO_2

enables facile diffusion of the reagents and by-products during the silica condensation reaction[87-88] without excessive dilation, which could disrupt the desired template structure, orientation and/or morphology. This strategy has been applied to the synthesis of films with spherical pores for use as ultra-low dielectric constant materials,[85] to the fabrication of films with vertically[89] and horizontally[90] oriented cylindrical nanochannels, and most recently to the direct patterning of mesoporous films without the need for etching,[91-92] as shown in Figure 2.5. One advantage of this approach compared to those that involve cooperative assembly with simultaneous silica network condensation is the separation of template organization and silica condensation into discreet steps. Such an approach enables conveyance of the structural details of template film into the silica replica. Moreover, films produced *via* this process exhibit low residual stress and excellent mechanical stability. [85]

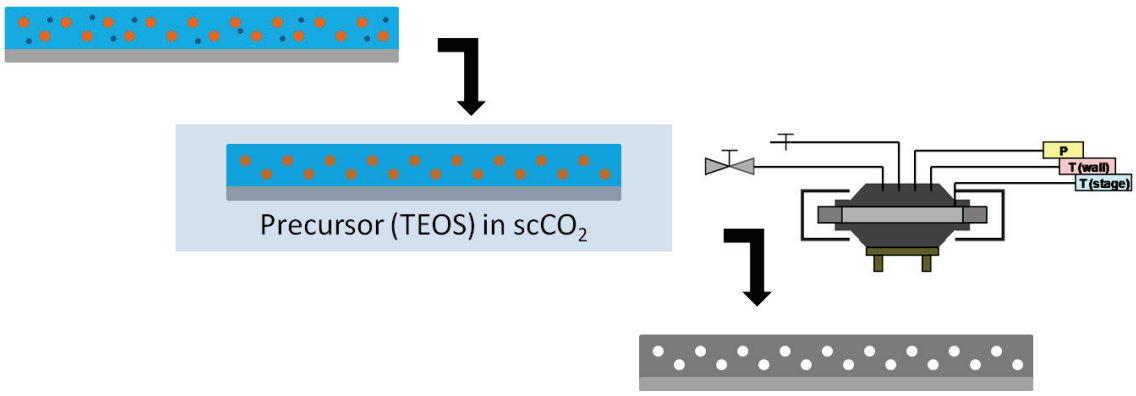

Figure 2.4 Schematic representation of the process for fabrication of mesoporous silica films in supercritical CO_2.

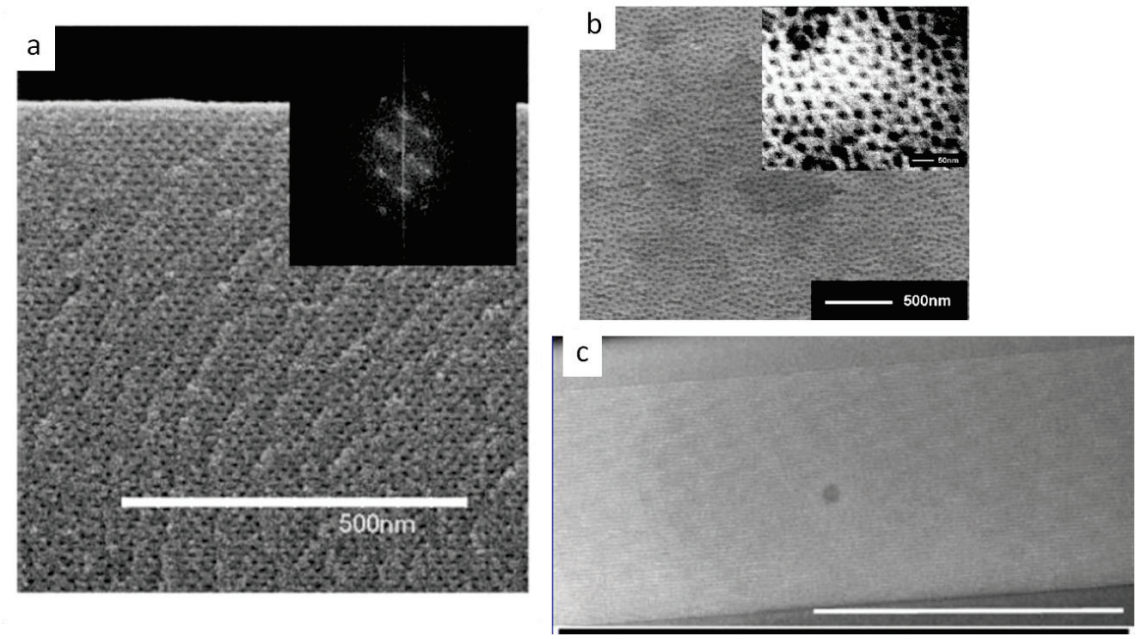

Figure 2.5 (a) SEM characterization of the cross section of the mesoporous silica film template from Pluronic F108 in $scCO_2$. Adapted from Ref.[85] (b) Field emission scaning electron micrograph of mesoporous silica film with vertically oriented cylindrical nanochannels. Adapted from Ref.[89] (c) Transmission electron microscopy characterization of the mesoporous silica film templated from Pluronic F127 with 16.7% PHS as the additive blended film in $scCO_2$.Adapted from Ref.[90]

2.2 Experimental

2.2.1 Materials

N,N,N',N',N''-pentamethyldiethylenetriamine (PMDETA), styrene, *tert*-butyl acrylate, ethyl-2-bromoisobutyrate, anisole, Copper(I) bromide, Copper(II) bromide, and tetraethylorthosilicate (TEOS) (99%) were purchased from Acros Organics and triphenylsulfonium triflate (TPST) was purchased from Sigma-Aldrich. Photo-resist NR9-1000PY was purchased from Futurrex, Inc. A quartz mask with line-patterns for photolithography was obtained from Benchmark Technologies, Inc.

2.2.2 Block copolymer synthesis.

Atom transfer radical polymerization (ATRP) was used for the synthesis of poly(styrene-*b*-*tert*-butyl acrylate) (PS-*b*-PtBA) diblock copolymers using established procedures with slight modification.[93] A magnetic stirbar, CuBr and $CuBr_2$ were added in a pear-shape Schlenk flask, which was dried in an oven overnight and caped with a rubber septa, evacuated and purged. Distilled styrene and PMDETA (purged with house nitrogen (N_2) for 30 minutes), were injected into the flask. After three freeze/pump/thaw cycles, the initiator ethyl-2-bromoisobutyrate was injected dropwise into the flask which was then heated to 90°C for 5 h. After dilution with tetrahydrofuran (THF), the resulting dark green solution was run through a column of neutral alumina and then precipitated in excess methanol, filtered, washed and dried. The product was used as the macroinitiator for chain extension, also performed following similar procedures with a slight modification.[93] The macroinitiator (PS), CuBr, and a magnetic stirbar were added into a Schlenk flask, followed by addition of purged anisole and distilled *tert*-butyl acrylate. After all solids were completely dissolved and three freeze/pump/thaw cycles, PMDETA was injected dropwise into the flask which was then heated for 48 h at 60°C. The same purification procedure as the first step was performed to give a white solid.

2.2.3 Formation of polymer film templates.

350 nm thick polymer films were spin-coated from a 3~5 wt% solution of PS-*b*-PtBA prepared in chloroform with 5 wt% TPST (to polymers) onto silicon wafers or patterned substrates at 3000 rpm for 60s. To achieve different thickness films, the spin-coating solution was diluted or concentrated. The template film cast on the silicon wafer was then annealed under chloroform vapor in a bell jar prior to infusion.

2.2.4 Infusion of silica alkoxide precursors.

The templates were subject to UV flood exposure (254 nm) at room temperature for 20 sec with 40 MJ/cm^2 and then sealed inside of a 150 ml stainless steel reactor containing 10 μL of TEOS. At room temperature (r. t.), 62 mL of CO_2 with the pressure of 68.9 bar and temperature of r. t. was injected into the reactor. The reactor was then heated to 60^{o}C for 2 h at a pressure of 103 bar. The composite was removed from the reactor and a uniform mesoporous silica film was generated by calcination at 400^{o}C for 6 h in air using a temperature ramp rate of 1.56°C/min.

2.2.5 Characterization

Gel permeation chromatography (GPC) was performed in THF at a flow rate of 1.0 mL/min using polystyrene as standards. 1H NMR spectra were acquired on a Bruker DPX300 NMR spectrometer (300 MHz) in deuterated chloroform. Atomic force microscopy (AFM) topographic and phase images were acquired on a Digital Instruments Dimension 3000 scanning microscope in tapping mode. A profilometer (Dektak3) and a Filmetrics Optical Profilometer were used to measure the thickness of the films.

Transmission electron microscopy (TEM) was performed on a JEOL 2000FX electron microscope operating at 200 kV. The mesoporous silica films were scraped off the substrates using a razor blade and ground to form a dilute slurry in ethanol. The suspension was dropped onto Formvar coated copper grids (Electron Microscopy Sciences), which was then dried in air prior to imaging.

Grazing incidence small angle X-ray scattering (GISAXS) experiments were performed at the G1 station of the Cornell High Energy Synchrotron Source (CHESS). The wavelength of X-rays used was 1.4617 Å and the sample to detector distance was

2572.1 mm. The angle of incidence was chosen to be above the critical angle of the film under study. A two-dimensional charge-coupled device (CCD) camera with image sizes of 1024 pixels by 1024 pixels was used to collect the scattered radiation. The GISAXS 1D profiles were all based on the integration of line scans in q_// axes.

2.3 Results and Discussion

2.3.1 Block copolymer synthesis and template formation.

Poly(styrene-*b*-*tert*-butyl acrylate) (PS-*b*-PtBA) copolymers of tailored molecular weight and volume fraction were used as templates (Table 2.1). Except for P3, all the polymers from Table 2.1 were synthesized by atom transfer radical polymerization (ATRP) at molecular weights ranging from 44K to 153K.

	Polymer Templates					Mesoporous Silica Films		
Sample	Mn (PS)	Mn (PtBA)	Total	PtBA weight %	PDI	Morphology	d-spacing [a]	Pore size[b]
P1	28K	125K	153K	81.7%	~1.5	Spherical	76 nm	~40 nm
P2	23K	100K	123K	81.3%	~1.33	Spherical	62 nm	~37 nm
P3[c]	19K	69K	88K	78.4%	1.07	Cylindrical	40 nm	~22 nm
P4	11.4K	32.7K	44.1K	74.1%	1.3	Cylindrical	38 nm	~20 nm
P5	11.4K	37.9K	49.3K	76.9%	1.21	Cylindrical	35 nm	~17 nm

[a] Calculated from GISAXS data, [b] estimated from TEM images, [c] Acquired from Polymer Source by anionic polymerization. All others synthesized by ATRP.

Table 2.1 Characteristics of PS-*b*-PtBA templates used in this study and characteristics of the corresponding mesoporous silica films prepared using the templates.

We first investigated how improvements in microphase segregation and the degree of order imparted to the PS-*b*-PtBA templates *via* solvent annealing in the presence of chloroform impacted the morphology of the mesoporous films. Chloroform,

which exhibits a solubility parameter, δ(SI), of 18.7 is a good solvent for both PS and PtBA. We used two annealing protocols. In the first, the template films were annealed in saturated chloroform vapor at room temperature for 4 h. The second protocol involved annealing in dilute chloroform vapor (200 µl chloroform in a 250 ml jar) for 15 h at room temperature. Figure 2.6a shows an AFM phase image of a 400 ± 30 nm thick film of 49.3K PS-*b*-PtBA containing a PtBA weight percentage of ~77% (Table 2.1, P5) prepared by spin coating from a 3 wt % solution of the copolymer in chloroform. The image (Figure 2.6a) suggests poor microphase segregation and weak order in the as spun template. Figure 2.6b is an image of the film after annealing in saturated chloroform vapor for 4 h at room temperature, which yielded a cylindrical morphology with grains containing cylinders oriented perpendicular or parallel to the substrate. Figure 2.6c shows an image of films after annealing in dilute chloroform vapor for 15h. These annealing conditions resulted in a cylindrical morphology in which the domains are primarily oriented parallel to the substrate.

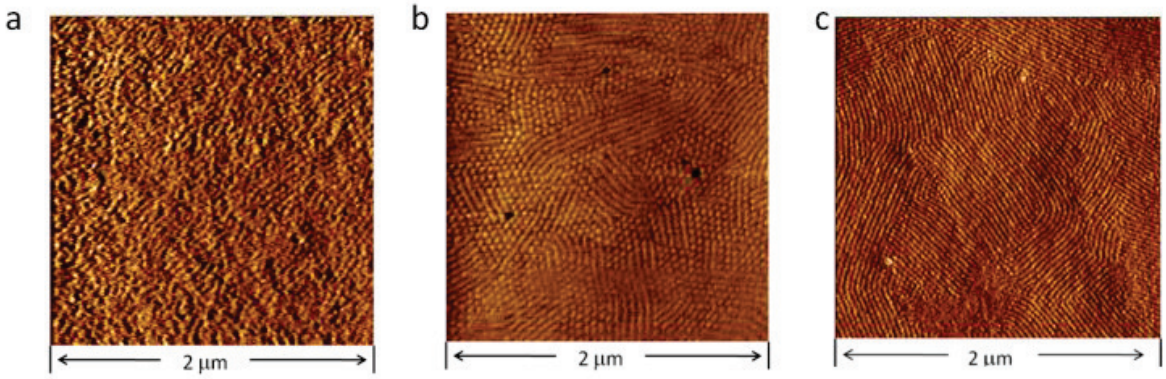

Figure 2.6 AFM Images of PS-*b*-PtBA film (P5, 49.3K PS-*b*-PtBA , 76.9% PtBA, PDI=1.21) before and after solvent annealing. (a) As-spun film. (b) Film annealed under saturated chloroform atmosphere for 4 h. (c) Film annealed under dilute chloroform vapor (200 µl chloroform in a 250 ml jar) for 15 h.

Similar chloroform annealing methods were applied to other PS-*b*-PtBA films with different molecular weights and PtBA volume fractions to give well-ordered structures, as shown in Figure 2.7. The thicknesses of these films are in the range of 400 ± 50 nm, which are about 6 times larger than their d-spacings. Block copolymers P1 and P2 from Table 2.1 exhibited spherical morphologies, as shown in Figure 2.7a and Figure 2.7b, while P3, P4 and P5 exhibited cylindrical morphologies as shown in Figure 2.7c, 2.7d and 2.7e. Table 2.1 shows the morphologies of polymer templates as well as the d-spacings and approximate pore dimensions of the mesoporous silica films fabricated using each of the templates. Templates with spherical pore morphologies and ~75 nm and ~64 nm d-spacings were prepared using P1 and P2 respectively (Figure 2.7a, 2.7b). Films prepared using block copolymer P1 (Mn = 153K, PDI = 1.5) exhibited poor order, while films prepared using P2, (Mn = 123K, PDI = 1.33) exhibited a face-centered cubic FCC morphology with a d-spacing of 64.1 nm as confirmed using grazing-incidence small-angle X-ray scattering (GISAXS) (Figure 2.7f).

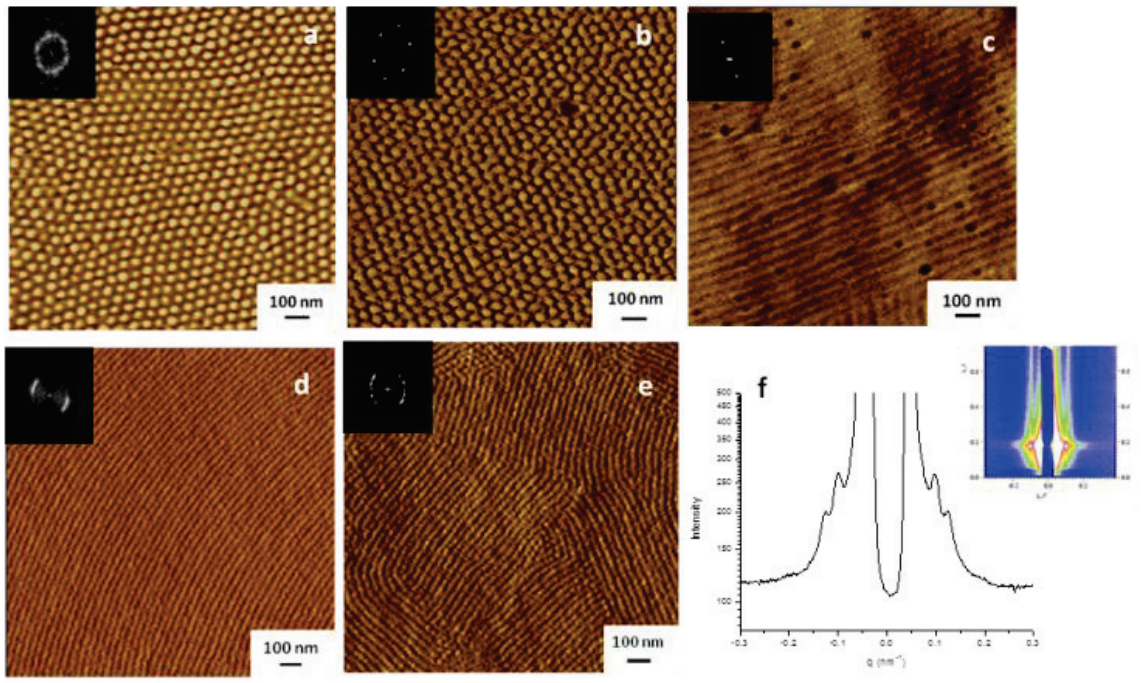

Figure 2.7 AFM phase images (a~e) for PS-*b*-PtBA films with film thicknesses of 400 ± 50 nm after chloroform annealing. (a) P1 (153K PS-*b*-PtBA , 81.7% PtBA, PDI=1.5) after solvent annealing for 24 h in saturated chloroform vapor (b) P2 (123K PS-*b*-PtBA, 81.3% PtBA, PDI=1.33) after 24 h in dilute chloroform vapor (250 µl chloroform in a 250 ml jar). (c) P3 (88K PS-*b*-PtBA, 78.4% PtBA, PDI=1.07) after annealing for in saturated chloroform vapor. (d) P4 (44.1K PS-*b*-PtBA , 74.1% PtBA, PDI=1.3) after annealing for 15 h in dilute chloroform vapor (200 µl chloroform in a 250 ml jar). (e) P5 (49.3K PS-*b*-PtBA , 76.9% PtBA, PDI=1.21) after annealing in dilute chloroform vapor (200 µl chloroform in a 250 ml jar). (f) GISAXS spectrum and integration for P2 shown in (b).

2.3.2 Mesoporous silica film fabrication using BCP templates.

The use of supercritical fluid assisted infusion and phase selective condensation of metal oxide precursors to fabricate mesoporous films is described in detail elsewhere.[85, 91-92, 94-95] Here, we show that the use of CO_2 dilation enables silica condensation within well-ordered PS-*b*-PtBA template films with molecular weights (44.1k to 153k) yield large-pore (17 to 40 nm) silica films. The photo-acid generator triphenyl sulfonium triflate (TPST) was used to generate acid within the template upon exposure to UV-light (254nm). The chemical amplification process and tetraethyl

orthosilicate (TEOS) infusion occur simultaneously within the supercritical carbon dioxide reactor to convert the PtBA domain into polyacrylic acid (PAA) and to initiate silica condensation selectively within the hydrophilic PAA-rich matrix to form a polymer/silica composite film at 60^{o}C and 105 bar. The mesoporous silica films were obtained by removal of the template *via* calcination. We point out that the use and deprotection of PS-*b*-PtBA templates offers distinct advantages to the direct use of PS-*b*-PAA as template. These include ease of solubility and spin-coating of the template and the relatively low Tg of the PtBA block relative to PAA, which facilitates achievement of well-ordered films during thermal annealing and the infusion of the silica precursor during the SCF exposure step. The morphology of mesoporous films prepared from templates of PS-*b*-PtBA was investigated using transmission electron microscopy (TEM) and GISAXS.

Figure 2.8 shows the mesoporous silica film obtained using PS(19K)-*b*-PtBA(69K) as the template (P3, Table 2.1). TEM imaging suggests a cylindrical morphology with hexagonal packing (Figure 2.8a, b) and a pore diameter of ~22 nm. GISAXS confirmed the morphology and revealed a d-spacing of 40 nm (Figure 2.8c, d). GISAXS was also used to compare the as-infused and as-spun films. There is no obvious difference of the q values of the first order peak in all three films indicating little influence of swelling or shrinkage during the process. The increase in peak intensity from the as-spun to as-infused, to calcined films evident in Figure 2.8d is as expected due to increasing electron density contrast in the silica/polymer composite and the mesoporous silica film relative to the PS-*b*-PtBA template.

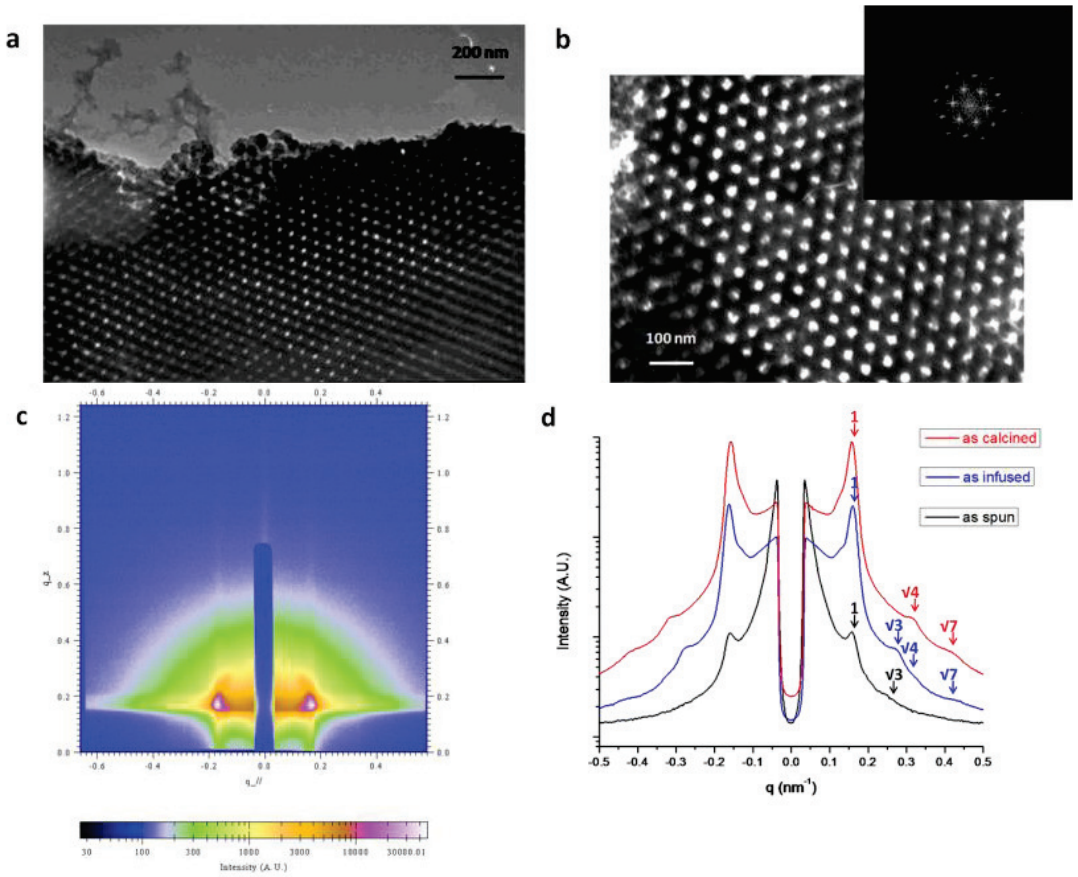

Figure 2.8 Characterization of mesoporous silica film templated from P3 (88K PS-*b*-PtBA, 78.4% PtBA, PDI=1.07). (a,b) TEM images, (b) is shown with its Fourier transform. (c) GISAXS analysis of the film. (d) Integration of the GISAXS data for the as-spun PS-*b*-PtBA film, the as infused polymer/silica composite film and the calcined mesoporous silica film.

A similar supercritical fluid assisted infusion process was applied to other ordered PS-*b*-PtBA templates (shown in Figure 2.7) to generate mesoporous silica films with well-ordered structures and tunable pore sizes and shapes (Figure 2.9, Table 2.1). We note here that while pore diameters and d-spacings of the mesoporous films can be controlled by varying the molecular weight of the polymer templates, the final mesoporous film dimensions are also influenced by the mass uptake of silica during fabrication and silica network contraction during calcination. Figure 2.9a and 2.9b, show mesoporous silica films with d-spacings of 76 nm and 62 nm respectively. The 40 nm pores shown in figure

2.9a are to our knowledge the largest reported in a mesoporous silica film. GISAXS measurements were used to confirm the morphologies and d-spacings and to provide clear information about the morphology over large areas on the film surface (see Figure 2.10 and 2.11) As shown in Figure 2.9 and Table 2.1 similar d spacings of ~40 nm (P3, P4) were templated from two block copolymers with very different molecular weights of 88K and 44K respectively. The two BCPs were synthesized using different methods, which yield large differences in PDI. The BCP (P3) was synthesized by anionic polymerization and was purchased from Polymer Source while the BCP (P4) was synthesized by ATRP as shown in the experimental section. The relatively large polydispersity of the template block copolymers produced by ATRP gave rise to larger d-spacing relative to narrow PDI samples of the same molecular weight. These larger template d-spacings are reflected in the mesoporous films. Self-consistent field theory has been used to quantitatively explain this phenomenon. [96-98]

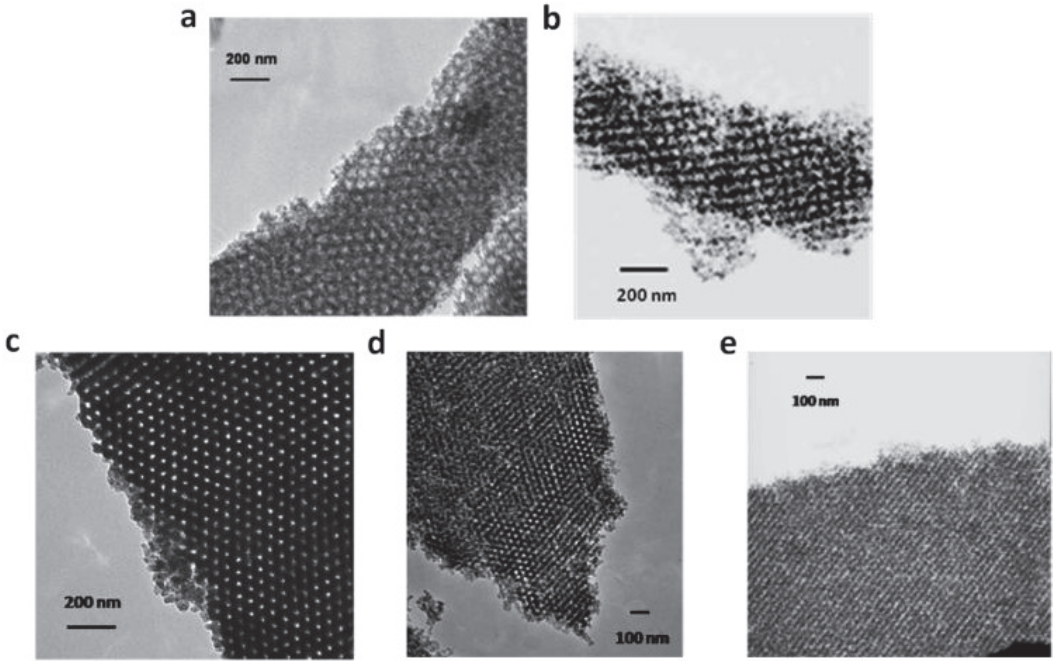

Figure 2.9 TEM images of mesoporous silica films templated from templates (a) P1, (b) P2, (c) P3, (d) P4 and (e) P5 in Table 2.1 and Figure 2.7.

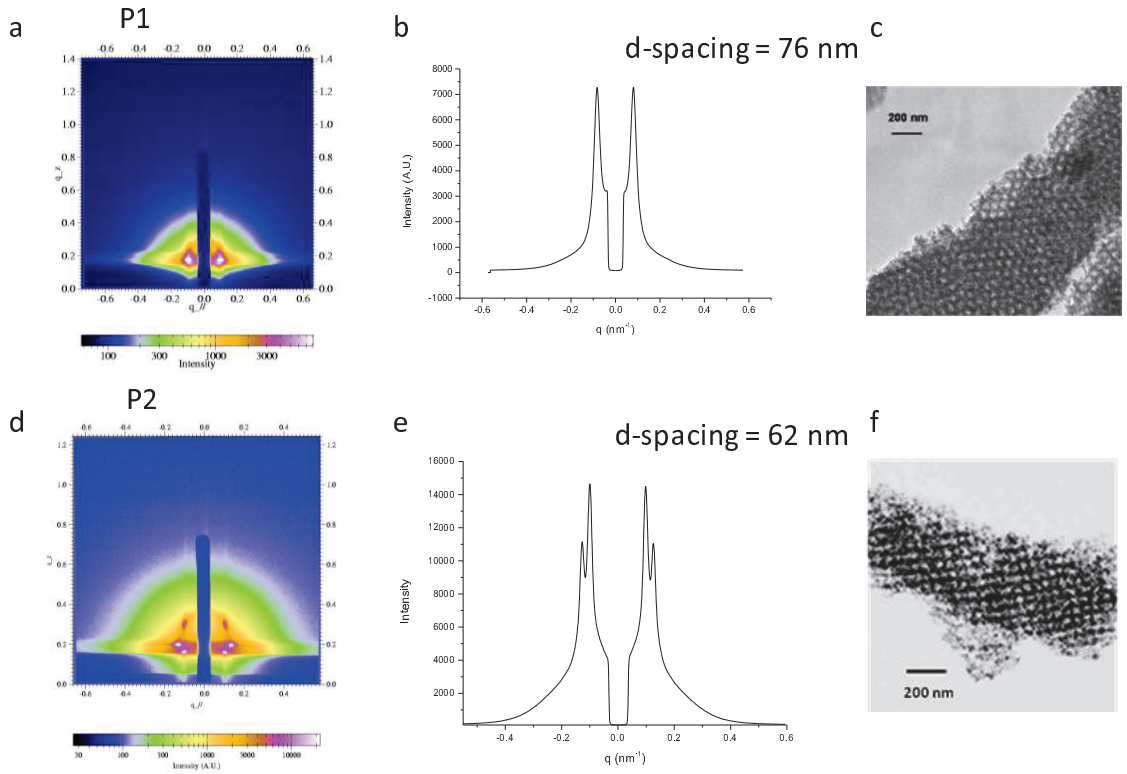

Figure 2.10 (a) GISAXS spectrum and (b) GISAXS integration for mesoporous silica film templated from P1 (153K PS-b-PtBA , 81.7% PtBA, PDI=1.5) see Table 2.1 Figure 2.7. The d-spacing is 76 nm. (c) TEM image of the mesoporous silica film; (d) GISAXS spectrum and (e) GISAXS integration for mesoporous silica film templated from P2 (123K PS-b-PtBA , 81.3% PtBA, PDI=1.33) see Table 2.1 and Figure 2.7. The d-spacing is 62 nm. (f) TEM image of the mesoporous silica film.

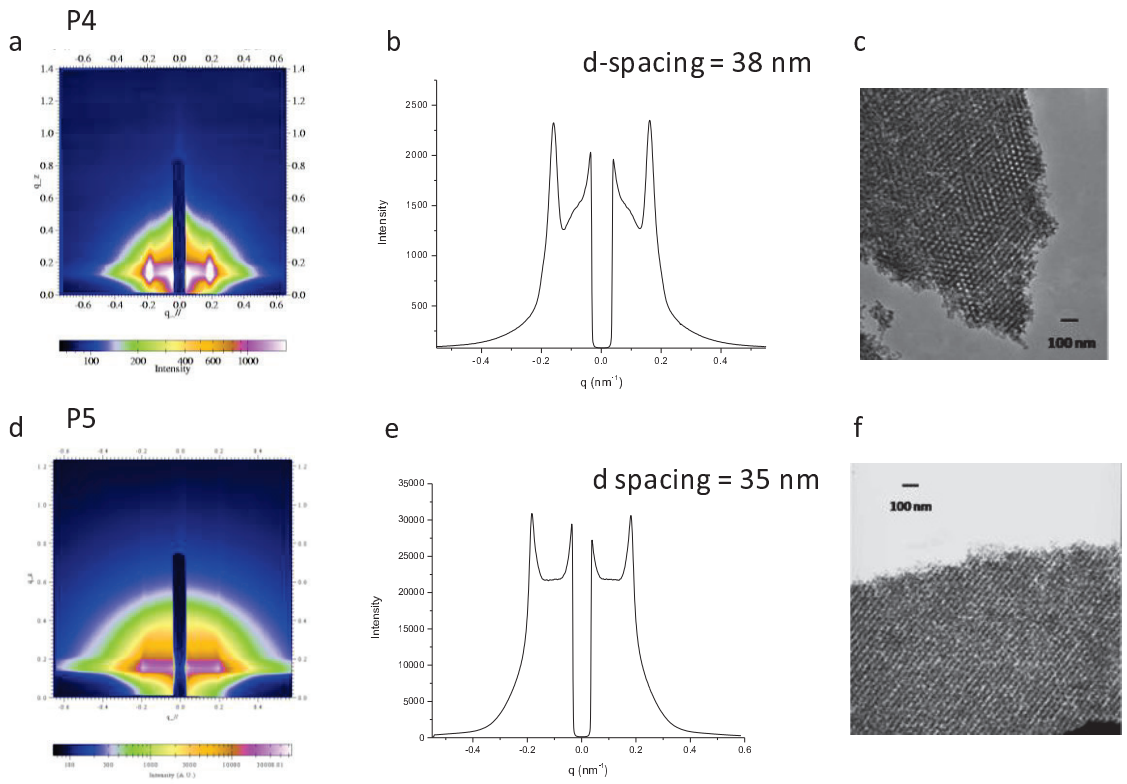

Figure 2.11 (a) GISAXS spectrum and (b) GISAXS integration for mesoporous silica film templated from P4 (P4 (44.1K PS-*b*-PtBA , 74.1% PtBA, PDI=1.3)) see Table 2.1 Figure 2.7. The d-spacing is 76 nm. (c) TEM image of the mesoporous silica film; (d) GISAXS spectrum and (e) GISAXS integration for mesoporous silica film templated from P5 (49.3K PS-*b*-PtBA , 76.9% PtBA, PDI=1.21) see Table 2.1 and Figure 2.7. The d-spacing is 62 nm. (f) TEM image of the mesoporous silica film.

2.3.3 Influence of template film thickness on cylindrical pore orientation

It is well known that the domain orientation in block copolymer films cast on solid substrates is influenced by both surface interaction and the thickness of the film. AFM and GISAXS analysis shown in Figure 2.12 indicates that for a PS(11.4K)-*b*-PtBA(37.9K) copolymer exhibiting a cylindrical morphology (P5 in Table 2.1) cast onto the native oxide of a Si wafer with a film thickness equivalent to 6 or 12 times the domain spacing, the cylinders are oriented parallel to the substrate. As the thickness decreases towards that equivalent to a single layer, the cylinders are oriented

perpendicular to the substrate with hexagonal packing (Figure 2.12d). The influence of film thickness on domain orientation was experimentally investigated by van Dijk[99] and theory developed by Lee.[100] For very thin films in the absence of strong preferential interactions of the surface with one of the blocks, conformational entropy energy dominates the total free energy, leading to vertical orientation of the cylinders. For films whose thicknesses are large relative to domain spacing, two degrees of orientational freedom are available in a parallel morphology.[99-100] Thus, the parallel cylinder orientation is favored in a thick film, while perpendicular orientation is favored in a thin film. GISAXS analysis confirmed that these orientations are maintained during the template replication process in supercritical carbon dioxide and are subsequently conveyed to the mesoporous silica films. As shown in the thick film (Figure 2.12b, c), the first order peak gives a d-spacing of ~35 nm and the weak intensity is consistent with weak in-plane ordering. While, in the thin film (Figure 2.12e), the sharp scattering rods along the q_z axis vertical to q_// axes indicate the vertical cylinder orientation and the higher order peaks at √3, √4 and √7 multiples of the location of the first order peak confirm a cylindrical morphology with in-plane hexagonal packing exhibiting a d-spacing equivalent to those found in the thicker films containing pores oriented parallel to the surface.

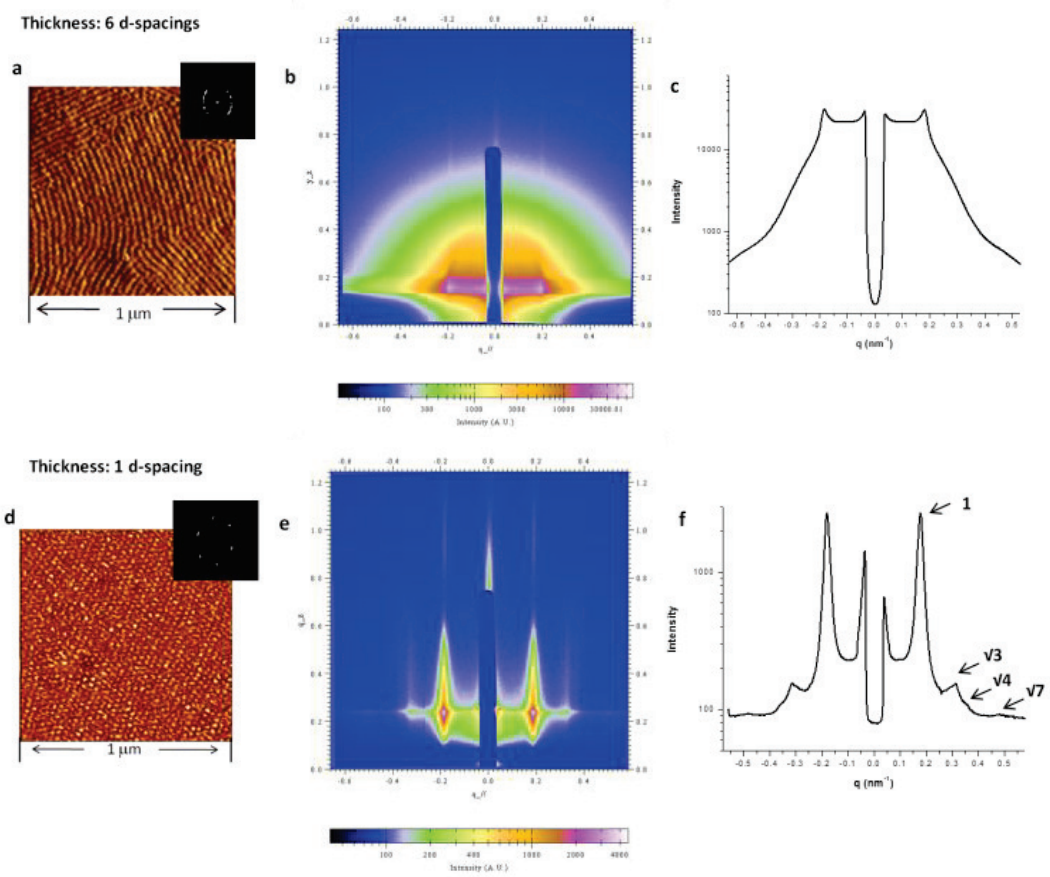

Figure 2.12 Influence of template thickness on the morphologies of the template P5 (49.3K PS-*b*-PtBA , 76.9% PtBA, PDI=1.21) annealed in dilute chloroform vapor for 15 h and corresponding mesoporous silica films for template thicknesses equivalent to 6 d-spacings or 1 d-spacing. (a) AFM image of template with thickness of 6 d-spacings (b) GISAXS spectrum and (c) GISAXS 1D integration line profile of mesoporous film in q_// derived from (a). (d) AFM image of template with thickness of ~1 d-spacing. (e) GISAXS spectrum and (e) GISAXS integration of mesoporous film derived from (d).

2.3.4 Influence of template film thickness on spherical pore packing.

BCPs with spherical morphologies can exhibit BCC or FCC packing. While BCC morphologies are common, the FCC morphology in neat block copolymers has been theoretically studied[101-102] but is not often observed experimentally because of its narrow temperature window within the phase diagram,[101, 103] strong thermal fluctuations under experimental conditions,[104-105] or competition with the disordered micelle regime.[106] In

the work presented here, BCPs with high PDIs and high molecular weight, synthesized by ATRP, have larger FCC windows relative to copolymers with narrow PDI and the FCC morphology can be kinetically trapped during solvent annealing.[107-108] For the block copolymer (PS23K-*b*-PtBA100K, P2 in Table 2.1) cast on the native oxide of a silicon wafer with a thickness equivalent to 6 d-spacings, an FCC spherical morphology was confirmed by AFM measurement of template morphology (Figure 2.13a) and GISAXS measurement (Figure 2.7f).

The influence of film thickness on spheres packing in the polymer template PS-*b*-PtBA films (PS23K-*b*-PtBA100K, P2 in Table 2.1) has also been observed. As the thickness decreased to a monolayer, the spherical pores pack into a hexagonal array was confirmed by AFM (Figure 2.13b). Due to the packing frustration[109], the hexagonal Wigner-Seitz (W-S) cell of sphere monolayer has a relatively smaller free energy increase to make the transition from FCC to hexagonal packing possible when the thickness decreases to a monolayer.

Supercritical CO_2 infusion was then applied to convey the influence of film thickness on sphere packing within polymer template to pore packing within mesoporous silica films. The FCC packing was confirmed by higher order peaks, $\sqrt{4/3}$ and $\sqrt{11/3}$, in GISAXS analysis for as-infused silica/polymer composite films with 6-d spacing (Figure 2.13d). As for mesoporous silica films after calcination, three thicknesses of 12 d-spacings, 6 d-spacings and 1 d-spacing have been investigated in this study by GISAXS, and the results are shown in Figure 2.14a, b and c. The 12 d-spacings and 6 d-spacings gave similar scattering results that were assigned to spherical pores with FCC packing,

while the 1 d-spacing gave √3q as first high order peak in GISAXS results, indicating the hexagonal packing.

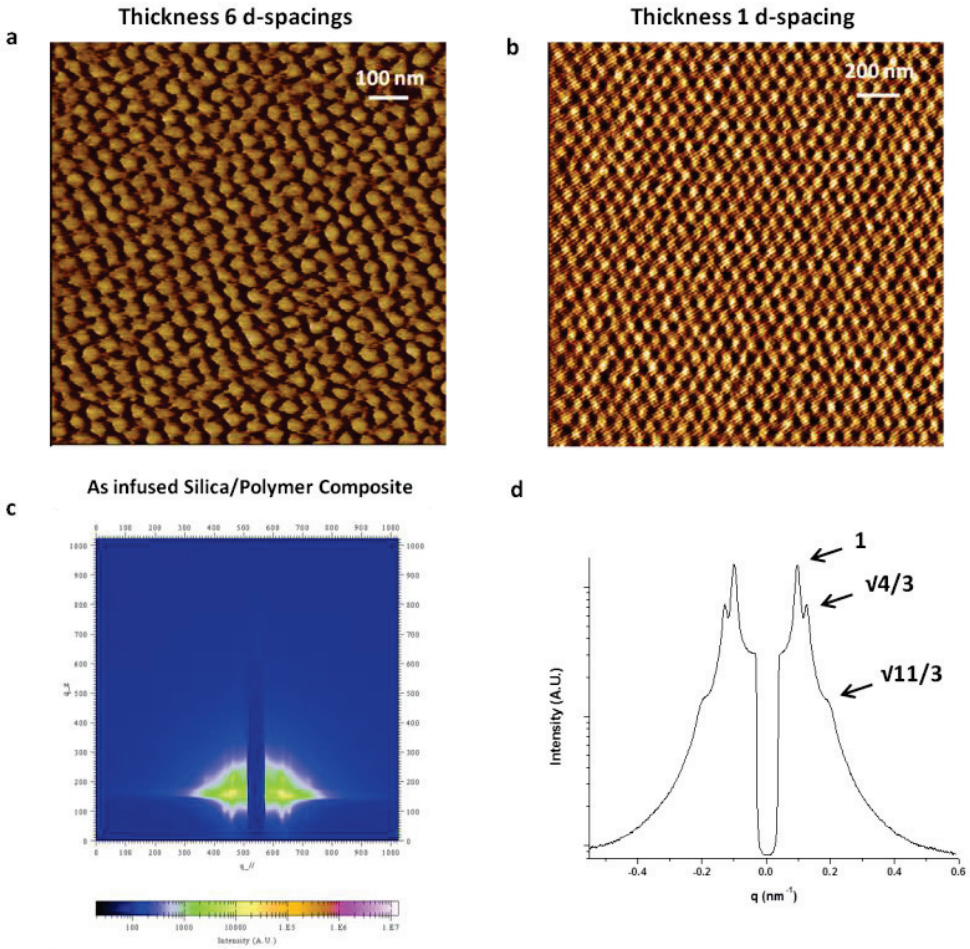

Figure 2.13 Influence of template thickness on sphere packing in the template film and in the corresponding mesoporous silica film. AFM phase images for P2 (123K PS-*b*-PtBA, 81.3% PtBA, PDI=1.33) with the thickness equivalent to ~ 6 d-spacings (a) and 1 d-spacing (b). (c) GISAXS spectrum and (d) its integration for silica/polymer composite prepared from (a).

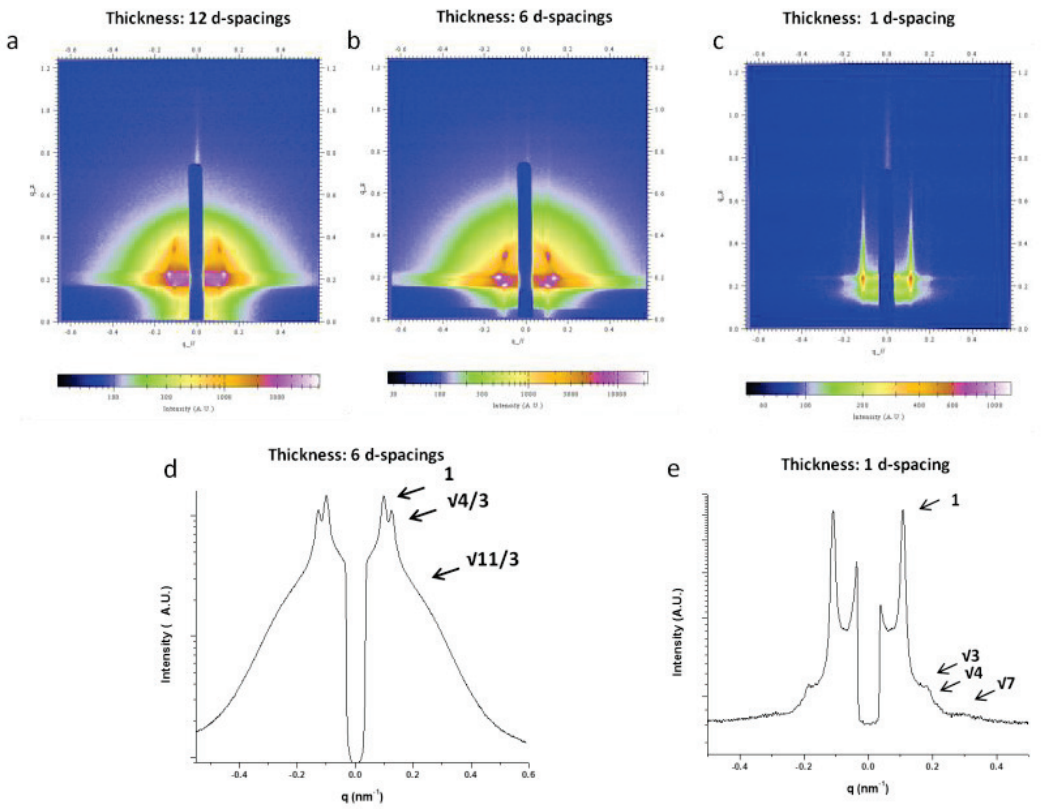

Figure 2.14 (a~c) GISAXS spectrum and (d,e) GISAX integrations for mesoporous silica film templated from P2 (123K PS-*b*-PtBA , 81.3% PtBA, PDI=1.33) at thickness equivalent to 12 d-spacings, 6 d-spacings and 1 d-spacing.

2.4 Conclusion

A method to fabricate mesoporous silica films with large pores of tunable geometry is presented. Excellent control of film structure was possible due to the separation of template preparation, precursor infusion and silica condensation into discrete steps. The template morphology was controlled by varying the molecular weight, volume fractions of the segments, and PDI of the block copolymer and by controlling film thickness and annealing conditions. Structures developed in the template by manipulation of these variables, including FCC spherical packing, an uncommonly accessed morphology in phase diagram, were successively conveyed to the mesoporous

films. Large pores in mesoporous silica films were accessible by increasing both the molecular weight and the PDI of the template. Pore orientation in films containing cylindrical pores was controlled by adjusting template film thickness. Such precise control of morphology in mesoporous silica films is expected to enhance their utility in a broad range of applications.

CHAPTER 3

DIRECTED SELF-ASSEMBLY TO ACHIEVE LONG-RANGE ALIGNED MESOPOROUS SILICA FILMS

3.1 Introduction

The fabrication of microfluidic or molecular-scale devices requires the well alignment of the mesochannels within the mesoporous silica films.[110] Using mesoporous silica films as templates to align other functional compounds with anisotropic properties also requires the well control of the alignment of the mesochannels.[111-113] To date several methods have already been reported to produce mesoporous silica films with aligned channels.[81-84] External fields, including magnetic fields,[114] shear flow,[115] and electric fields,[116] have been used for mesochannel alignment in mesoporous silica films. Various substrates such as the (110) crystal face of silicon,[117] mica,[118-119] and rubbing-treated polyimide films[120-122] have also been used to align mesochannels. For example, epitaxial growth was used by K. Kuroda and coworkers[118] to align the mesochannels in a mesoporous silica film by EISA process on a freshly cleaved mica ($K_2Al_4(Al_2Si_6O_{20})(OH)_4$) surface as shown in Figure 3.1a. Hot air flow was also used by Q. Lu and coworkers[123] to orient the precursor and surfactant solution before EISA process using a shear force induced by the hot jet air flow as shown in Figure 3.1b. Both methods using EISA process to fabricate the mesoporous silica film using small molecular surfactants to give only small pore size. And also the simultaneous processes combining order generation and silica formation in one step involved and the kinetic constraints during the process, control of morphology becomes complicated and nice

ordering becomes relatively difficult to achieve, especially for high molecular weight surfactants or block copolymers to achieve large-size channels. Thus, the pore sizes generated through those methods are relatively small with only 7~8 nm. Again, for applications including microfluidics and biomolecule separation, it is very necessary to achieve well aligned cylindrical channels with large pore size.

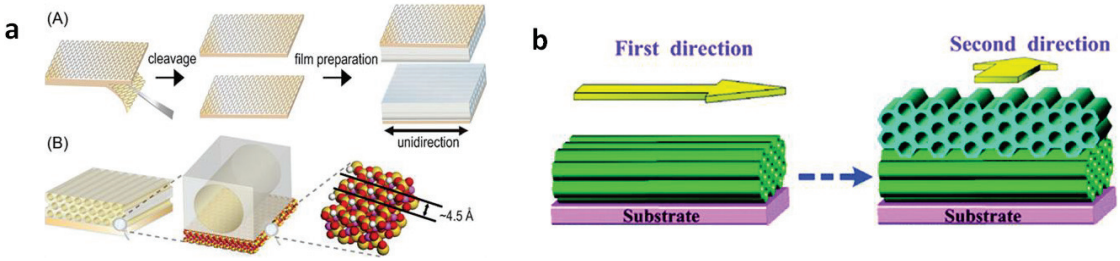

Figure 3.1 (a) Schematic illustration of using mica ($K_2Al_4(Al_2Si_6O_{20})(OH)_4$) to unidirectionally align the mesochannels in a mesoporous silica film by EISA process.[118] (b) The shear force induced by a hot jet air flow was used to orient the precursor and surfactant solution before sol-gel process. Adapted from Ref.[123]

Long-range alignment in block copolymer template has been widely investigated recently, which can be achieved by a method, called directed self-assembly (DSA), using a distance of only a few periods on the substrate to direct the long-range order in block copolymer films.[124] There are two main different patterns on the substrates: topographic guiding patterns (graphoepitaxy),[21, 125-127] which uses substrate surface with patterns fabricated by top-down lithography to assist the assembly of microdomains of block copolymer, and chemical guiding patterns (chemical epitaxy),[128-130] which utilizies chemical heterogeneity on substrate surface to direct the alignment of block copolymer domains. Cylindrical or lamellar alignment has been achieved in block copolymers with

cylindrical morphology by using DSA with both topographic guiding patterns[125, 131-135] and chemical guiding patterns.[136-138] As reported by S. J. Sibener group[125] in 2004, aligned parallel arrays of cylinders in polystyrene-block-poly(ethylene-alt-propylene) (PS-*b*-PEP) have been achieved on topographically patterned silicon nitride substrates fabricated using e-beam lithography as shown in Figure 3.2a. And also in 2009, T. P. Russell and coworkers[126] reported using a sapphire single crystal surface to guide the perpendicular alignment of PS-*b*-PEO diblock copolymers as shown in Figure 3.2b. The alignment of lamellae microdomain in PS-b-PMMA was achieved in Nealey's group in 2003 using chemically guiding patterns as shown in Figure 3.2c, d.

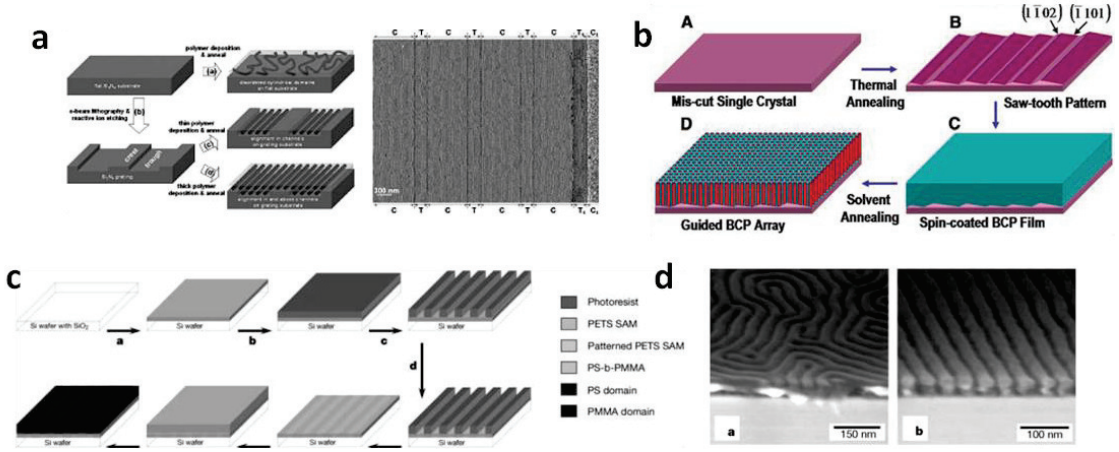

Figure 3.2 (a) Schematic illustration of the process to achieve aligned parallel arrays of cylinders in diblock copolymer on patterned substrate fabricated by e-beam lithography. Adapted from Ref.[125] (b) Schematic illustration of perpendicular oriented cylindrical microdomain in block copolymer on a sapphire single crystal surface. Adapted from Ref.[126] (c) Schematic representation of creation of chemically nanopatterned surfaces and alignment of PS-*b*-PMMA lamellae microdomains on chemically patterned surfaces. Adapted from Ref.[130] (d) SEM cross-section images of PS-*b*-PMMA lamellae on unpatterned and chemically patterned surfaces. Adapted from Ref.[130]

Here, we use the technology of supercritical fluids infusion process[85, 91-92, 95] to fabricate mesoporous silica films with massively aligned channels by decoupling the ordering generation in polymer template from silica netwok formation. By combination of top-down lithography with bottom-up self-assembly, the orientation of block copolymer templates which contain cylindrical morphologies can be directed to achieve long-range alignment prior to replication. Substrates with micron-scale line patterns fabricated by photolithography, a well developed method, can be used to direct the self-assembly of a block copolymer (PS-*b*-PtBA) to achieve cylindrical 1-D alignment. We further use the supercritical CO_2 infusion process to precisely replicate all of the structural details into mesoporous silica films to create 1-D aligned mesochannels.

3.2 Experimental

3.2.1 Formation of patterned substrate

The photo-resist used in the process is NR9-1000PY, a negative lift-off resist. Spin-coating was performed on a Brewer Science CEE 100CB Spin Coater with the spinning rate 3000 rounds per minute (rpm) for 60 seconds using silicon wafers (type-doping: N/Sb, orientation: <111>) as substrates. Pre-exposure baking was set at 150^{o}C for 60 seconds.

Photolithography was performed on a SUSS MA6 Mask Aligner with a quartz mask containing line-patterns. The UV exposure time was 30 seconds with intensity of 388 mJ/cm^2. The post exposure bake was conducted at 100^{o}C for 60 seconds. The substrates were then developed in the RD6 developer for 12 seconds, rinsed with distilled water and then dried in N_2.

Reactive ionic etching (R.I.E.) was performed on a STS Vision 320 Reactive Ion Etch system. CF_4 plasma was used for silicon etching with the process pressure of 5 mT, the RF set point at 100 W, the stabilization time for 15 sec, the CF_4 flow at 30 sccm. The etching rate for silicon was ~9.24 nm per minute measured by AFM. The whole process is demonstrated in Figure 3.3.

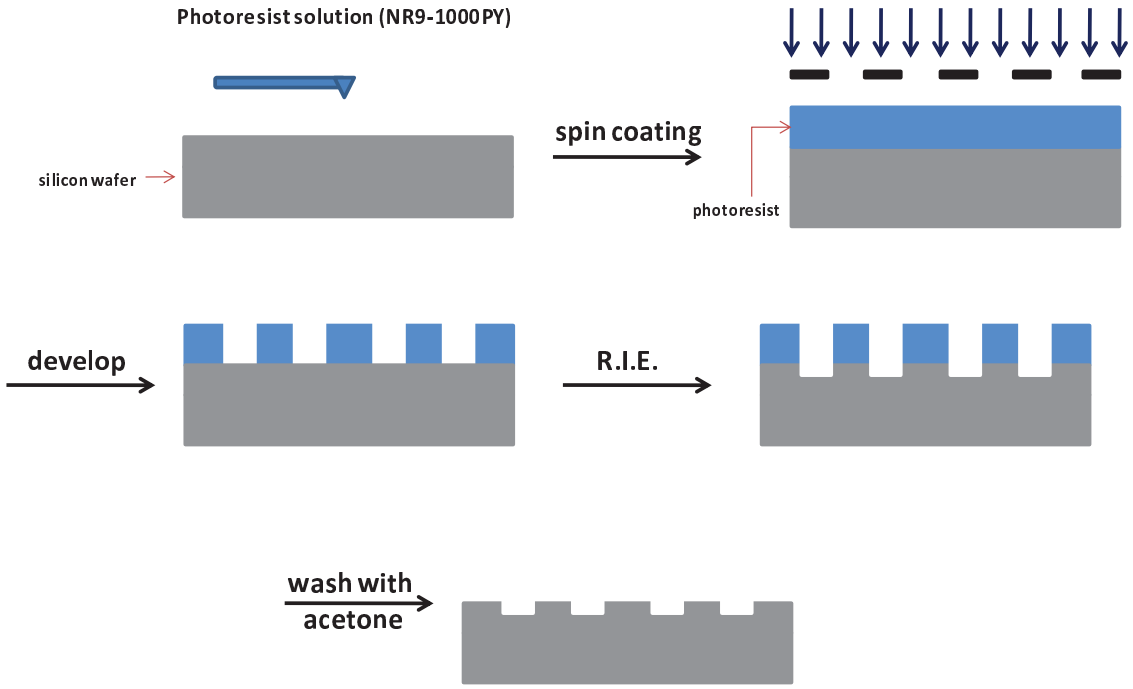

Figure 3.3 Schematic illustration of photolithography for patterned substrate fabrication.

3.2.2 Formation of block copolymer templates with long-range aligned cylinders

PS-*b*-PtBA (49.3K PS-*b*-PtBA , 76.9% PtBA, PDI=1.21, Table 1.1 P5) was used in this study which gives cylindrical morphology. The same procedure for block copolymer spin-coating and annealing was used on patterned substrates as Chapter 2. The spin-coating solvent used was THF/Toluene (1:1) mixture with the polymer concentration of around 3 wt%. After spin-coating with 3000 rpm from this solution, a PS-*b*-PtBA film with the film thickness of 180 nm was generated. Solvent annealing (200 µl in 250 ml jar) was used to achieve long-range alignment in PS-*b*-PtBA.

3.2.3 Formation of mesoporous silica films with massively aligned channels

Supercritical CO_2 infusion was used to replicate the long-range alignment in PS-*b*-PtBA films into mesoporous silica films to achieve bicontinous structure. The procedure was the same as Chapter 2.

3.2.4 Characterization

Atomic force microscopy (AFM) was performed on a Digital Instruments Dimension 3000 scanning microscope in tapping mode to give topographic and phase images.

Transmission electron microscopy (TEM) was performed on a JEOL 2000FX electron microscope operating at 200 kV. The mesoporous silica films were scraped off the substrate with razor blades. The powders were then ground to form a dilute slurry with ethanol and dropped onto Formvar coated copper grids (Electron Microscopy Sciences). The transmission electron microscope was then used to observe the grids after drying in air.

Grazing incidence small angle X-ray scattering experiments were performed at the G1 station of the Cornell High Energy Synchrotron Source (CHESS) with the wavelength of X-rays as 1.4653 Å. The angle of incidence was chosen between the critical angles of the polymer or mesoporous silica films and silicon substrates to make sure that the collected scattered radiation is the representation of the entire film thickness. The scattered radiation was collected with a two-dimensional charge-coupled device (CCD) camera with image sizes of 1024 pixels by 1024 pixels with the sample to detector distance as 2399.7 mm.

The thickness of the films was measured by spectroscopic ellipsometer (Sopra Inc., GES5) and a profilometer (Dektak3).

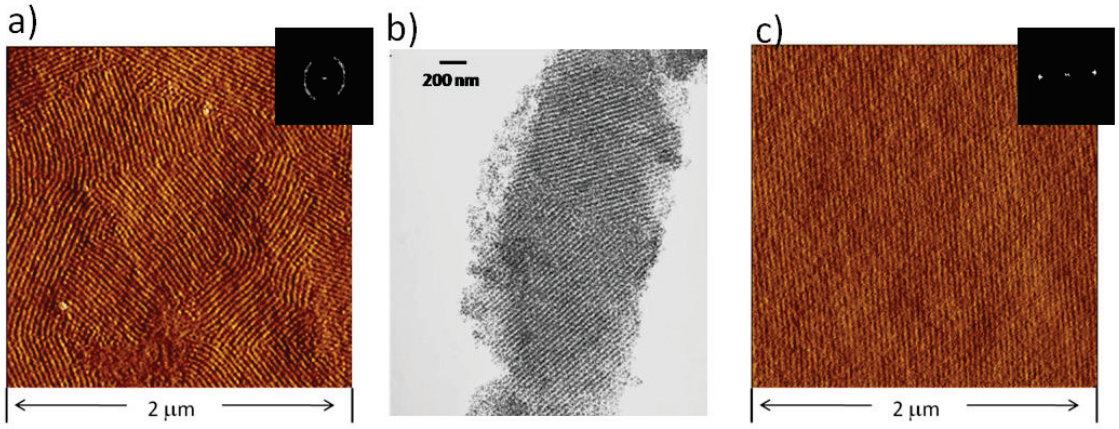

Figure 3.4 Topography-directed orientation of domains in block copolymer films. (49.3K PS-*b*-PtBA , 76.9% PtBA, PDI=1.21). (a) AFM phase images of PS-*b*-PtBA film (49.3K PS-*b*-PtBA , 76.9% PtBA, PDI=1.21) spin-coated from chloroform after solvent annealing (200 μl chloroform in a 250 ml jar) for 15 h. (b) TEM image of the corresponding mesoporous silica film replicated from the polymer template (image a) after supercritical CO_2 infusion and calcination. (c) AFM phase images of PS-*b*-PtBA film (49.3K PS-*b*-PtBA , 76.9% PtBA, PDI=1.21) spin-coated from 1:1 mixture solvent of Toluene and THF after solvent annealing (200 μl chloroform in a 250 ml jar) for 15 h with its Fourier Transform image.

3.3 Results and Discussion

3.3.1 Directed assembly of block copolymer templates for the fabrication of aligned mesochannels in silica films

PS-*b*-PtBA (49.3K PS-*b*-PtBA , 76.9% PtBA, PDI=1.21, P5 in table 2.1) after chloroform vapor annealing, which gives cylindrical morphology (Figure 2.7e), was used as the template to produce a mesoporous silica film with cylindrical channels as shown in Figure 2.9e. AFM images of the block copolymer films (Figure 3.4a) showed that most cylinders were oriented parallel to the substrate, which is thermodynamically preferred

for thick films, but randomly oriented in-plane. The TEM image (Figure 3.4b) of the mesoporous silica films also shows an obvious grain boundary after the replication of the block copolymer morphology. The in-plane order improvement in PS-*b*-PtBA templates was investigated using solvents for spin coating. A mixed solvent, consisting of equal parts THF and toluene, was used in this strategy. Figure 3.4c and Figure 3.5 show an increase of the grain size of the cylindrical morphology from less than 1 µm to over 5 µm. This grain size increase is due to the slow evaporation of the mix-solvent relative to chloroform, which reduces the chance of defect generation.

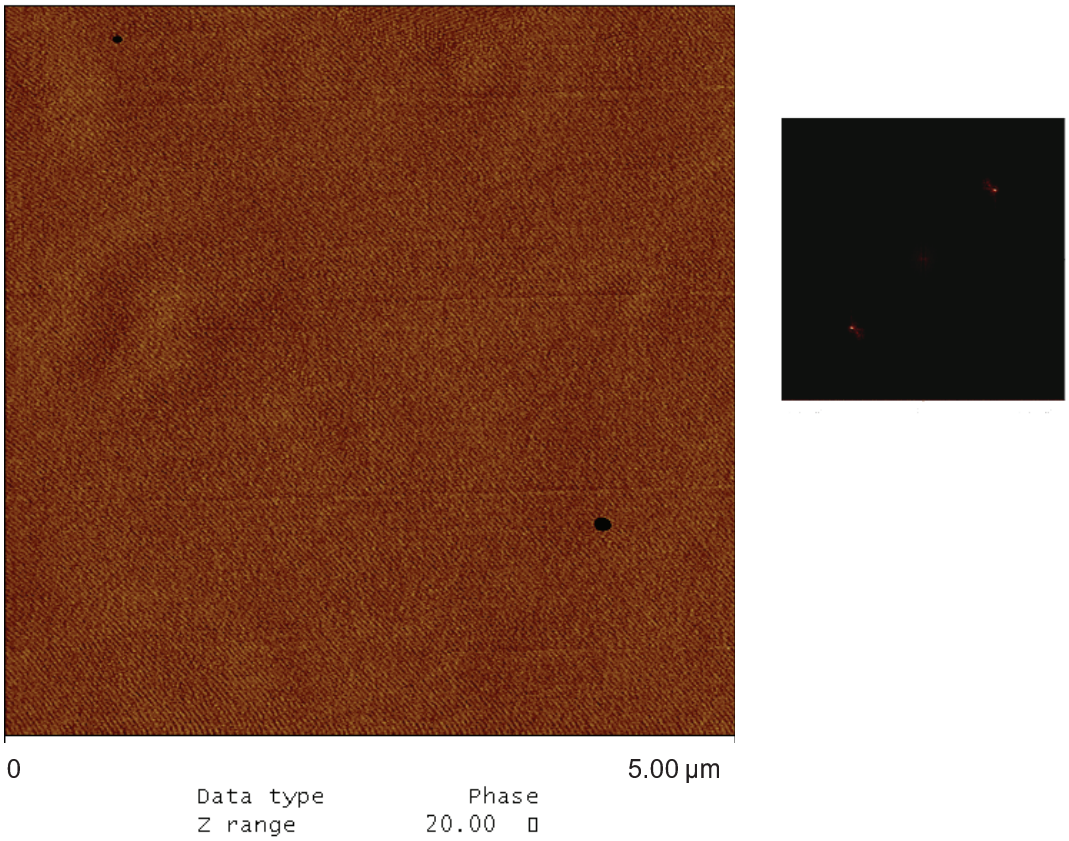

Figure 3.5 AFM phase image at the scale of 5 µm × 5 µm of PS-*b*-PtBA film (49.3K PS-*b*-PtBA, 76.9% PtBA, PDI=1.21) spin-coated from 1:1 mixture solvent of Toluene and THF after solvent annealing (200 µl chloroform in a 250 ml jar) for 15 h with its Fourier Transform image.

The use of topographic guiding alignment was then investigated in conjunction with slow solvent evaporation to achieve long-range alignment and orientation of the cylinders within PS-*b*-PtBA films. Silicon wafers with oxide thickness 25 nm (line-width 0.201 ± 0.018 micron, pitch length 0.473 ±0.005 micron), obtained from Lucent Technologies, Inc. were used for DSA. After spin-coating of the same solution used for the films shown in Figure 3.4c followed by chloroform annealing, the cylindrical domains of the polymer template were guided by the topographical patterns beneath the films as shown in the AFM images (Figure 3.6a, c), The long-range alignment of the cylinders was confirmed *via* Fourier transform (F.T.) of the AFM phase image (Figure 3.6b, d).

Additional DSA templates were fabricated in our laboratories as shown in Figure 3.3 with the line-widths as small as 500 nm and period of 1 micron were fabricated. The depth of the line patterns was tuned by changing the RIE time. Patterned line gratings on silicon wafers with depths of 75 nm were fabricated after etching under CF_4 for 8 minutes. (Figure 3.7a) A PS-*b*-PtBA film with a thickness of approximately 180 nm was spin-coated from a solution of 3 wt% PS-*b*-PtBA in THF: Toluene (1:1 weight ratio) onto the patterned substrate. Very well aligned cylinders were again achieved after overnight chloroform annealing. AFM characterization of the aligned film (3 μm by 3 μm) is shown in (Figure 3.7b) and also in Figure 3.8 for a 6 μm by 6 μm region. After replication of the template in supercritical CO_2 and 400^{o}C calcination, TEM was used to characterize the final structures of the mesoporous silica films. TEM images in Figure 3.9 show that well aligned channels were successfully replicated in the mesoporous silica films.

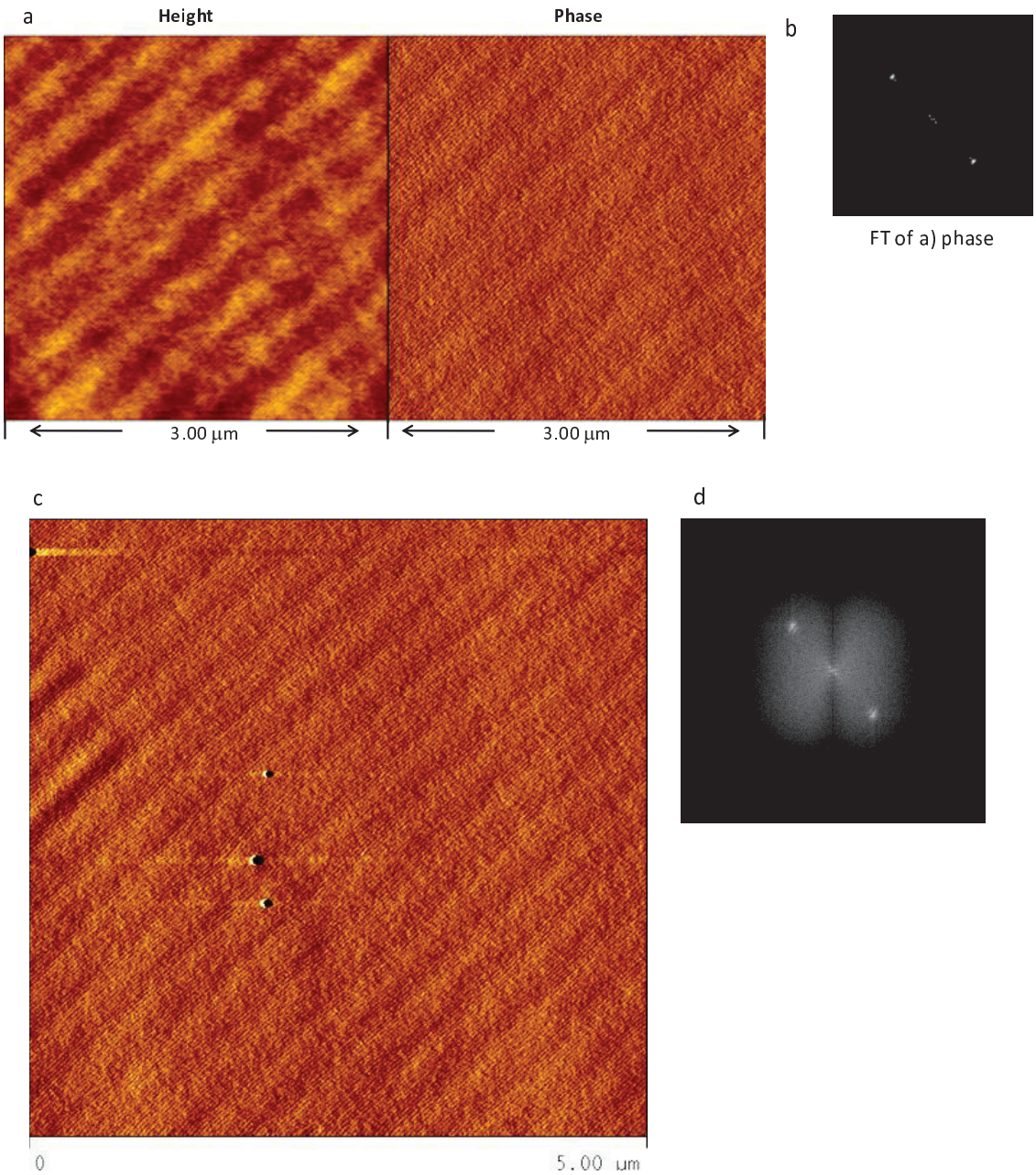

Figure 3.6 (a) AFM image (3 µm × 3 µm) of the topography of PS-*b*-PtBA film (180 nm) on the patterned substrate (with oxide pattern thickness of 25 nm, line-width of 0.201 ± 0.018 µm and pitch length of 0.473 ±0.005 µm from Lucent Technologies, Inc.) (b) Fourier Transform of the phase image in (a), (c) AFM phase image at the scale of 3 µm × 3 µm, (d) Fourier Transform of the image in (c).

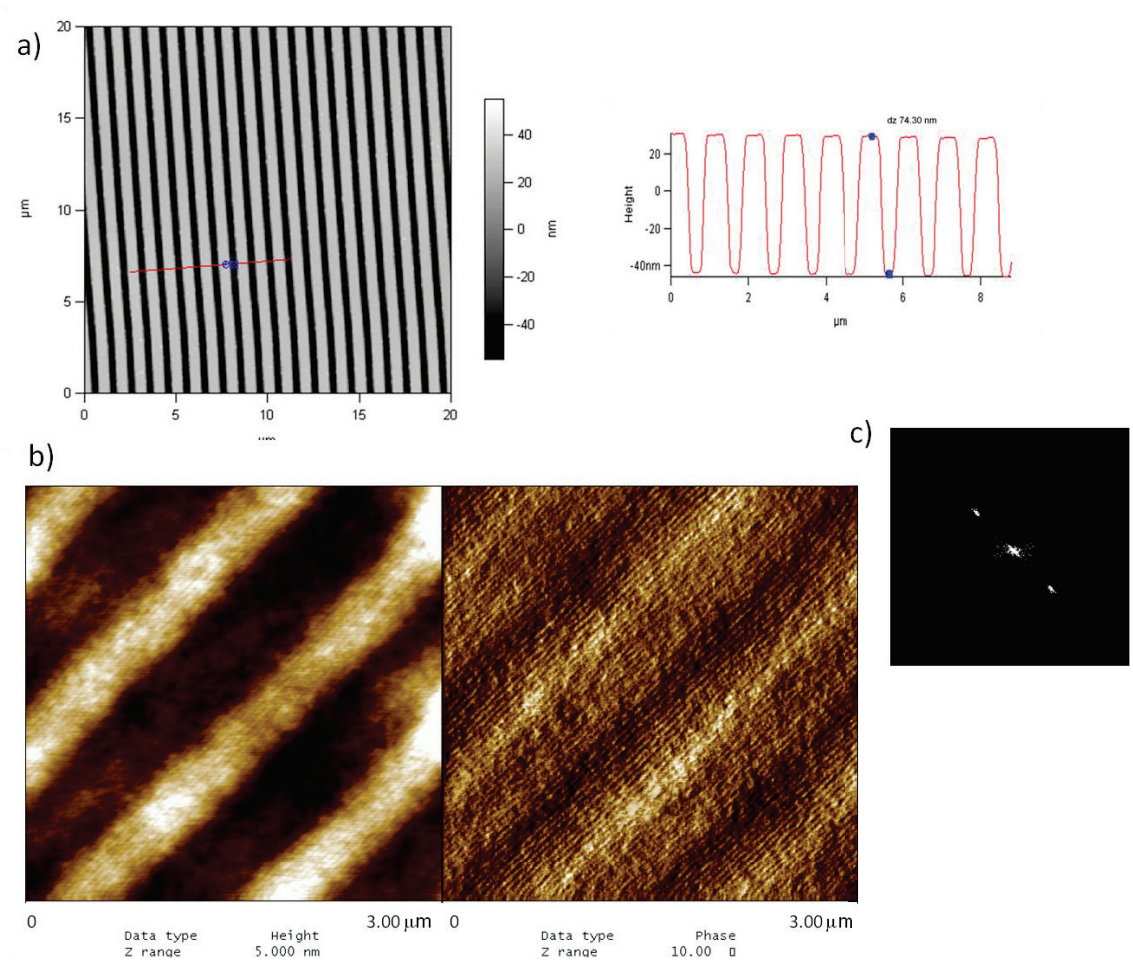

Figure 3.7 PS-*b*-PtBA block copolymer with cylindrical morphology aligned by an underlying patterned line gratings. (a) AFM height image of the line gratings on the silicon substrate with the thickness 74.3 nm, line-width of 500 nm and pitch length of 1000 nm fabricated by photolithography and AFM profile of the patterned substrate. (b) AFM image of the topography of PS-*b*-PtBA film on the patterned substrate at the scale of 3µm × 3 µm. (c) Fourier Transform of the phase image in (b).

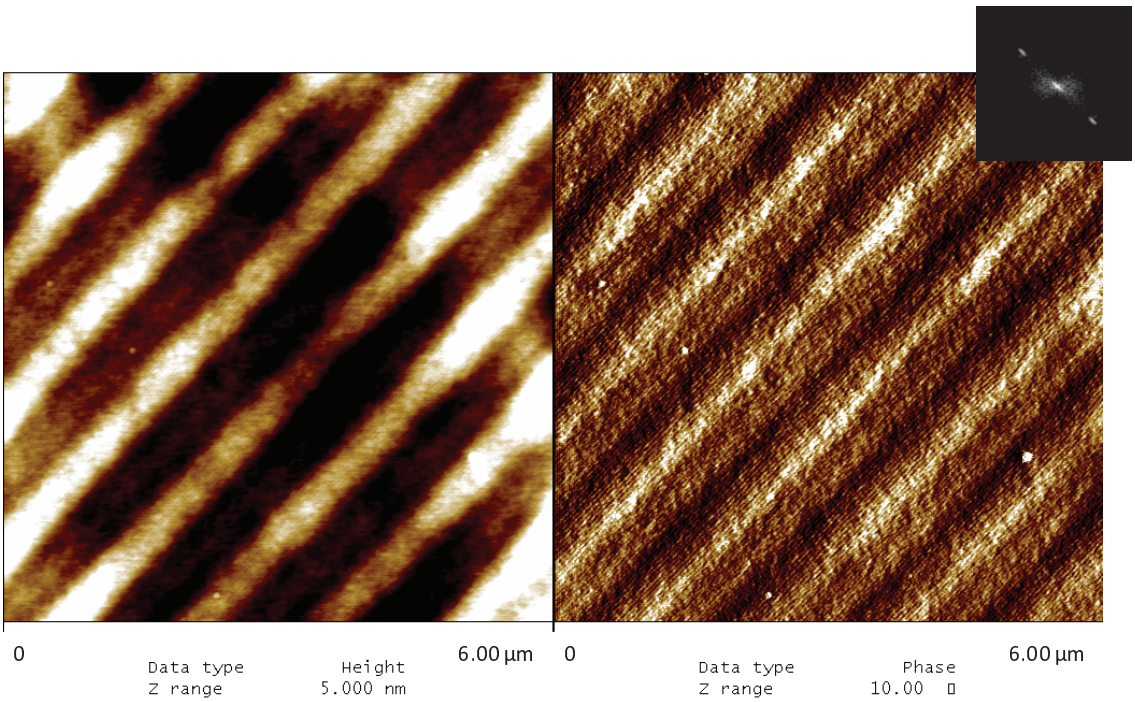

Figure 3.8 AFM image of the topography of PS-*b*-PtBA film on the patterned substrate at the scale of 6 µm × 6 µm with its Fourier Transform image.

3.3.2 GISAXS characterization of the long-range aligned mesoporous silica films

However, due to the fact that microscopy methods provide information over relatively small areas, we used grazing-incidence small-angle X-ray scattering (GISAXS) to provide information regarding large-area alignment. The sample was placed on a rotatable stage and aligned with X-ray beam at an angle, known as the grazing incidental angle (α) (Figure 3.10), which is between the critical angles of the polymer films (or mesoporous silica films) and silicon substrates to give strongest scattering signal across the whole film thickness. The bare lithographically patterned line gratings on the silicon substrate produced anisotropic scattering patterns on the GISAXS spectrum during rotation of the stage (ϕ) as shown in Figure 3.10) that must be accounted for (Figure 3.11). Intense scattering patterns arranged in an arc around the beam center were observed in the spectrum when the beam was exactly parallel to the lithographically

patterned line gratings; we define the relative ϕ value as 0 at this rotation (Figure 3.11c). When the stage was rotated by 90^{o} to render the x-ray perpendicular to the line gratings, a series of circular patterns line up in the q-z axes (Figure 3.11a and 3.11e). However, if the stage was rotated by only a very small angle away from the parallel direction, about 2^{o} in either direction, the circular scattering patterns moved away from the center and are rearranged as a tail emanating from the beam stop as shown in Figures 3.11b and 3.11d. The diffraction from grating has been studied previously by couple research groups.[139-140] We also used modeling to quantitatively describe the GISAXS-geometry scattering from the substrate with the lithographically patterned gratings. The results are shown in Figure 3.11f for different relative rotation angles, and match very well with the experimental results of the scattering from patterned gratings in Figures 3.11a, b, c, d and e.

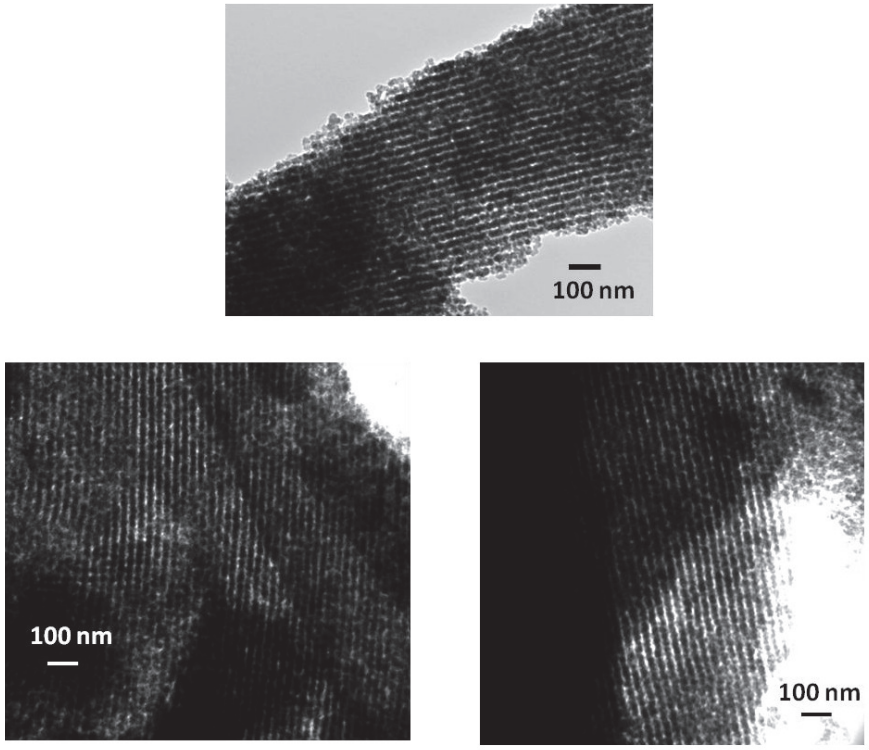

Figure 3.9 TEM images of mesoporous silica films with aligned channels replicated from block copolymer templates aligned using DSA.

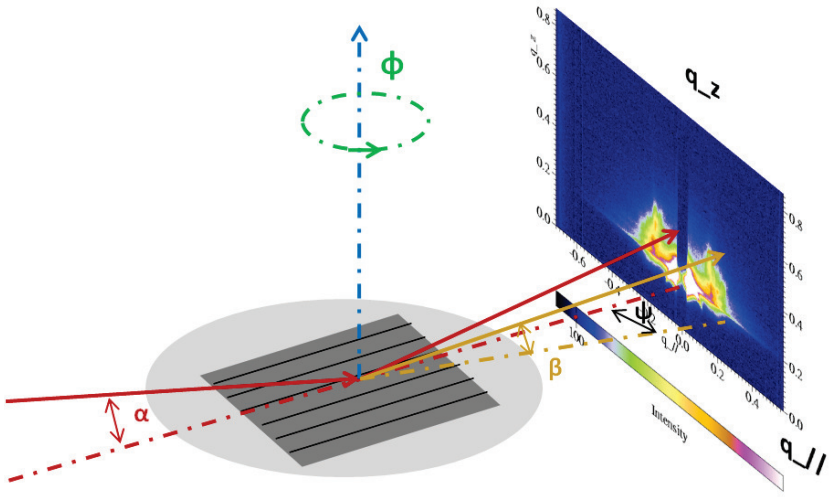

Figure 3.10 GISAXS set up for anisotropic substrate.

The same theory can also be applied to the scattering from the mesoporous silica films fabricated on top of the patterned silicon gratings. When the beam was parallel to the line gratings underneath, the scattering intensity from mesoporous silica film was apparent in the q_// direction, with a d-spacing of 35nm (Figure 3.11c). As the stage was rotated by a very small angle, such as 2^{o}, either counter clockwise or clockwise, the scattering from the mesoporous films became much more obvious, as shown in Figure 3.11b and 3.11d, because of the attenuation of the background scattering from the substrate line gratings. However, if the stage was rotated by a larger angle of approximately 45^{o}, no scattering from the mesoporous silica film was observed in Figure 3.11a and 3.11e, which indicates a lack of contrast in q_// direction. The anisotropic scattering patterns from mesoporous silica films indicates that the mesochannels in mesoporous silica films are all aligned in a parallel manner with the underlying gratings, and thus scattering patterns from mesoporous films was only observed in q_// when the X-ray beam was co-linear with the line gratings.

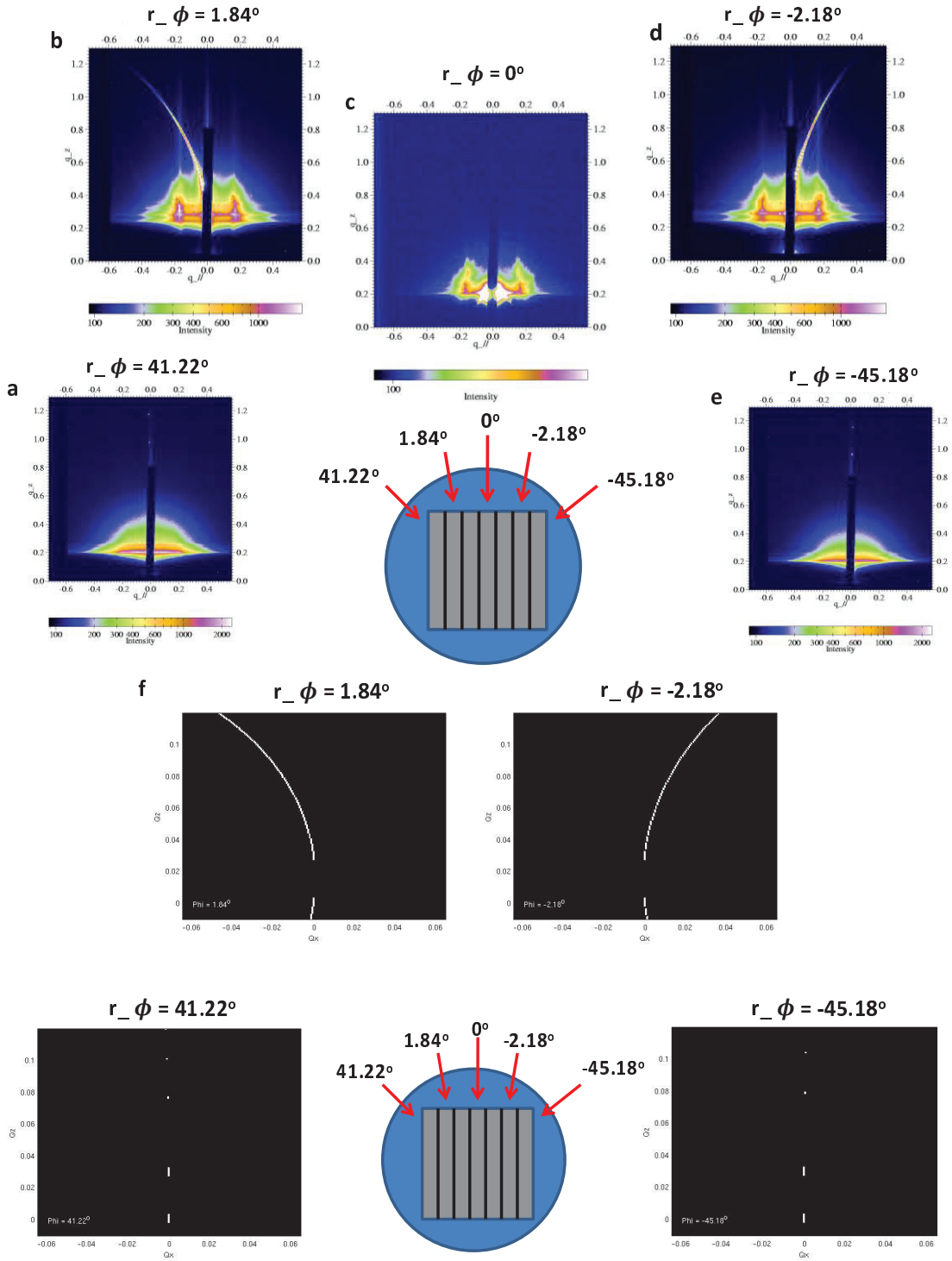

Figure 3.11 (a-e) GISAXS spectra for silica films with aligned cylindrical pore with different relative ϕ during azimuthal rotation of the sample stage. (f) Modeling results of GISAXS-geometry scattering from the substrate with lithographically patterned gratings during azimuthal rotation of the sample stage.

In order to confirm good alignment of the mesochannels within the film, the sharpness of the anisotropic transition for the scattering from the mesoporous silica film needs can be determined while rotating the stage at small angles (Figure 3.12a). When the relative rotation angle (r_ϕ) increased from 2^{o} to 15^{o}, the scattering from the mesoporous silica film decreased dramatically as shown in Figure 3.12a. This sharp transition indicates that the cylindrical mesochannels within the mesoporous silica film were well-aligned in the direction parallel to the underlying line gratings. The long range alignment can be quantified using the angular spread as reported in literature.[22, 141-142] Scattering intensity versus azimuthal angle relation curve is shown in Figure 3.12b, which gives the angular spread $\Delta\theta_{hwhm}$ (half width at half-maximum) $\approx$ 5.5. Similarly, the GISAXS method was also applied to block copolymer template PS-*b*-PtBA after solvent annealing but before silica infusion. As shown Figure 3.13, the similar alignment as that found in the mesoporous silica film was observed, although the scattering intensity was not as strong due to the weaker electron density contrast between PS and PtBA in comparison to that between air and silica.

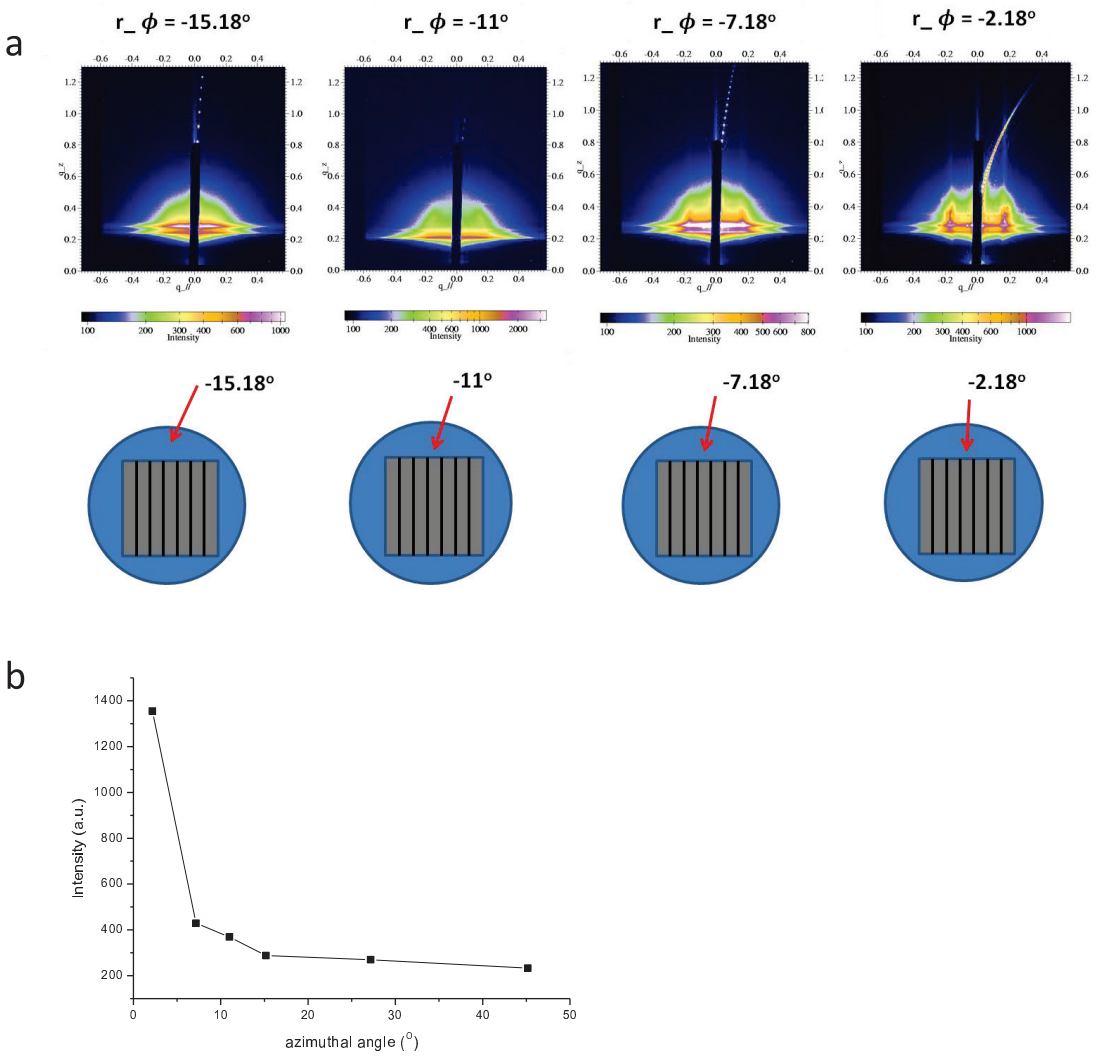

Figure 3.12 (a) Sharp transition of the scattering from mesoporous silica films during azimuthal rotation of the sample stage with small angles. (b) The plot of scattering intensity of the first order peak in GISAXS 1D profile versus azimuthal angle.

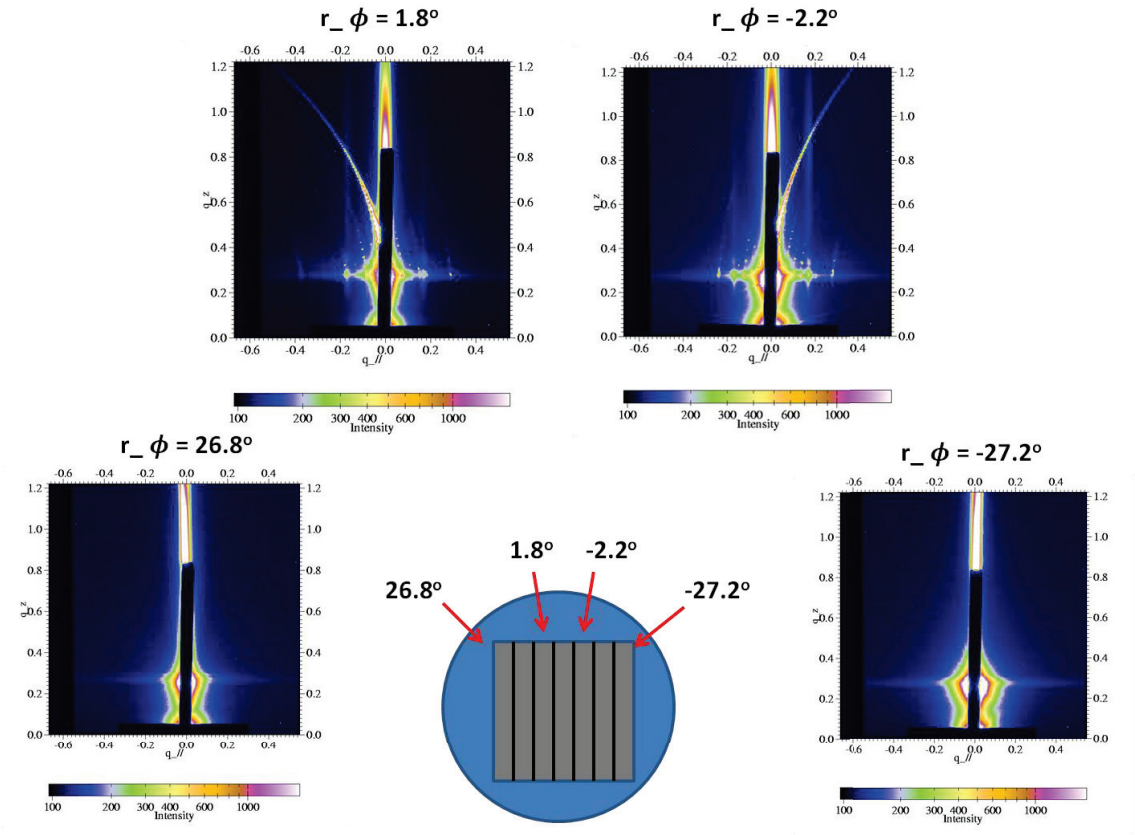

Figure 3.13 GISAXS spectra of aligned PS-*b*-PtBA films before supercritical fluid infusion with different relative ϕ during azimuthal rotation of the sample stage.

3.3.3 Control experiments for the reliability of the GISAXS measurements for confirmation of long-range alignment

Additional control experiments were conducted to determine the reliability of the GISAXS measurements for the long-range alignment. Two substrates with different line gratings were used. The first one has the grating with the same linewidth and pitch length as the standard substrate, but a much lower depth of 40 nm. The second substrate was fabricated by using a different mask with linewidth and periodical length double that of the original mask, while keeping the depth the same as the original (75 nm). Through analysis of the AFM image (Figure 3.14), it is apparent that if the depth of the line patterns were too shallow or the linewidth of the patterns was too large, the cylinders of

the PS-*b*-PtBA films of the same thickness were no longer guided by the underlying line gratings.

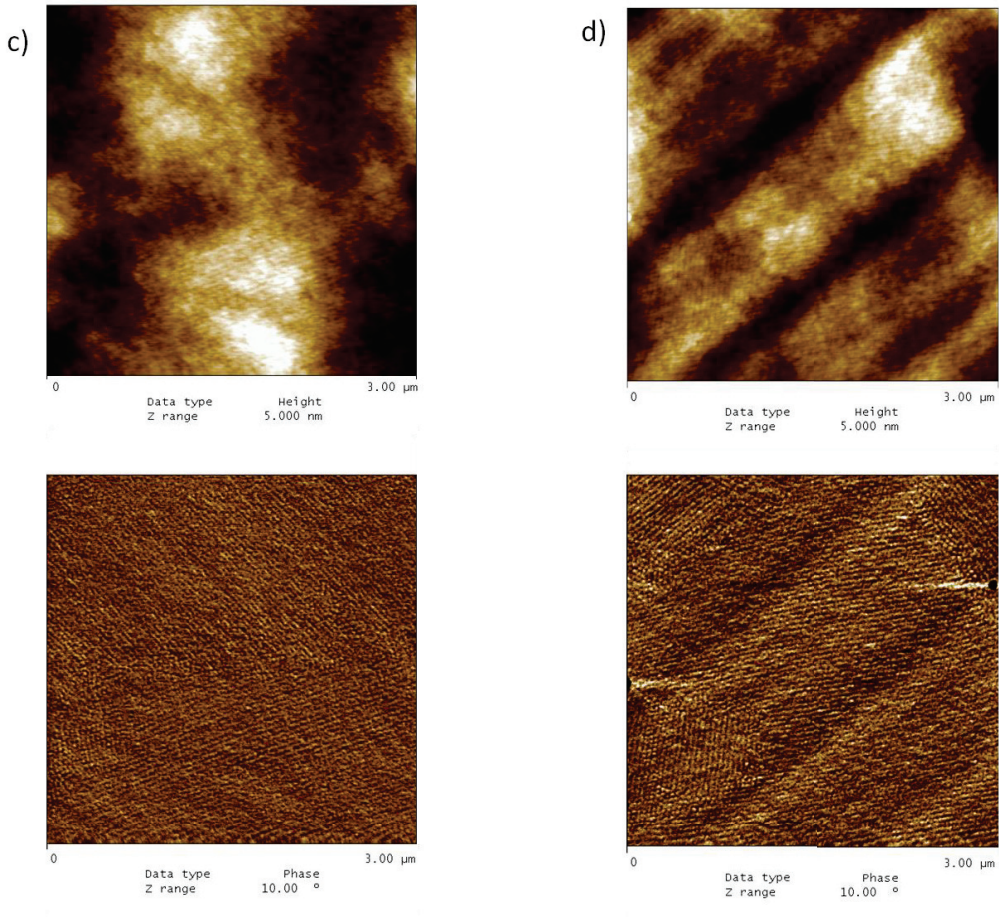

Figure 3.14 (a, b) AFM height images of the patterned substrate silicon wafers (Control I, Control II) fabricated by photolithography. And AFM profiles of the patterned substrate. (c, d) AFM images of the topography of PS-*b*-PtBA film on the patterned substrates (Control I, Control II).

Mesoporous silica films replicated using the same strategy in supercritical CO_2 from the two control templates were also characterized by using GISAXS at different r_ϕ. As shown in Figure 3.15, when r_ϕ was equal to 0^o, beam direction is parallel to the underneath line-patterns, strong scattering from the mesoporous silica films were

observed in all three substrates. When r_ϕ was equal to orthogonal to the underlying substrate patterns, there was no scattering from the standard sample, but strong scattering persisted from the control substrates (Figure 3.15). The presence of scattering along all directions of the unaligned films, combined with the anisotropic scattering in aligned film, indicate using GISAXS with azimuthal rotation to prove the achievement of long-range alignment in the standard film is reliable.

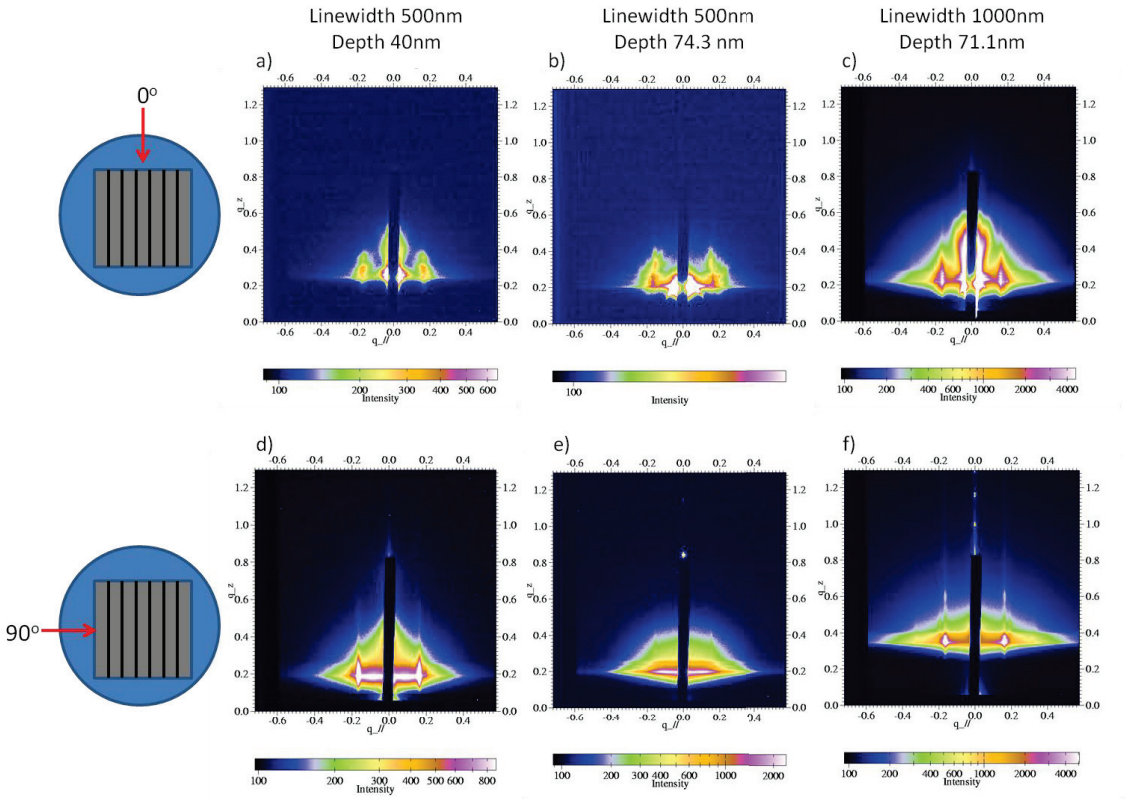

Figure 3.15 (a, b, c) GISAXS spectra for the mesoporous silica films on three substrates (Control I, standard, Control II), when r_ϕ was equal to 0o, beam direction is parallel to the underlying line-patterns. (d, e, f) GISAXS spectra for the mesoporous silica films on three substrates (Control I, standard, Control II), when r_ϕ was equal to orthogonal to the underlying substrate patterns.

3.4 Conclusion

A two-step method to fabricate mesoporous silica films with 1-D aligned cylindrical channels has been described. Cylindrical alignment in PS-*b*-PtBA films was first achieved by directed self-assembly using topographic guiding patterns. After 3-D replication process in supercritical CO_2, well aligned mesochannels can be generated in the final mesoporous silica films. The separated processes of template organization and silica network formation made the control of 1-D alignment much easier. GISAXS with azimuthal rotation was used to confirm the long-range alignment in addition to AFM and TEM analysis. Control experiments were also used to confirm the reliability of GISAXS measurement for alignment measurement.

CHAPTER 4

MESOPOROUS SILICA FILMS WITH BICONTINUOUS STRUCTURE REPLICATED FROM GYROID MORPHOLOGY IN BLOCK COPOLYMER TEMPLATES

4.1 Introduction

Mesoporous silica films with accessible channels attract enormous attention during the past decades, because of the potential industrial applications in separations,[143-145] photovoltaics,[146-147] proton transport,[82, 148] biomedicine devices,[149-150] and *etc*. Due to various morphologies can be generated through block copolymers self-assembly,[8, 151-155] mesoporous silica films with different pore-size and shape channels can be well fabricated using block copolymers as templates.[156] It has been well established in literature that a typical diblock copolymers can microphase separate into discrete morphologies, like spherical, cylindrical, lamellar and bicontinuous,[157] among which cylindrical morphology is a good candidate for providing mesoporous silica films with accessible channels. However, cylindrical pores in mesoporous silica films need to be either perfectly standing up or well aligned parallel to each other when laying down with few grain boundaries allowed for the through-film accessibility, which are difficult to be achieved especially for thick films.

Double-gyroid morphology bypasses these problems associated with the cylindrical morphology because of two continuous phases interpenetrating each other as shown in Figure 4.1b.[158] If this morphology can be achieved in mesoporous silica film, the pores are continuously accessible through the whole film thickness even with the presence of grain boundaries, making it an ideal candidate as separation membrane for

selective mass transport. To date, several methods have been used to produce bicontinuous mesoporous silica films by using silicon containing triblock copolymer. E. L. Thomas and coworkers[158] reported in 1999 the use of polyisoprene-*b*-poly(pentamethyldisilylstyrene)-*b*-polyisoprene (PI-*b*-P(PMDSS)-*b*-PI) to fabricate bicontinuous nanoporous and naorelief ceramic films as shown in Figure 4.1a. In 2004, E. J. Kramer and B. F. Chmelka reported the fabrication of mesoporous silica films with gyroid morphology through surfactant directing sol-gel process using nonionic surfactant, Brij-56, as the template shown in Figure 4.1c, d. H. W. Hillhouse group[159] also reported in 2007 using a nonionic surfactant, EO17-PO12-C14, as the structure directing reagent to fabricate bicontinuous silica films through EISA process as shown in Figure 4.1e, f. However, complicated synthesis is involved or strict conditioning for ordering control is required in those methods, which greatly hamper the possibilities for large scale manufacturing.

A supercritical fluid infusion process, previously developed in our group,[85, 91-92, 95, 156] was used as a very efficient method to fabricate robust and well-ordered mesoporous silica films through phase-selective condensation of silica and organosilicate[86] precursor in supercritical CO_2. Due to the properties it possesses, such as zero surface tension and high precursor solubility, supercritical CO_2 allows modest dilation of the polymer template to facilitate the diffusion of the reagents and by-products during the silica condensation without destroying the nanostructures of the template, thus allowing precise translation of all the structure details of block copolymer into mesoporous silica, especially good and efficient for thick films. In this process, the ordering step for block copolymer templates is completely decoupled from the silica condensation for inorganic

network formation, thus all strategies developed by polymer community for ordering soft block copolymer template can be easily and directly transplanted into metal oxide films formation, like different annealing methods, selective UV exposure for direct dual-tone patterning[92] and directed self-assembly. By tuning the parameters, including the molecular weight (M_n), Flory's interaction parameter (χ) and volume fraction (f),[157] the gyroid region in the diblock copolymer phase diagram can be easily reached with the assistance of a simple solvent annealing process. The double gyroid morphology of block copolymer template can then be replicated into silica to obtain bicontinuous nanochannels in mesoporous silica films through the supercritical CO_2 infusion process.

Here, we report the use of a chemically amplified block copolymer system, poly(styrene-*b*-*tert*-butyl acrylate) (PS-*b*-PtBA), which was previously used as a template in a direct dual tone patterning method in our group.[92, 156] We show that by tuning the molecular weight and volume fraction of the polymer template, gyroid morphology is achieved, with {121} planes preferentially parallel to the substrate confirmed by atomic force microscopy (AFM). Bicontinuous mesoporous silica film is then fabricated in supercritical CO_2 through the chemically amplified process together with the phase-selective silica condensation in PtBA block followed by high temperature calcination, confirmed by transmission electron microscopy (TEM) and grazing-incidence small-angle scattering (GISAXS).

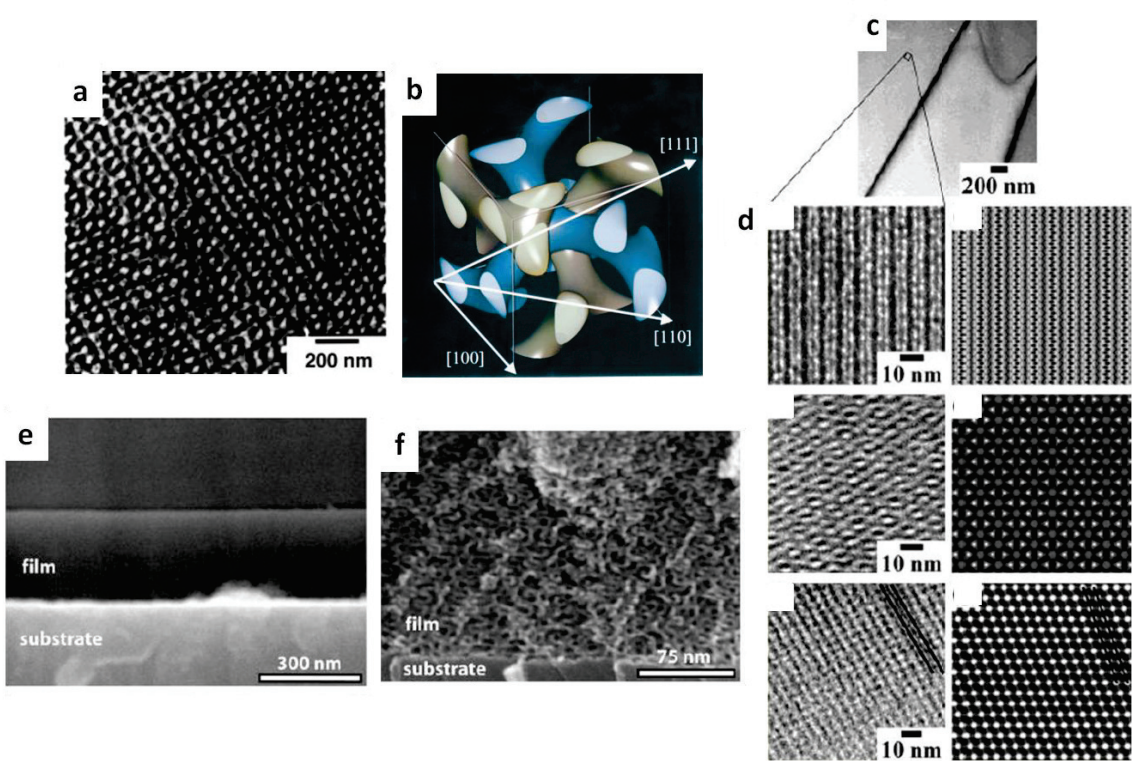

Figure 4.1 (a) Bright-field TEM image of PI-*b*-P(PMDSS)-*b*-PI triblock copolymer with double gyroid morphology after removal of PI network. Adapted from Ref.[158] (b) Schematic of the crystallographic unit cell of the double gyroid morphology. Adpated from Ref.[158] (c) Low-magnification TEM images for mesoporous silica films with double gyroid morphology ($Ia\bar{3}d$) edge and lamellae morphology (center). (d) Experimental and simulated TEM images from different plane projection for mesoporous silica films with bicontinous structure fabricated through surfactant directing sol-gel process using surfactant directing sol-gel process using Brij-56 as structure directing reagent (59-60 vol% $C_{16}EO_{13}$ and aged at 45°C). Adapted from Ref.[160] (e) Low-magnification (f) high-magnification FESEM images of mesoporous silica films using EO17-PO12-C14 as structure directing reagent through sol-gel process. Adapted from Ref.[159]

4.2 Experimental

4.2.1 Materials

Tetraethylorthosilicate (99%) were purchased from Acros Organics; PS-*b*-PtBA was synthesized by Atom Transfer Radical Polymerization[156, 161]; triphenylsulfonium triflate (TPST) were purchased from Sigma-Aldrich.

4.2.2 Formation of block copolymer film template with gyroid morphology

325nm thick polymer films was generated by spin coating onto silicon wafers at 2500 rpm for 60s using a 2 wt% solution of PS-*b*-PtBA, which has total molecular weight of 20k and weight percentage of PtBA of 65% with PDI as 1.30, in chloroform with 5 wt% TPST (to polymers). Gyroid morphology was formed in PS-*b*-PtBA films after a solvent annealing process: 150 μl of chloroform was put inside of a closed 250 ml jar with the presence of the polymer films on the silicon substrates for 15 hours.

4.2.3 Infusion of silica alkoxide precursors

As reported earlier,[85, 91-92, 94-95] ordered mesoporous silica film can be prepared from supercritical carbon dioxide infusion process by selective condensation of silicon alkoxides precursor in hydrophilic domain. Upon UV flood exposure (254nm) at room temperature for 30 seconds to generate acid was generated from photoacid generator (TPST). The acid then deprotected PtBA into PAA in the hydrophilic domain by PEB at 60^{o}C inside of a sealed 150 mL reactor. At the same time, 62 mL of carbon dioxide (with the pressure of 68.9 bar at room temperature) was injected into the reactor together with a 10 μL tetraethyl orthosilicate (TEOS) precursor. The reactor was then heated up to 60^{o}C to reach a final pressure of 103 bar, above the critical point of carbon dioxide, for two hours. After 400^{o}C calcination for 6 hours in air with temperature ramp rate of 1.56°C/min, a uniform mesoporous silica film was generated.

4.2.4 Characterization

For polymer synthesized by ATRP, Gel permeation chromatography (GPC) was used to measure the PDI and molecular weight. GPC was performed in THF at a flow rate of 1.0 mL/min using polystyrene as standards. Two detectors, a K-2301 refractive

index detector and a K-2600 UV detector and a column bank which consisted of two Polymer Labs PLGel Mixed D columns at 40^{o}C will be used.

1H nuclear magnetic resonance (1H NMR) spectra was be used to measure the ratio of two blocks and also molecular weight, which was acquired on a Bruker DPX300 NMR spectrometer (300 MHz) in deuterated chloroform.

Atomic force microscopy (AFM) was performed on a Digital Instruments Dimension 3000 scanning microscope in tapping mode to give topographic and phase images.

Transmission electron microscopy (TEM) was performed on a JEOL 2000FX electron microscope operating at 200 kV. The mesoporous silica films were scraped off the substrate with razor blades. The powders were then ground to form a dilute slurry with ethanol and dropped onto Formvar coated copper grids (Electron Microscopy Sciences). The transmission electron microscope was then used to observe the grids after drying in air.

Grazing incidence small angle X-ray scattering experiments were performed at the G1 station of the Cornell High Energy Synchrotron Source (CHESS) with the wavelength of X-rays as 1.4653 Å. The angle of incidence was chosen between the critical angles of the polymer or mesoporous silica films and silicon substrates to make sure that the collected scattered radiation is the representation of the entire film thickness. The scattered radiation was collected with a two-dimensional charge-coupled device (CCD) camera with image sizes of 1024 pixels by 1024 pixels with the sample to detector distance as 2399.7 mm.

The thickness of the films was measured by Spectroscopic ellipsometer (Sopra Inc., GES5) and profilometer (Dektak3).

4.3 Results and discussion

4.3.1 Formation of double gyroid morphology in polymer template

Double gyroid morphology needs to be achieved in the block copolymer template first. PS-*b*-PtBA copolymers with different molecular weight and volume fraction can be synthesized by atom transfer radical polymerization (ATRP).[156] The block copolymer with a total molecular weight of 20k, a PtBA weight percentage of 65% and a PDI of 1.30 was picked as the candidate to yield gyroid morphology, a very unique morphology in di-block copolymer phase diagram.[157]

We prepared the PS-*b*-PtBA film by spin-coating from a 2 wt% solution of the copolymer in chloroform solution to yield a film thickness of 325 nm. We then investigated the morphology development using solvent annealing,[10-11, 13-16, 162-164] which is a very efficient method especially for block copolymer with higher glass transition temperature (Tg). Chloroform was chosen as the solvent for PS-*b*-PtBA annealing, which is a good solvent for both polystyrene (PS) and PtBA domains with a solubility parameter, δ(SI), of 18.7. Dilute chloroform vapor with the concentration of 150μl chloroform in a 250ml jar for 16 hours was selected as the annealing protocol. Figure 4.2 shows the AFM characterization of the surface topography of the polymer film template after chloroform annealing, which shows specific patterns only observed in gyroid morphology with [211] plane parallel to the substrate, similar as the simulated results reported in literature.[160] The inner structure of the polymer film also need to be characterized to rule out the possibility that the morphology only formed on the film surface. To characterize the inner

structure of the polymer template, the film was peeled off the silicon substrate by epoxy and cut using microtoming. RuO_4 was used to stain the PS block to increase the contrast for TEM characterization, with PS as the dark area and PtBA as the light area. Figure 4.3 shows the TEM images from the cross-section, which represent the [311] plane in double gyroid morphology with $I\alpha\bar{3}d$ space group symmetry similar as the simulated results reported in literature.[159]

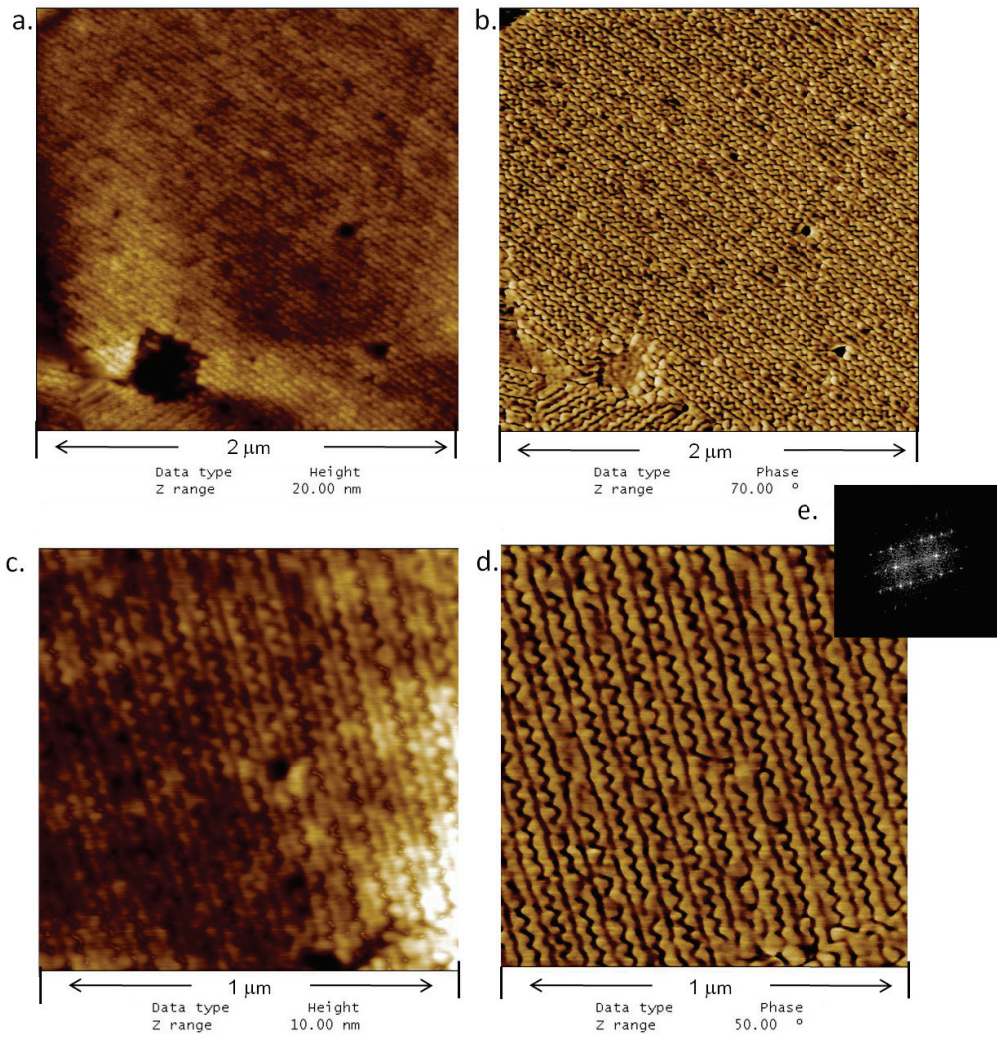

Figure 4.2 AFM characterization for the surface morphology of PS-*b*-PtBA films after solvent annealing for 16 hours (150 µl Chloroform in a 250 ml jar): height images with the area of 2 µm × 2 µm (a), 1 µm × 1 µm (c); corresponding phase images with the area of 2 µm × 2 µm (b), 1 µm × 1 µm (d). (e) Fourier Transform of the phase image in (d).

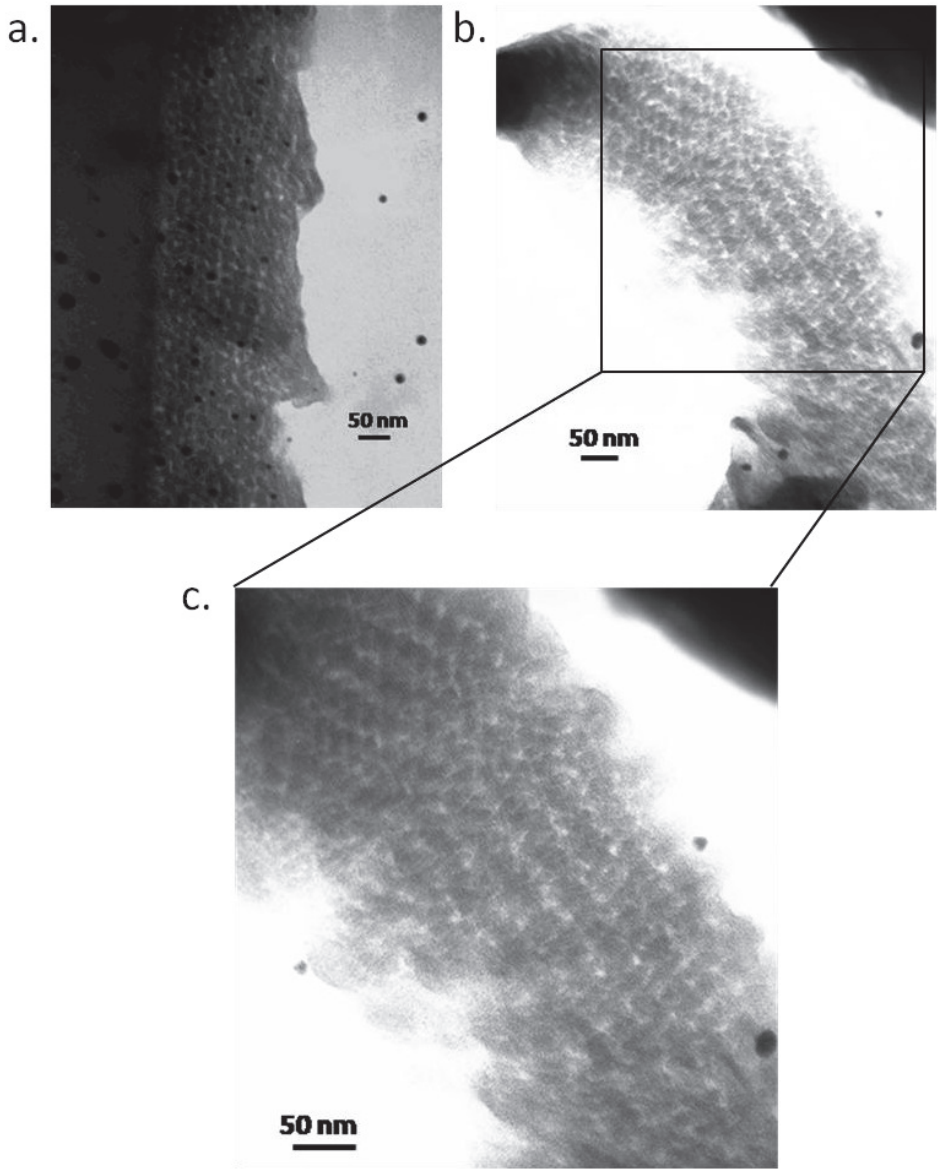

Figure 4.3 TEM characterization for the cross-section of PS-*b*-PtBA film after solvent annealing cut by microtoming with PS domain stained by RuO_4 vapor.

4.3.2 The replication of double gyroid morphology in $scCO_2$

The replication of this double gyroid morphology in PS-*b*-PtBA template into mesoporous silica film was then investigated, based on the method previously developed by our group called supercritical CO_2 assisted infusion process.[85, 91-92, 94-95, 156] For PS-*b*-PtBA copolymer template, this process involves a chemical amplification process and a

phase selective condensation of silica precursor (TEOS) in hydrophilic domain of the block copolymer template in supercritical CO_2. After exposure under UV lamp with the wavelength of 254nm for 20 seconds to generate triflic acid from triphenyl sulfonium triflate (TPST), a photoacid generator, the chemical amplification process, which involves acid-catalyzed PtBA deprotection into polyacrylic acid (PAA), and silica condensation in hydrophilic matrix, are processing at the same time in the medium of supercritical CO_2. Figure 4.4a shows infrared spectroscopy (IR) study of the chemical amplification process of deprotecting PS-*b*-PtBA into PS-*b*-PAA in the presence of 5 wt% TPST during the post exposure baking (PEB). Partial deprotection finished after baking at 60°C for 2 hours, proved by the shift of the carbonyl stretch peak relative to the protected film in IR. AFM was used to track the surface morphology change during the PEB as shown in Figure 4.4b. The phase image is not as clear as PS-*b*-PtBA films because of the weaker contrast of the modulus difference between PS and PAA compared with PS and PtBA. However, the electron density contrast is in the opposite way, where it is much higher in PS-*b*-PAA than PS-*b*-PtBA to give more scattering patterns in Grazing-incidence small-angle scattering (GISAXS). Only transmitted X-ray patterns in GISAXS were observed in the PS-*b*-PtBA film in Figure 4.5a, while not only transmitted X-ray patterns but also reflected patterns were observed in PS-*b*-PAA film, as shown in Figure 4.5b. This partial deprotection process makes the PtBA domain much more hydrophilic to trap enough acid and condense silica from TEOS in the hydrophilic domain.

The silica condensation process took place in a 150 ml high pressure reactor with 62 ml of carbon dioxide (68.95 bar at room temperature) and 10 μl TEOS. A final pressure of 105 bar was reached after heating the reactor up to 60°C to pass over the

critical point of CO_2 entering the supercritical fluid region. Over the course of two hours to form polymer/silica composite films and after subsequent high temperature calcinations to burn all organic compounds, a mesoporous silica film with bicontinuous channels was nicely generated. Here, the role of using PtBA through a chemically amplified process rather than directly using PAA is two-fold. These include the high solubility of PtBA in organic solvent for template film coating and relatively low Tg of the PtBA block, making it easier dilated in $scCO_2$ to facilitate the diffusion of reagents and by-products in and out of the template. Moreover, the use of PS-*b*-PtBA as the template also allows the direct duel-tone patterning of the final mesoporous silica films as reported in our group.[92]

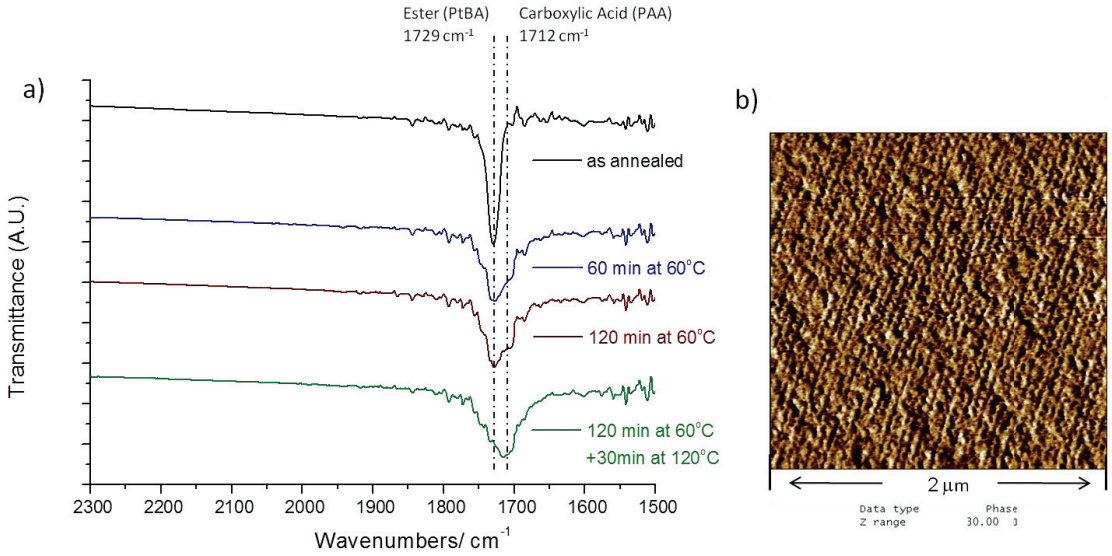

Figure 4.4 The deprotection process of PS-*b*-PtBA into PS-*b*-PAA with TPST after UV exposure during PEB tracked by IR (a). AFM phase image (b) for partially deprotected PS-*b*-PtBA films after PEB at 60°C for 2 hours.

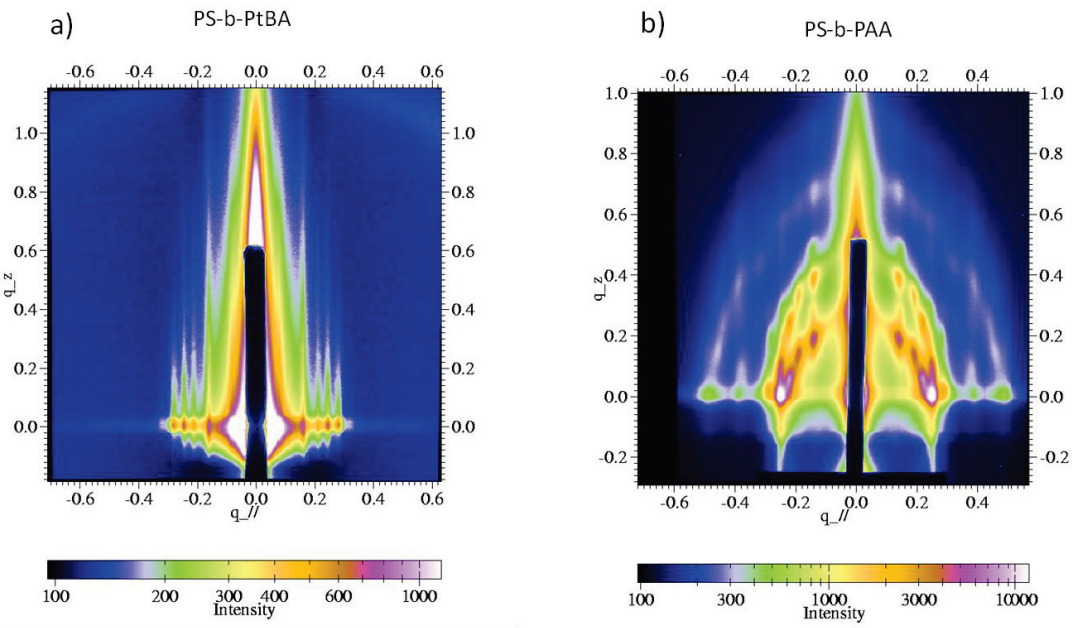

Figure 4.5 GISAXS spectra for PS-*b*-PtBA film after solvent annealing (a) and PS-*b*-PAA film deprotected from pre-ordered PS-*b*-PtBA film after UV exposure and PEB at 90^{0}C for overnight (b).

4.3.3 The characterization of bicontinuous mesoporous silica film

In order to characterize the bicontinuous structure of mesoporous silica films using transmission electron microscopy (TEM), the mesoporous silica films need to be scraped off the substrates and grounded into powders to generate small slices thin enough to be imaged. The powders were then suspended in ethanol, caught by Formvar coated copper grids (Electron Microscopy Sciences) and imaged under the microscope. Thin slices perpendicular to different axises were observed in TEM (Figure 4.6) with different volume projection views, [111], [011], [311] and [211], which are well matched with the simulated micrographs (Figure 4.7, reported by literature[159-160]). Interesting patterns were observed in those volume projections, especially in the [111] and [311] projections. [111] projection image is quite similar as reported previously[159-160, 165-167] and contains very typical pattern, like "wagon-wheel",[160] which is not common in other morphologies in

diblock copolymer system. The perfect agreement of the TEM volume projection view of mesoporous silica thin slices with the reported simulated images (Figure 4.7) confirms the achievement of double gyroid structures, $I\alpha\bar{3}d$, in our mesoporous silica films.

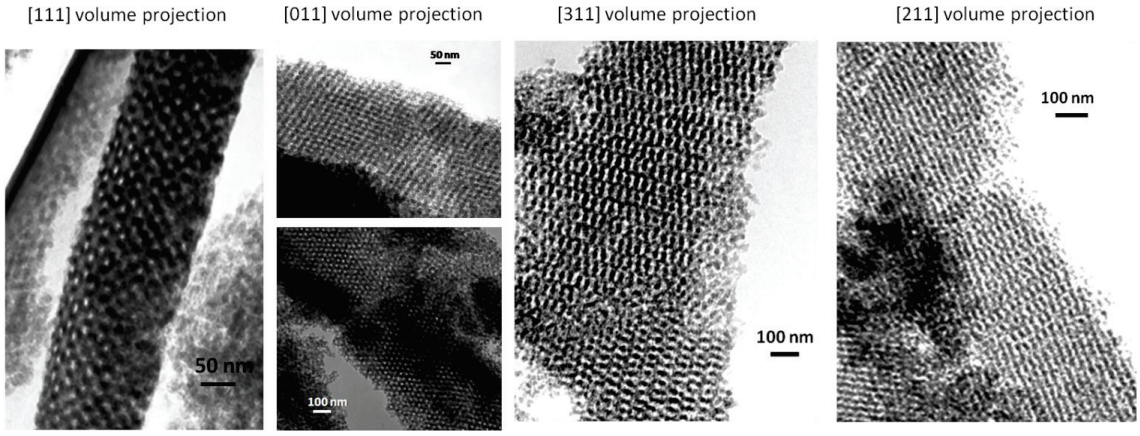

Figure 4.6 Bicontious mesoporous silica films with different plane volume projection after replication from a block copolymer template in supercritical CO_2, as characterized by TEM.

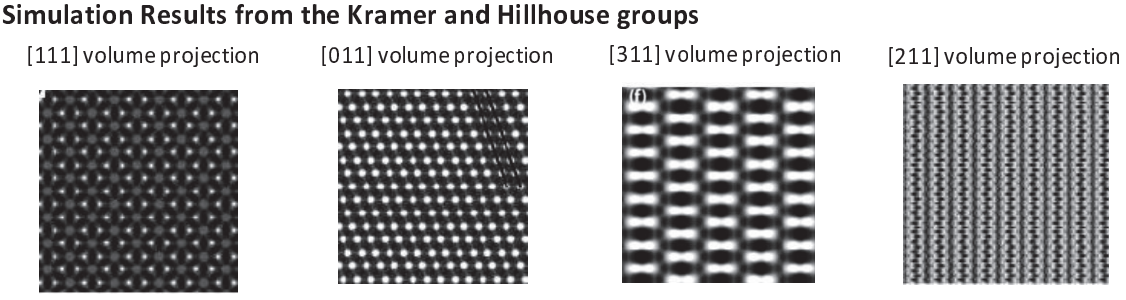

Figure 4.7 Simulation results for different volum projections. [111], [011] and [211] volume projection images are adapted from Ref,[160] [311] volume projection image is adapted from Ref.[159]

Since microscopy methods only give the localized structure information of the individual fragment of the mesoporou silica films, GISAXS need to be used to give the ordering information in a much larger scale and to assign the morphology and orientation. The GISAXS patterns from the polymer/silica composite films after infusion and the mesoporous silica films after calcination were shown in Figure 4.9a and 4.9b individually.

Clearly, two sets of diffraction patterns were observed in both GISAXS spectrums from the reflected and transmitted X-ray beams respectively, with lower one as transmitted patterns and relatively higher one as reflected patterns. Distorted wave Born approximation was used in T.Chang and M.Ree group to derive a GISAXS formula and calculate the GISAXS patterns for gyroid morphology,[168-169] as shown in Figure 4.8b.

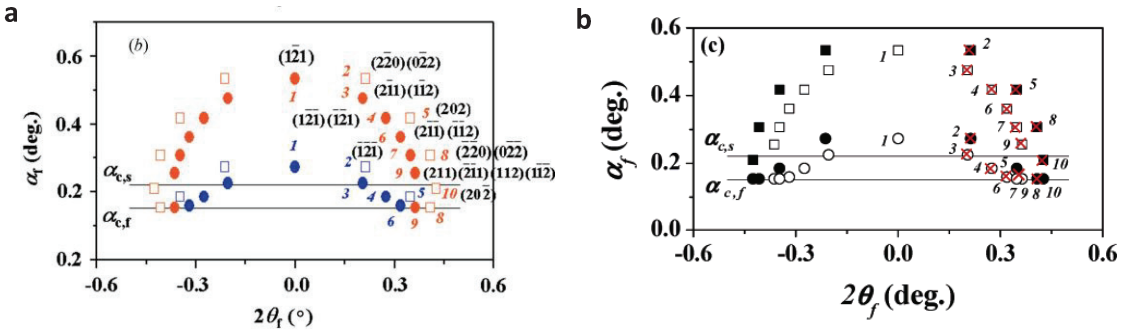

Figure 4.8 (a) Indexing of the scattering spots in the two dimensional SAXS pattern of the gyroid structures in the PS-*b*-PI diblock copolymer film, adapted from Ref. [169] (b) GISAXS pattern calculated for gyroid structure oriented with {121} plane parallel to the silicon substrate; the lattice parameter is 58.7 nm with open symbols as the diffraction peaks from the {121} plane and filled symbols for {220} plane, adapted from Ref. [168]

The GISAXS patterns obtained experimentally for polymer/silica composite films and mesoporous silica films matches well with the simulated GISAXS patterns for gyroid morphology. All diffraction peaks from reflective beams were confirmed as marked in Figure 4.9, except the diffraction spot from $(1\bar{2}1)$ blocked by the beamstop. The diffraction spots from {121} planes arranged along the inner ellipse with diffraction spots from {220} planes along the outer ellipse, which clearly shows that the gyroid structure oriented with {121} planes preferentially parallel to the substrate, as indicated by T.Chang and M.Ree group.[168] The AFM topography of the polymer template in Figure 4.2 also shows a pattern similar to the simulated [211] volume projection image (Figure

4.7), which again proves the orientation of the gyroid structure in the mesoporous silica films and also shows that the morphology was kept during the whole replication process. The lattice parameter a_G can be calculated from the undistorted q_|| value of the diffraction spots from $(20\bar{2})$ plane[168] as $a_G = \frac{2\pi \bullet 2\sqrt{2}}{q_{\_||,(20\bar{2})}}$. The lattice parameter a_G can be easily calculated as 58.4 nm from a $q_{\_||,(20\bar{2})}$ value of 0.3042 nm^{-1} as taken in the GISAXS spectrum. The similarity in the GISAXS spectrum between the as-infused polymer/silica composite films and the as-calcined mesoporous silica films shows that no significant film shrinkage during the calcinations step.

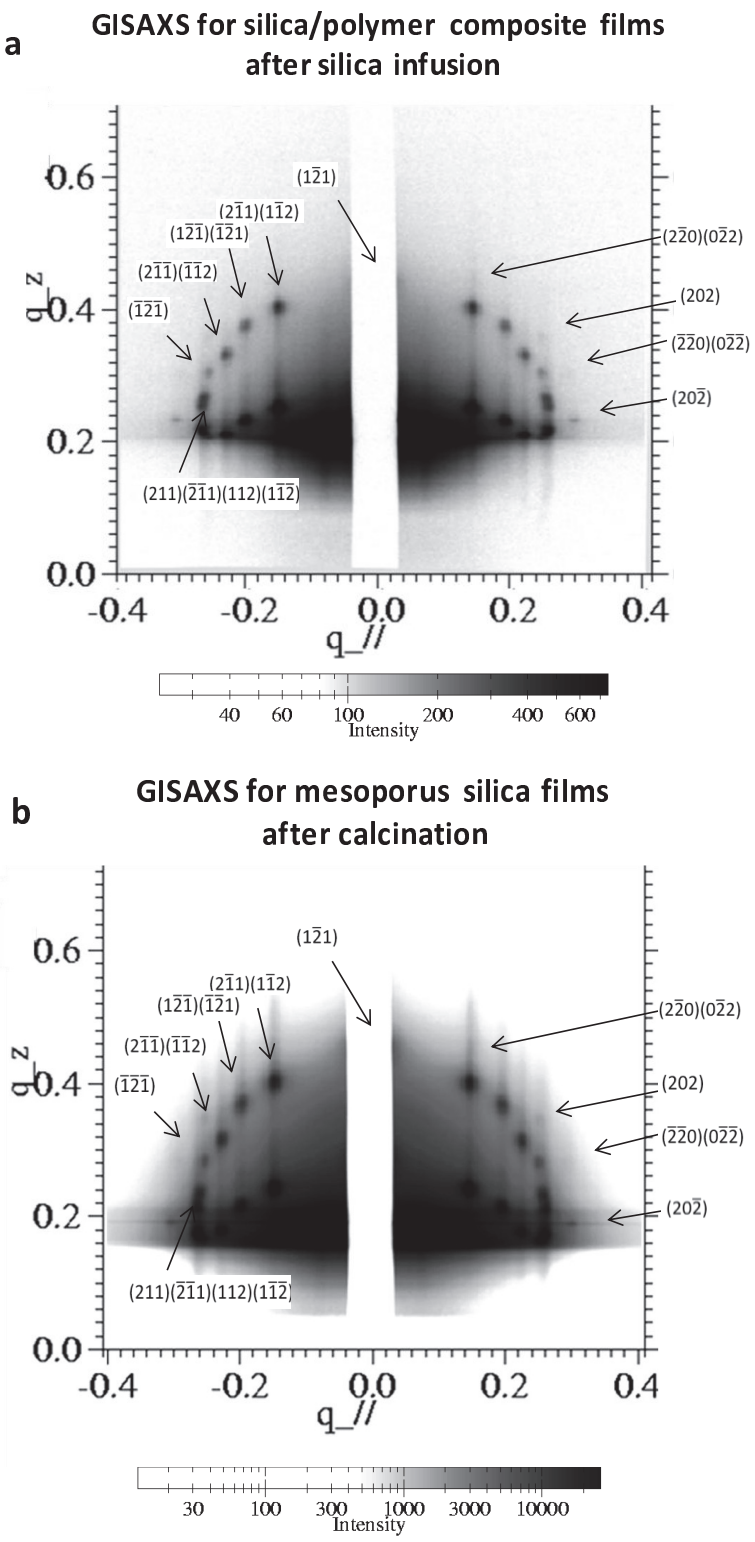

Figure 4.9 GISAXS characterization of the gyroid morphology in the as-infused silica/polymer composite film (a) and bicontinuous mesoporous silica film after calcination (b).

4.4 Conclusion

Well oriented bicontinuous mesoporous silica films have been fabricated in supercritical CO_2 based on 3-D replication of the gyroid morphology in chemically amplified block copolymer PS-*b*-PtBA films. By selective UV exposure of the PS-*b*-PtBA template, direct dual-tone patterning can be achieved in the mesoporous silica as reported previously in our group[92], which make our methods much more versatile over all the other processes for making bicontinuous silica films. The gyroid morphology with [211] face parallel to the substrate was formed in PS-*b*-PtBA film prior to silica condensation by using solvent annealing. With the assistance of PS-*b*-PtBA deprotection into PS-*b*-PAA together with silica condensation solely in hydrophilic domain, gyroid morphology in PS-*b*-PtBA templates was successfully replicated into silica films wth bicontinuous nanochannels in silica films, which shows no significant film shrinkage. IR, AFM, TEM and GISAXS were used to track the composite and morphology development in block copolymer films during annealing and chemical amplication process, as well as in replication process during the supercritical fluids infusion and calcination processes. The orientation of the gyroid morphology and important lattice parameters in bicontinous mesoporous silica films were confirmed and calculated through the GISAXS measurement. The bicontinuous mesochannels in the mesoporous silica film make it a perfect candidate for separation membrane and the applications for that are now under study.

CHAPTER 5

SELF-ASSEMBLY OF CHEMICALLY AMPLIFIED BLOCK COPOLYMERS WITH SMALL MOLECULAR ADDITIVES FOR PHOTO-INDUCED ORDER-DISORDER PATTERN FORMATION

5.1 Introduction

Block copolymer (BCP) can self-assemble into well-ordered periodic morphologies by tuning the number of repeat units (N), the segment-segment interaction parameter (Flory-Huggins parameter (χ)), and volume fraction (f) of each segment. [9] The segregation strength of a BCP system is determined by the interaction parameter together with the number of repeat unit, while it can also be increased by blending additives that can selectively interact with one block of the BCP system. For example,[37-38] the addition of a homopolymer that can selectively interact with one of the block copolymer segments can significantly enhance segregation strength as shown in Figure 5.1a. Furthermore, small functional molecules[39-40] or nanoparticles[41] (Figure 5.1b) that can interact preferentially with one of the blocks, can induce order in otherwise disordered BCPs, producing composite materials that have applications in a variety of areas including electronics,[21] photovoltaics[170-172] and photonics.[173-174]

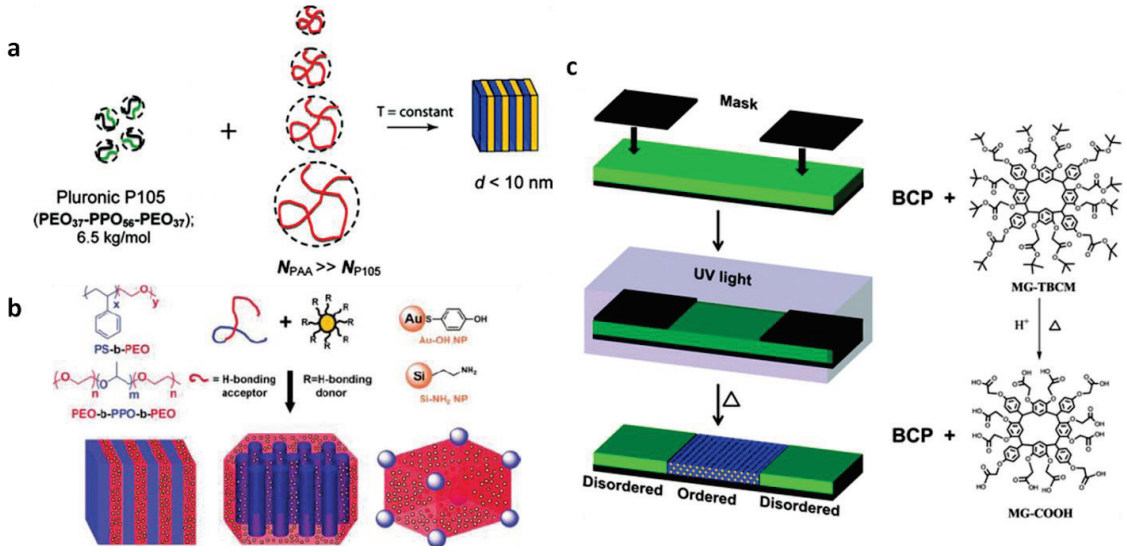

Figure 5.1 (a) Schematic illustration of ordering generation from a disordered block copolymer Pluronic P105 system blended with homopolymers PAA with different molecular weight. Adapted from Ref.[37] (b) Schematic representation of nanoparticle-driven assembly of block copolymers through hydrogen bonding. Adapted from Ref.[41] (c) Schematic illustration of photo-induced ordering transition through chemical transformation of MG-TBCM to MG-COOH with acid as catalyst generated from photo-acid generator. Adapted from Ref.[175]

Much effort has been directed towards achieving light-induced ordering or disordering transitions in block copolymer systems.[176-177] Such approaches would yield readily accessible pathways towards hierarchical structures in which nanoscale features are defined *via* block copolymer phase segregation and device level structures are defined by optical lithography. The most common approaches used to date have been based on photo-induced isomerization of azobenzene[176, 178-180] or anthracene[177, 181-183] moieties contained within a BCP chain segment. This approach relies on relatively small changes in the apparent segregation strength of the system upon isomerization and thus requires careful tuning of molecular weight such that the critical segregation strength for phase separation can be achieved upon light exposure. Since this will occur over a rather narrow range of molecular weight and because the small changes in the interactions

produce limited changes in segregation strength, the versatility of the technique in terms of available domain sizes and the degree of order is somewhat limited.

Recently we described an alternative path to achieve photo-induced order that was based on inducing strong interactions between an additive and one segment of a BCP by chemically amplified de-protection of the additive using a photo acid generator.[175] In that work we used poly(ethylene oxide)-block-poly(propylene oxide)-block poly(ethylene oxide), PEO-*b*-PPO-*b*-PEO triblock copolymers blended with a protected molecular glass bearing t-butyl groups at its periphery and the photo acid generator triphenylsulfonium triflate. Upon light exposure the protected molecular glass was deprotected to remove the t-butyl functionality and expose carboxylic acid functionality. These acid groups interact with PEO through a hydrogen bond and drive micro-phase separation in the exposed regions. While a photo-induced transition from a disordered system to one that exhibited strong segregation was readily achieved, some of the details of this particular system are not conductive to high resolution lithography. First, while PEO crystallization is suppressed in the ordered domains due to the strong interaction with the de-protected additive, it crystallizes in the disordered domains in the absence of the hydrogen bond interaction. Consequently in thin films there is a disparity in surface roughness between the smooth ordered domains and the disordered domains containing PEO crystallites. Second the low glass transition temperatures of the PEO and PPO components contribute to facile acid diffusion, which works against high resolution lithography.

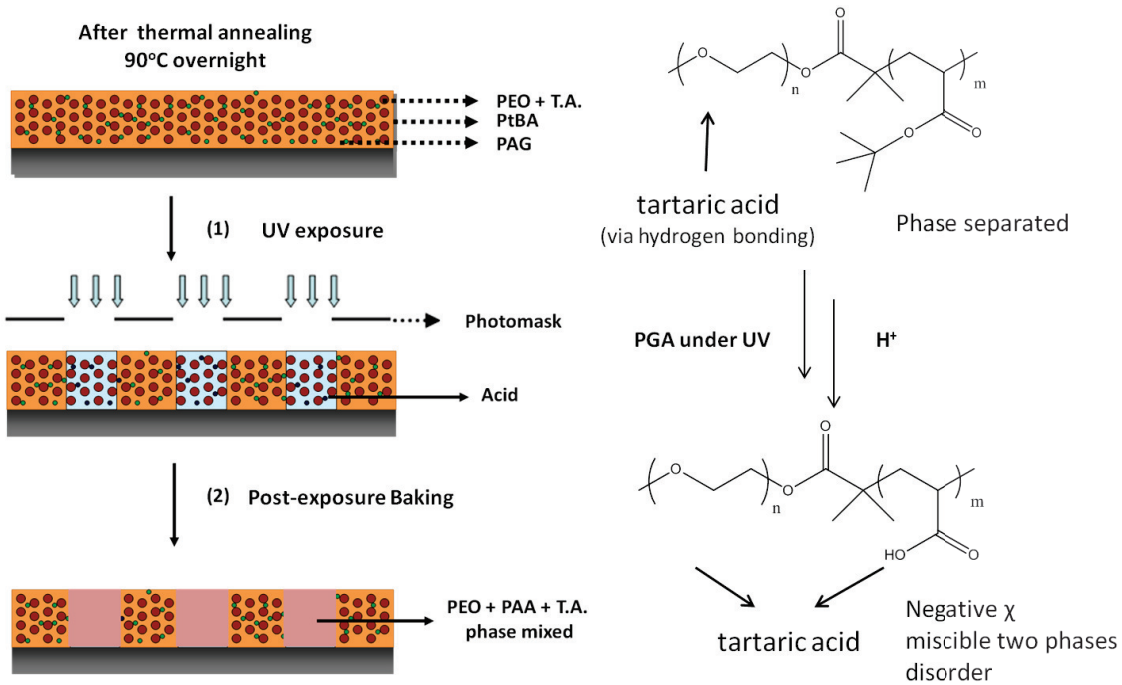

Figure 5.2 Schematic representation of the disordering transition of PEO-*b*-PtBA/tartaric acid blended system induced by UV exposure (right) and order-disorder patterns formation through UV selective exposure adding photoacid generator in this system (left).

In this chapter we describe an alternative system that enables high resolution lithography to yield patterned regions of strongly segregated and disordered domains. Instead of using the aforementioned disorder to order approach, here we use a photo-induced order to disorder scheme to achieve submicrometer scale patterns of ordered and disordered domains. The initially ordered system is comprised of a poly(ethylene oxide-block-*tert*-butyl acrylate), PEO-*b*-PtBA, blended with tartaric acid. The interaction between the tartaric acid not only inhibits the crystallization of PEO, but also effectively enhances the phase segregation strength of PEO-*b*-PtBA. The increase in segregation strength in the presence of the additive has obvious advantages including the ability to achieve order in low molecular weight systems. The PtBA block can be deprotected in the presence of a photoacid generator to form poly(acrylic acid) (PAA). PAA is compatible with both PEO and tartaric acid and thus de-protection results in a phase

mixed material. Using a mask and photo-acid generator, area selective photo-induced disorder can be realized upon UV exposure, followed by a post-exposure bake (PEB) as shown in Figure 5.2. We further show that through a kinetic study and process optimization for this process, it takes only seconds to complete the disordering transition during the PEB, which minimizes acid diffusion. Upon the addition of a trace amount of base to improve resolution, a standard approach in optical lithography, we show that submicrometer patterns of ordered and disordered regions structures can be achieved.

5.2 Experimental

5.2.1 Materials

Poly(ethylene glycol) methylether (5K, PDI=1.06 and 2K, PDI=1.08) was purchased from Polymer Source. *Tert*-butyl acrylate, anisole, copper(I) bromide(CuBr), copper(II) bromide and N,N,N',N',N''-pentamethyldiethylenetriamine (PMDETA) were purchased from Acros Organics. Triphenylsulfonium triflate (TPS-Tf) and 2-bromo-2-methylpropionyl bromide were purchased from Sigma-Aldrich.

5.2.2 Block copolymer synthesis

A magnetic stir-bar and poly(ethylene glycol) methylether were added to a flame-dried flask caped with a rubber septum, which was evacuated and purged. Distilled dichloromethane and 2-bromo-2-methylpropionyl bromide (2 molar equiv relative to the PEG polymer) were injected into the flask. Distilled triethylamine was injected drop-wise into the flask, which was then stirred at room temperature for 48 hours. The reactant was diluted with dichloromethane, extracted by water, and dried with magnesium sulfate. After precipitating into an excess amount of cold ethanol, the white powder was filtered

and dried in a vacuum oven overnight. The product was used as the macroinitiator for chain extension.

Atom transfer radical polymerization (ATRP) was used in chain extension for the synthesis of poly(ethylene oxide-*b*-*tert*-butyl acrylate) (PEO-*b*-PtBA) diblock copolymer following established procedures, with slight modifications.[93] CuBr, the macroinitiator (PEO) and a magnetic stir-bar were added into a Schlenk flask which was capped with a rubber septum and purged with N_2. Anisole and distilled *tert*-butyl acrylate, purged with N_2, were then injected into the flask. When all solids were completely dissolved, three freeze/pump/thaw cycles were applied. After PMDETA was injected into the flask, the final solution was heated at 60^{o}C for 30 hours. Tetrahydrofuran (THF) was used to dilute the reactant and a column of neutral alumina was used to filter the resulting dark green solution. The final solution was then concentrated through rotary evaporator and dried in vacuum oven at 70^{o}C for 24 hours.

5.2.3 Preparation of bulk samples for small-angle X-ray scattering and wide-angle X-ray scattering

PEO-*b*-PtBA and tartaric acid were blended at a given mass ratio in anhydrous ethanol with or without TPS-Tf of a certain weight percentage. Bulk samples were drop cast from the solution onto glass slides while baking at 60^{o}C and were annealed for 36 h at 90°C under vacuum.

5.2.4 Small-angle X-ray scattering (SAXS) and wide-angle X-ray scattering (WAXS)

Dried bulk samples were scraped off the glass slides and placed evenly in the center of metal washers, which were then sandwiched by Kapton film on both sides and

placed on a heated vertical holder. For SAXS, the samples were equilibrated at 90°C for about 20 min and interrogated at 90°C, while for WAXS, the samples were measured at room temperature. The whole system was evacuated during measurement. WAXS and SAXS in Figures 5.4, 5.5 and 5.7b were done at UMass Amherst using an in-house setup from Molecular Metrology Inc. (presently sold as Rigaku S-Max3000). A microsource (Bede) of 30 W with a 30×30 μm^2 spot size to match a Maxflux® optical system (Osmic) gave a low-divergence beam of monochromatic CuK_α radiation (wavelength λ=0.1542 nm). An image plate placed in the sample chamber about 139 mm away from the sample was used to collect WAXS data. Silver behenate was used to calibrate the sample detector distance for SAXS. SAXS measurements in Figure 5.7a and Figure 5.10b,c were done at the G1 station of the Cornell High Energy Synchrotron Source (CHESS) with wavelength of X-rays of 0.1453 nm and sample to detector distance of 913 mm using a two-dimensional charge-coupled device (CCD) camera with an image size of 1024 pixels by 1024 pixels.

5.2.5 Characterization

Polymer Characterization: Gel permeation chromatography (GPC) and 1H NMR spectra were used to characterize the synthesized polymers. GPC was performed in THF at a flow rate of 1.0 mL/min with a column bank consisted of two Polymer Labs PLGel Mixed D columns at 40°C and two detectors, a K-2301 refractive index detector and a K-2600 UV detector. A Bruker DPX300 NMR spectrometer (300 MHz) was used for acquiring 1H NMR spectra using deuterated chloroform as solvent. A Spectrum 100 FT-IR spectrometer (Perkin Elmer, Inc) was used for acquiring Fourier transform infrared

spectroscopy of PEO-*b*-PtBA films blended with 10 wt% TPS-Tf to measure the extent of PtBA deprotection during PEB and to detect hydrogen bonding between PEO and PAA.

Differential scanning calorimetry (DSC) characterization was performed using the same bulk samples prepared for SAXS on glass slides. Aluminum pans were filled with 5-10 mg samples and hermetically sealed. The DSC was performed on a TA Instruments Q100 DSC equipped with an RCS cooling system in nitrogen, with a gas flow rate of 50mL/min. All measurements were done with the heating and cooling rate of 10^{o}C/min in the temperature range of -90^{o}C to 110^{o}C. The second heating cycle from -80^{o}C to 90^{o}C was reported in this paper. All DSC data were analyzed by using Universal Analysis software from TA Instruments.

Formation of the ordered film. Films of about 100 nm thickness were spin-coated from a 3 wt% solution of PEO-*b*-PtBA and L-tartaric acid at a given mass ratio prepared in ethanol with given amount of TPS-Tf onto silicon wafers at 3000 rpm for 20s for the kinetics study. Films of about 50 nm thickness were spin-coated from a 3 wt% solution of PEO-*b*-PtBA and L-tartaric acid prepared in DMF with TPS-Tf and trace amount of triethanol amine for the area-selective UV exposure. The films were annealed for 24 h at 90^{o}C under vacuum.

Grazing incidence small angle X-ray scattering (GISAXS) using synchrotron source. All GISAXS measurements were performed at the G1 station of the Cornell High Energy Synchrotron Source (CHESS). The wavelength of X-rays used was 1.2500 Å. The incidence angle was chosen to be above the critical angle of the film under study. The sample to detector distance was 992.3 mm. The scattered radiation was collected with a

two-dimensional charge-coupled device (CCD) camera with an image size of 1024 pixels by 1024 pixels.

Atomic force microscopy (AFM) characterization. A Digital Instruments Dimension 3000 scanning microscope in tapping mode was used in AFM topographic and phase images acquisition. The ordered organic films were vacuum-pressed with a photo mask and were subject to UV flood exposure for 60 seconds using a UV lamp with a wavelength of 254 nm and intensity of 14.5 MW/cm^2 to give the dose of 870 MJ/cm^2. A post-exposure bake (PEB) was then used to achieve area-selective deprotection of PtBA and to induce the disordering transition. AFM was then used for charactering the order, disorder and order/disorder boundary. An optical microscope attached to the AFM was used to monitor the position of AFM tip on organic films. The films thickness was measured using a profilometer (Dektak3) and a Filmetrics Optical Profilometer.

5.3 Results and Discussion

5.3.1 Phase-separation of block copolymers driven by an enantiopure tartaric acid additive

Tartaric acid is a chiral acid with two stereocenters in its backbone that contains two carboxylic acid and two hydroxyl groups as shown in Figure 5.3. Enantiomerically pure D- and L- tartaric acid as well as racemic tartaric acid were investigated as additives in this study. The block copolymer was poly(ethylene oxide-*b*-*tert*-butyl acrylate) (PEO-*b*-PtBA). The initial studies were conducted using a BCP of Mn 9.2K, 46.6 wt% PtBA, PDI=1.04, which in the neat melt is weakly segregated. Both this copolymer and another copolymer of lower molecular weight (5.2K), which is disordered in the melt, were used to probe the phase behavior of the BCP/tartaric acid systems.

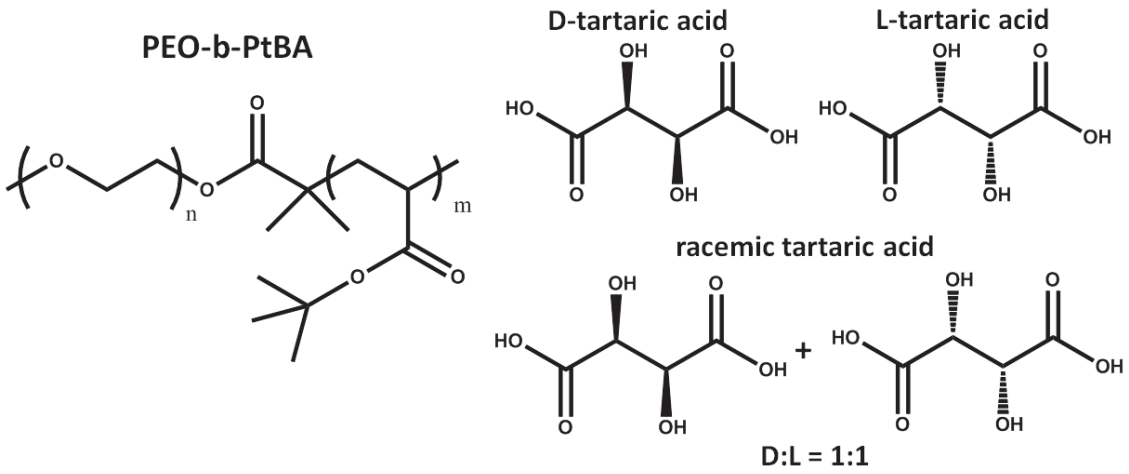

Figure 5.3 Structures of PEO-*b*-PtBA, D-tartaric acid, L-tartaric acid and racemic tartaric acid.

Upon blending enantiopure tartaric acid into the BCPs, the carboxylic acid and hydroxyl group of the tartaric acid can strongly interact with the PEO block through hydrogen bonding. The effect of the interaction of the PEO block with the additive on the crystallization behavior of PEO was investigated using wide angle X-ray scattering (WAXS) and differential scanning calorimetry (DSC). WAXS results (Figure 5.4a) show peaks at 13.2 nm^{-1} and 16.2 nm^{-1} , which correspond to (120) and (112) planes in PEO unit cell respectively, indicating the presence of PEO crystallites for neat BCP samples, while no crystal peaks were present with the addition of enantiopure tartaric acid, indicating that the strong interaction between PEO and enantiopure acid. This interaction inhibits crystallization of both PEO and tartaric acid. However, when racemic tartaric acid was added to the system, peaks indicating crystallization of both PEO and tartaric acid were observed as shown in Figure 5.4a, indicating little interaction between them. (WAXS characterizations of racemic and L-tartaric acid are shown in Figure 5.5 for reference). The DSC measurements as shown in Figure 5.4b are consistent with the

conclusions of the WAXS study. No melting endotherm for PEO is observed upon the addition of D- or L-tartaric acid, but strong melting endotherms are evident for PEO upon the addition of racemic tartaric acid. The glass transition temperature of PEO is reported to be -64°C.[184] The glass transition temperatures of the PEO tartaric acid blends are clear in the DSC analysis and range between -20 and -30°C. The glass transition of PtBA is reported to be 43°C.[185] Our DSC analysis indicates that Tgs for the low molecular weight PtBA segments in this block copolymer (9.2K, 46.6 wt% PtBA, PDI=1.04) are approximately 30°C. (See Figure 5.6)

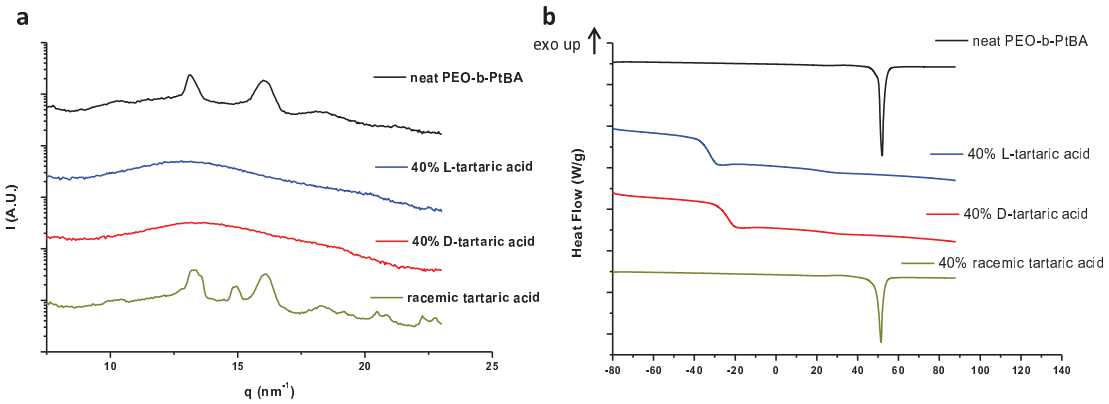

Figure 5.4 (a) WAXS characterization for neat PEO-*b*-PtBA (9.2K, 46.6 wt% PtBA, PDI=1.04), PEO-*b*-PtBA blended with 40 wt% L-tartaric acid, 40 wt% D-tartaric acid and 40 wt% racemic tartaric acid. (b) DSC characterization of neat PEO-*b*-PtBA (9.2K, 46.6 wt% PtBA, PDI=1.04), PEO-*b*-PtBA blended with 40 wt% L-tartaric acid, 40 wt% D-tartaric acid and 40 wt% racemic tartaric acid by heating from -90°C to 110°C with rate of 10°C/min.

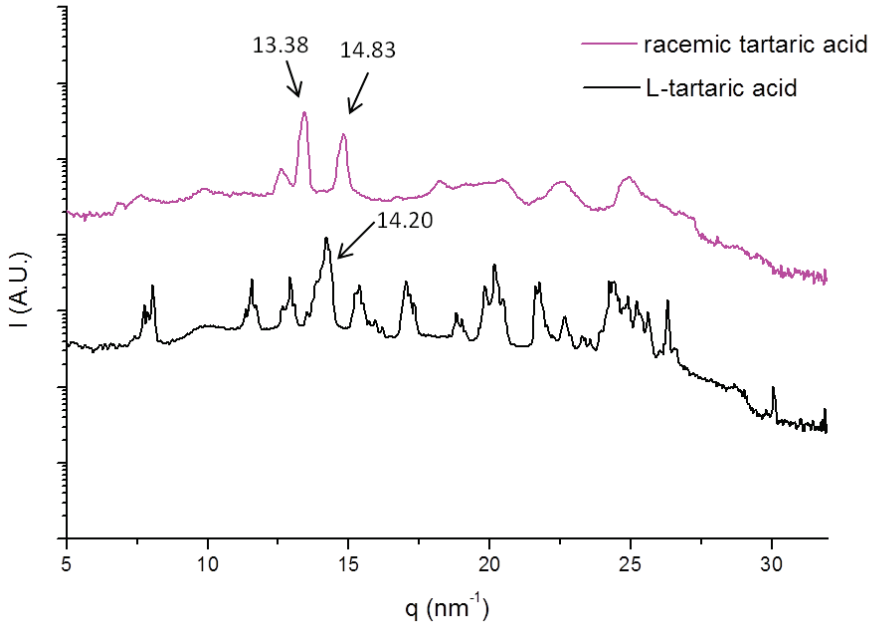

Figure 5.5 WAXS characterization for neat racemic tartaric acid and L-tartaric acid.

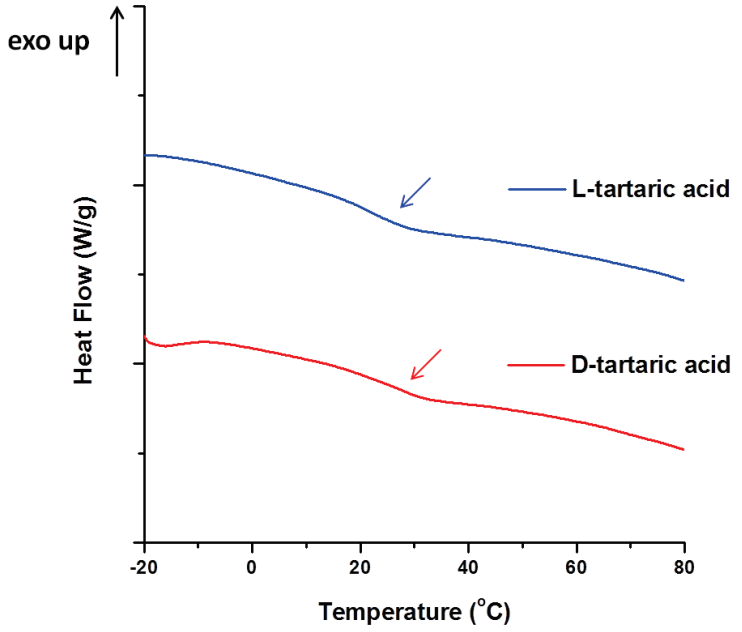

Figure 5.6 DSC characterization of PEO-*b*-PtBA (9.2K, 46.6 wt% PtBA, PDI=1.04) blended with 40 wt% L-tartaric acid and 40 wt% D-tartaric acid upon heating from -90°C to 110°C at a rate of 10°C/min showing the temperature range of -20°C to 80°C in an expanded scale to reveal the Tgs of the PtBA blocks.

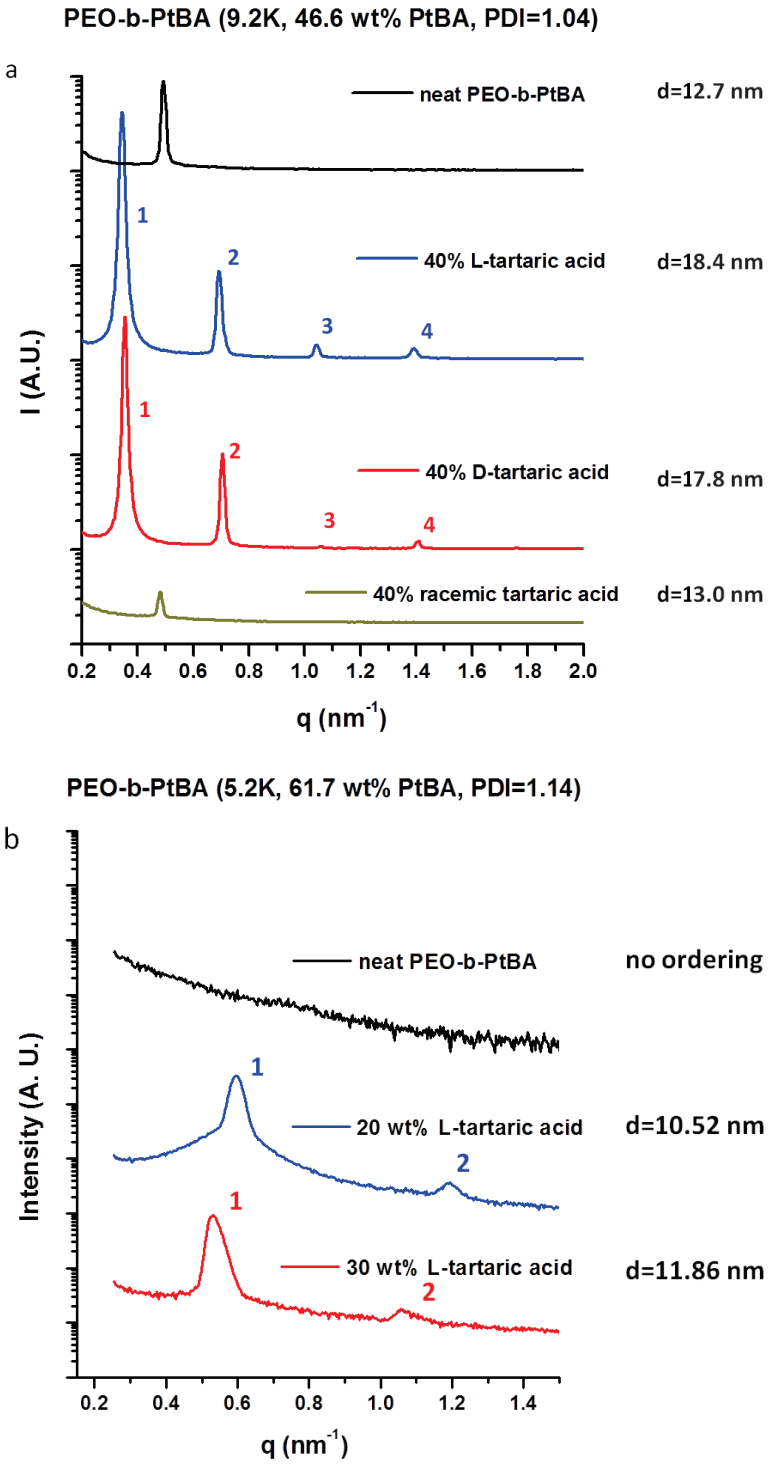

Figure 5.7 (a) SAXS of neat PEO-*b*-PtBA (9.2K, 46.6 wt% PtBA), PEO-*b*-PtBA with 40 wt% D-tartaric acid, 40 wt% L-tartaric acid, and 40 wt% racemic tartaric acid. b) SAXS spectra and integrations of PEO-*b*-PtBA (5.2K, 61.7 wt% PtBA, PDI=1.14) blended with 0 wt% L-tartaric acid, 20 wt% L-tartaric acid, 30 wt% L-tartaric acid. All samples were annealed at 90°C for 36 hours before tests and all SAXS data were taken at 90°C above the melting point of PEO.

As we reported previously,[37-38] the addition of a homopolymer that selectively associates through hydrogen bonding with one segment of low molar mass amphiphilic triblock copolymers can dramatically increase the segregation strength. Small molecule additives can be also effective for increasing segregation strength in block copolymer composites.[40, 186-190] Likewise here the enantiopure tartaric acids not only suppress the crystallization of PEO, but also substantially increase the segregation strength of PEO-*b*-PtBA. Figure 5.7 shows SAXS analysis for PEO-*b*-PtBA of two different compositions with and without the addition of tartaric acid. Figure 3a indicates that neat BCP with a molecular weight of 9.2K is weakly ordered at 90^{o}C and exhibits only a primary scattering peak. With the addition of enantiopure, either D- or L-, tartaric acid into this system, the segregation strength was increased and ordering was dramatically improved as evidenced by the significant increasing of the primary peak intensity and the appearance of multiple higher order reflections which can be assigned as lamellar morphologies. The d-spacing was also increased with the addition of enantiopure tartaric acid as shown in Figure 5.7a. In contrast, the addition of racemic tartaric acid in this system did not enhance microphase separation or order in the system. This is consistent with the DSC and WAXS analysis, which suggests that interaction between the racemates is preferred to interaction of the either of the racemates with PEO. Phase pair identity density functional theory simulations were used by the Pearl group to identify a racemic heteropair structure which has the lowest energy level for racemic tartaric acid pair.[191] Thus, there is little interaction between tartaric acid and PEO segment when equal amount of D- and L- tartaric acids are present in the system. Figure 5.7b shows SAXS results for a sample of PEO-*b*-PtBA of low molecular weight (5.2K) with and without the

addition of L-tartaric acid acquired at 90°C. While the neat copolymer is disordered the addition of 20% L-tartaric acid is sufficient to induce strong microphase separation, showing lamellar morphology based on higher order peak in SAXS (Figure 5.7b). D-spacing was increased by increasing the amount of L-tartaric acid loading, as evidenced by d-spacing of 10.5 nm with 20% L-tartaric acid while 11.9 nm with 30% L-tartaric acid calculated from SAXS (Figure 5.7b).

The DSA-induced long-range alignment of PEO-*b*-PtBA film can also be enhanced by loading enantiopure tartaric acid. Cylinders in neat PEO-*b*-PtBA film was not aligned by the patterned substrate with oxide pattern thickness of 25 nm, ling-gratings of line-width of 0.201 ± 0.018 μm and pitch length of 0.473 ±0.005 μm (Lucent Technologies, Inc.) as characterized by AFM in Figure 5.8a. After loading 12.5 wt% L-tartaric acid into PEO-*b*-PtBA, the alignment was improved as shown by AFM surface morphology in Figure 5.8b. By increasing the loading of L-tartaric acid up to 25 wt%, cylinder alignment in the composite film was achieved confirmed by AFM in Figure 5.8c. GISAXS was also used to confirm the long-range alignment in a much larger area. Same as described in Chapter 3, the anisotropic scattering patterns (Figure 5.9) from polymer/additive films indicates that the cylinders in PEO-b-PtBA/L-tartaric acid films are all aligned in a parallel manner with the underlying gratings. As shown in Figure 5.9, the scattering patterns from polymer films was only observed in q_// when the X-ray beam was co-linear with the line gratings with higher-order patterns which confirms well ordered and aligned lamellar morphology.

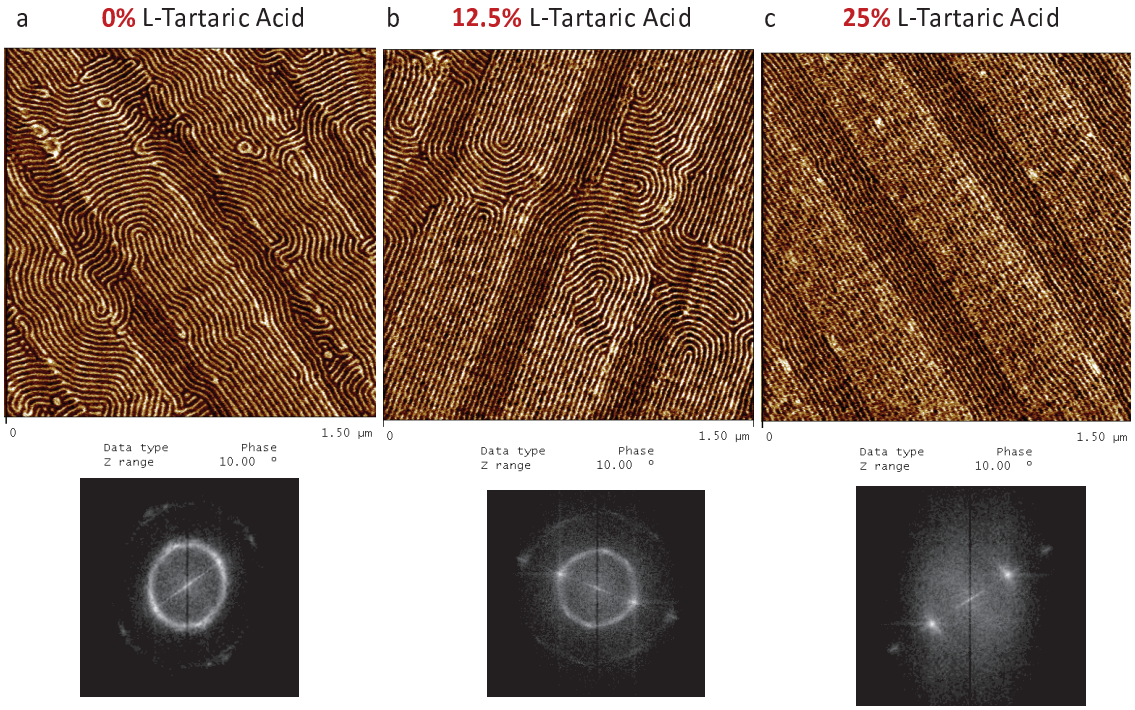

Figure 5.8 Neat PEO-*b*-PtBA (13.9K, 64 wt% PtBA, PDI=1.12) film (a), PEO-b-PtBA/12.5 wt% L-tartaric acid (b), and PEO-b-PtBA/25 wt% L-tartaric acid (c) with the thickness of ~ 45-50 nm on patterned substrate (with oxide pattern thickness of 25 nm, line-width of 0.201 ± 0.018 µm and pitch length of 0.473 ±0.005 µm from Lucent Technologies, Inc.) after thermal annealing at 90°C for 24 hrs.

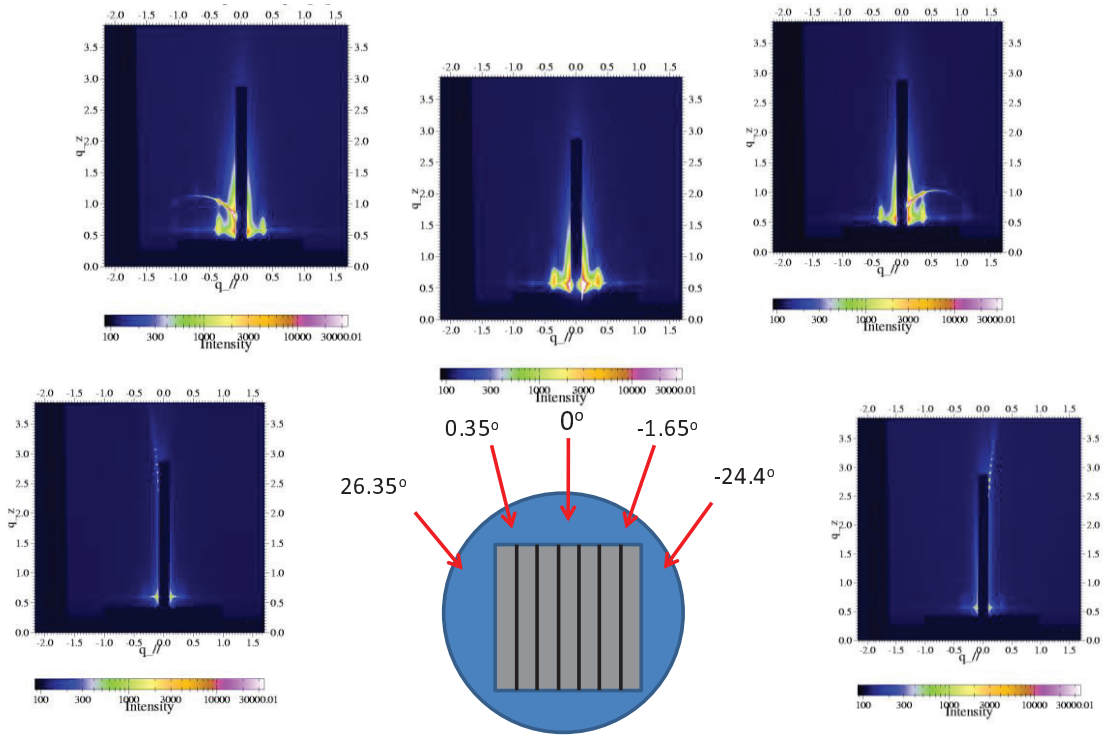

Figure 5.9 GISAXS spectra for PEO-b-PtBA/25 wt% L-tartaric acid films with aligned cylindrical pore with different relative ϕ during azimuthal rotation of the sample stage.

5.3.2 Photo-induced disorder in phase-separated PEO-*b*-PtBA/tartaric acid system

Chemically amplified deprotection of resists using photoacid generators for photolithography has been well investigated by many research groups.[192-194] Here we use catalytic deprotection of PtBA induced by the UV exposure of a photo-acid generator (PAG) followed by a quick post-exposure bake (PEB) to alter the interaction among the resist components and induce disorder. Figure 5.10 shows the scheme for the photo-acid catalyzed, chemically amplified de-protection of the PtBA block to generate PAA at elevated temperatures. PAA interacts strongly with PEO through hydrogen bonding, resulting in a negative χ. The de-protection to PAA generates two miscible blocks each of which is compatible with tartaric acid to form a completely disordered film, as shown in Figure 5.10a.

Here, triphenyl sulfonium triflate (TPS-Tf) was used as the PAG, which generates triflic acid upon UV exposure. A UV lamp with wavelength of 254 nm and intensity of 14.5 MW/cm^2 was used in this study. Exposure times were typically 60 seconds, which yields a dose of 870 MJ/cm^2 that is more than sufficient for acid generation from TPS-Tf. For PEO-*b*-PtBA (13.9K, 64 wt% PtBA, PDI=1.12) blended with 25 wt% L-tartaric acid and 5 wt% TPS-Tf, both the bulk sample and thin film show an order-disorder transition after acid catalyzed deprotection of PtBA during PEB. SAXS (Figure 5.10b) of the bulk PEO-*b*-PtBA/tartaric acid/TPS-Tf sample after thermal annealing at 90^{o}C was shown. After UV exposure for 60 sec, followed by a thermal bake at 90^{o}C overnight under vacuum, the system becomes completely disordered, as shown by SAXS (Figure 5.10c). A similar phenomenon was also observed for a 50 nm thin film, which was spin-coated from a DMF solution. Clear evidence of a well ordered film was observed in AFM images (Figure 5.10d) after thermal annealing at 90^{o}C. The microphase segregated morphology was also confirmed by GISAXS, as shown in Figure 5.10d. Disorder in the thin film was induced by UV exposure for 60 sec and 90^{o}C baking overnight under vacuum as evidenced by AFM and GISAXS analysis. (Figure 5.10e). We note here that an annealing step is necessary to allow the system to reach a well-ordered state. For polymers with low molecular weight, the annealing step requires a shorter time. As shown in Figure 5.11, for lower molecular weight PEO-*b*-PtBA (5.2K, 61.7 wt% PtBA, PDI=1.14), 25 minutes at 100^{o}C was sufficient to achieve a well ordered film. The higher molecular weight sample required several hours.

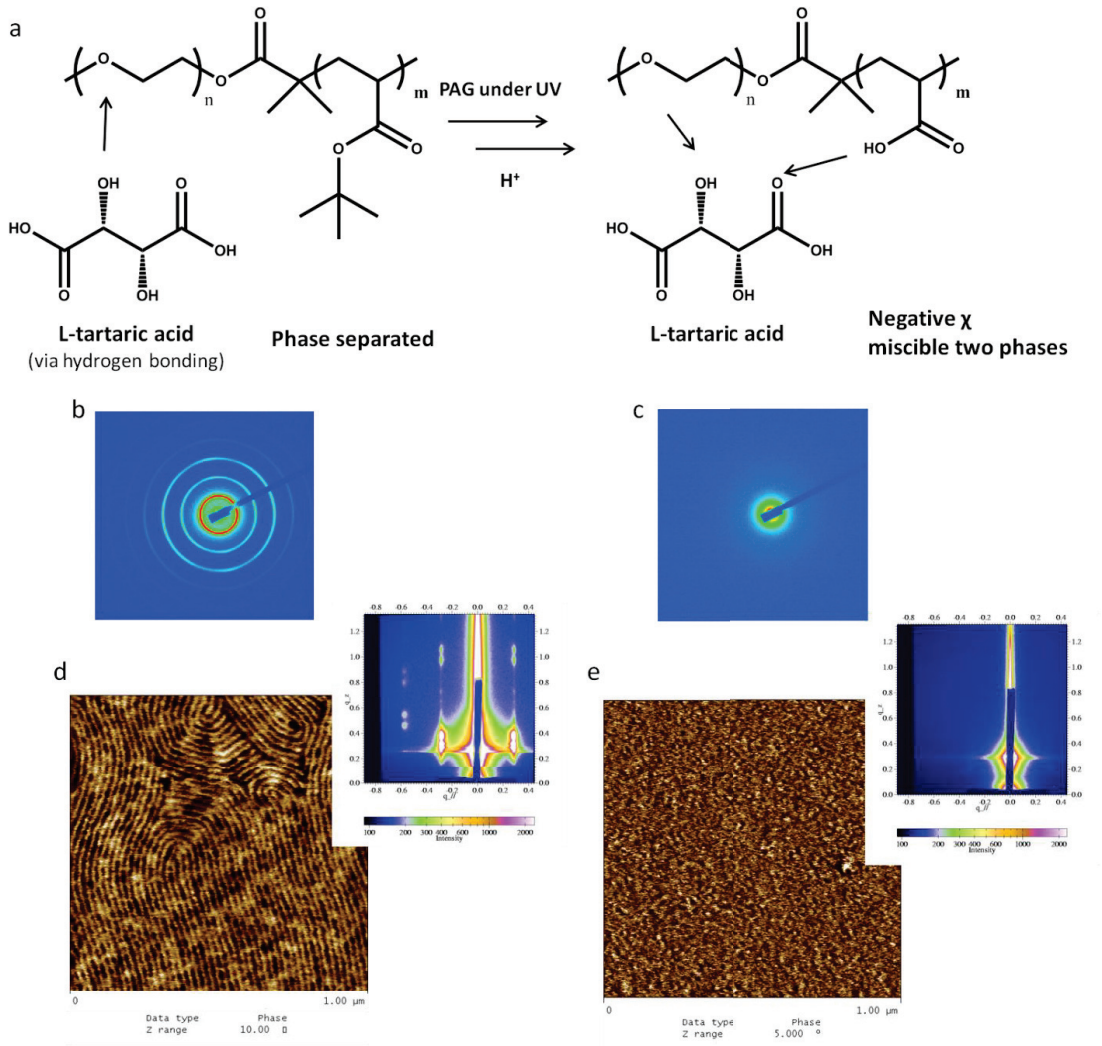

Figure 5.10 (a) Schematic showing deprotection of PEO-*b*-PtBA (13.9K, 64 wt% PtBA, PDI=1.12) into PEO-*b*-PAA catalyzed by acid generated from TPS-Tf upon UV flood exposure. (b) SAXS characterization of a bulk sample of PEO-*b*-PtBA blended with 25 wt% L-tartaric acid and 5 wt% TPS-Tf after annealing at 90°C for 36 hours. (c) SAXS characterization of a bulk sample (b) after UV (254 nm) exposure for 60 seconds and annealing at 90°C overnight. (d) AFM characterization and GISAXS spectra of PEO-*b*-PtBA films blended with 25 wt% L-tartaric acid and 5 wt% of TPS-Tf, with a thickness of ~50 nm after thermal annealing at 90°C overnight. (e) AFM characterization and GISAXS spectrum of the ordered film in (d) after UV (254 nm) exposure for 60 seconds and annealing at 90°C overnight.

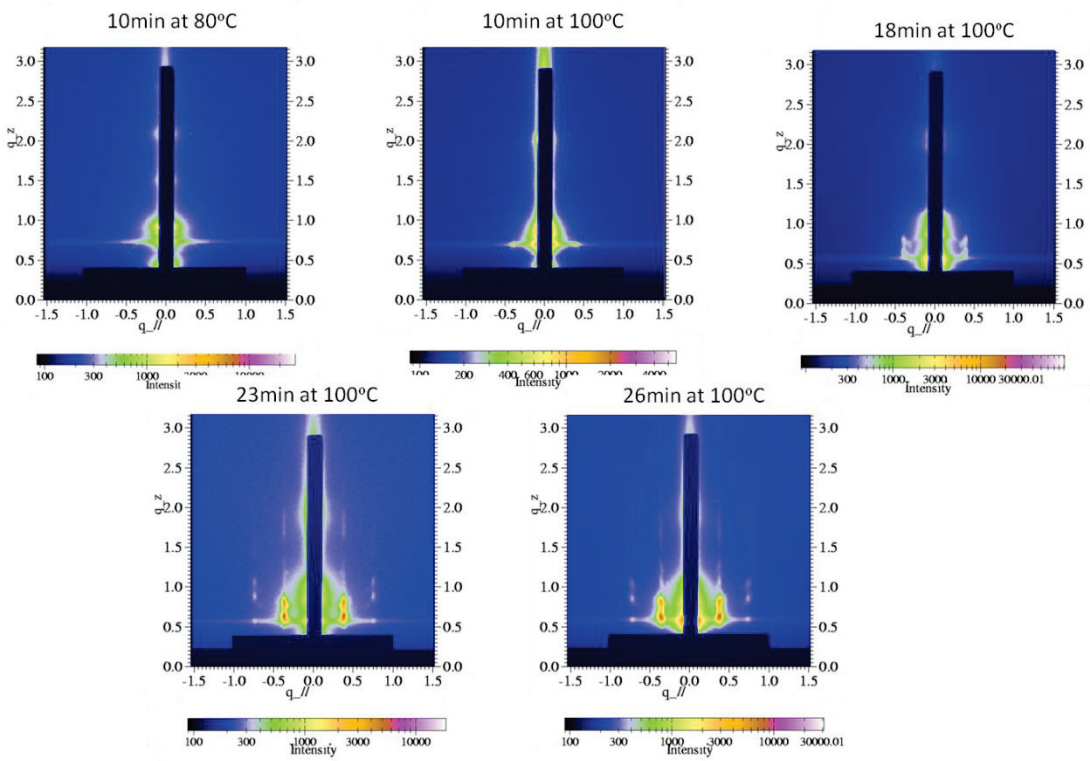

Figure 5.11 Evolution of phase segregation in a thin film of PEO-*b*-PtBA(5.2K, 61.7 wt% PtBA, PDI=1.14) with 30% L-tartaric acid during annealing at 100°C as characterized by GISAXS.

In order to achieve sharp order/disorder sub-micron patterns, acid diffusion needs to be minimized during PEB. Image blur during PEB in a patterned, chemically amplified photoresist has been attributed to reaction-diffusion kinetics during PEB.[195-196] Minimizing the time used for the PEB favors high resolution patterning. We used a kinetics study for the disordering transition to optimize the process. Specifically, GISAXS was used to track the disordering transition during the PEB. Three different TPS-Tf loadings in the PEO-*b*-PtBA (18K, 72.3 wt% PtBA, PDI=1.12)/L-tartaric acid (22 wt%) blend system were characterized in this study: 3 wt%, 7.5 wt% and 10 wt%. Figure 5.12 shows that after UV exposure, a 40 - 60 min PEB was required at 110°C to disorder the system with the addition of 3 wt% TPS-Tf. The same system required ~15

sec with 7.5 wt% TPS-Tf, and only ~6 sec with 10 wt% TPS-Tf. Thus, 10 wt% TPS-Tf blends were selected to study the temperature dependence of the disorder transition during PEB. Three different PEB temperatures were used: 110°C, 100°C, and 90°C. As shown in Figure 5.13, the disordering transition was complete during PEB after 6 sec at 110°C as compared to 15 sec and 22 sec at 100°C and 90°C, respectively. Fourier transform infrared spectroscopy (FT-IR) was used to characterize the extent of deprotection of PtBA to yield PAA. Figure 5.14 shows the complete deprotection of PtBA using 10 wt% TPS-Tf after UV flood exposure for 60 seconds and PEB at 110°C for 5 seconds and 10 seconds. FT-IR analysis also indicates hydrogen bond formation between PAA and PEO as shown in the figure.

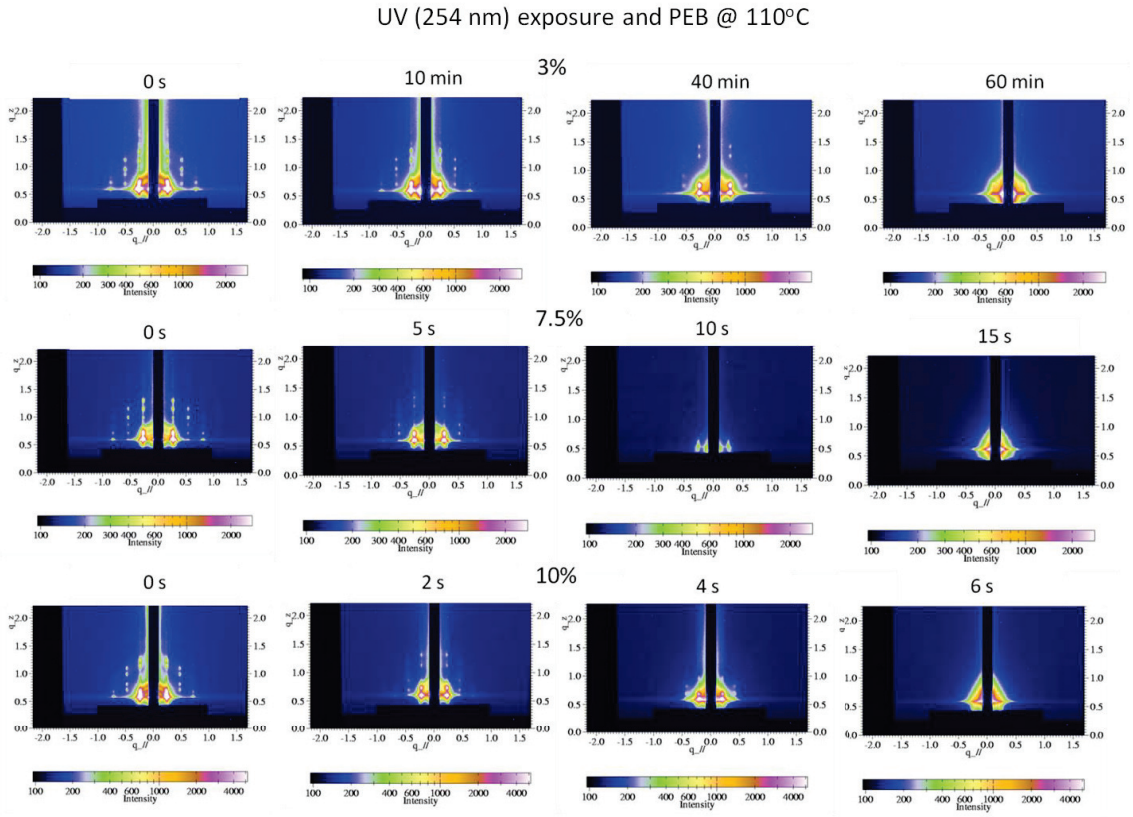

Figure 5.12 Kinetic study of the order-disorder transition during PEB at 110°C using GISAXS after UV (254 nm) exposure for 60 seconds. Three different amounts of TPS-Tf added to PEO-*b*-PtBA (18K, 72.3 wt% PtBA, PDI=1.12) blended with 22 wt% L-Tartaric acid: 3 wt%, 7.5 wt% and 10 wt%.

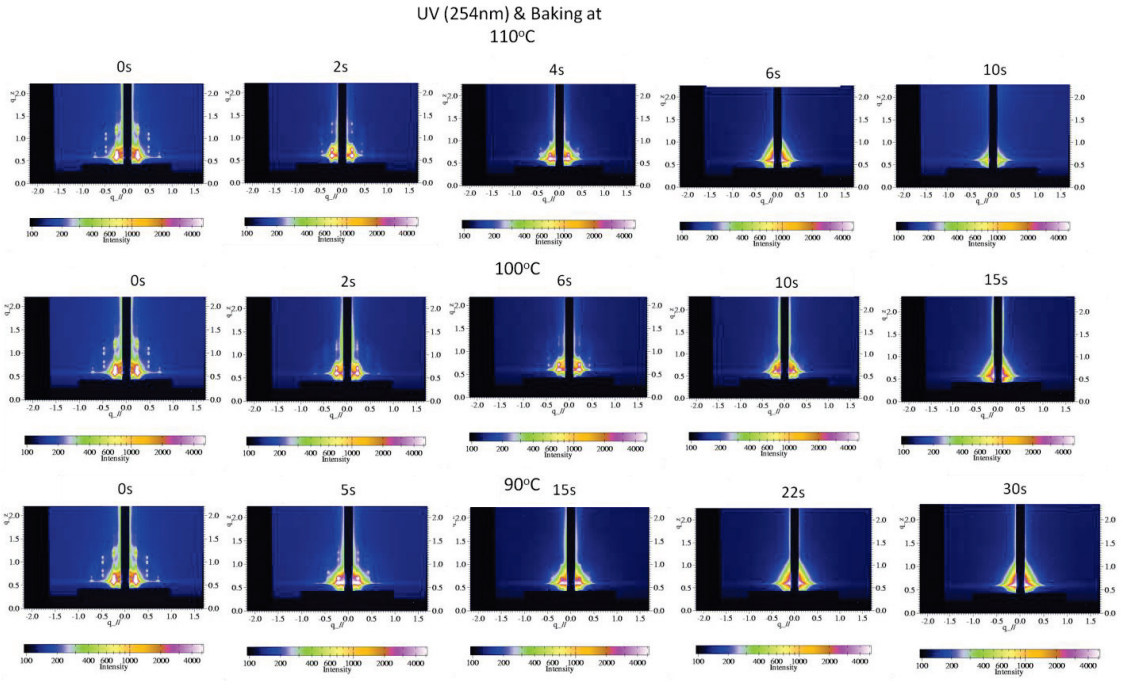

Figure 5.13 Kinetic study of the disordering transition during PEB using GISAXS after sufficient UV (254 nm) exposure. Three different temperature were used during PEB for PEO-*b*-PtBA (18K, 72.3 wt % PtBA, PDI=1.12) blended with 22 wt% Tartaric acid and 10 wt% TPS-Tf: 110°C, 100°C and 90°C.

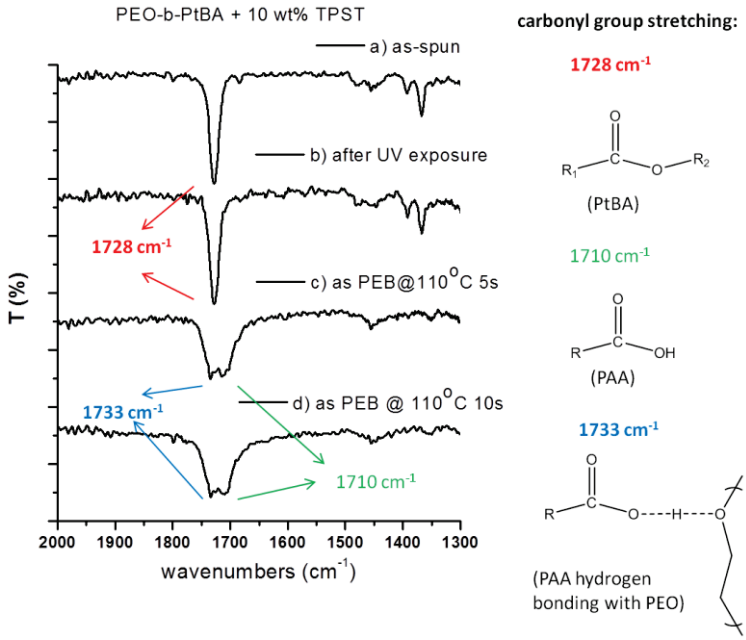

Figure 5.14 FT-IR spectra showing the extent of deprotection of *tert*-butyl acrylate in PEO-*b*-PtBA (18K, 72.3 wt% PtBA, PDI=1.12) films blended with 10 wt% TPS-Tf. FT-IR spectra for (a) as-spun PEO-*b*-PtBA + 10 wt% TPS-Tf film, (b) film after UV flood exposure for 1 min, (c) film after UV flood exposure and PEB at 110°C for 5 seconds, (d) film after UV flood exposure and PEB at 110°C for 10 seconds.

We next investigated area selective patterning *via* illumination through a mask. To improve pattern resolution, a base quencher can be employed.[197-198] 0.5 wt% triethanol amine was loaded into this system to neutralize the trace amounts of acid that may diffuse into the unexposed area. Using DMF as the solvent, PEO-*b*-PtBA (18K, 72.3 wt% PtBA, PDI=1.12), 22 wt% L-tartaric acid, and 10 wt% TPS-Tf was spin-coated onto a clean silicon wafer to form a 50 nm thick film. After thermal annealing at 90°C overnight, nicely ordered structures were generated, as characterized by AFM (Figure 5.15a). GISAXS was used to confirm the ordering (Figure 5.15b) and showed a lamellar morphology through the integration in the q_// direction (Figure 5.15c).

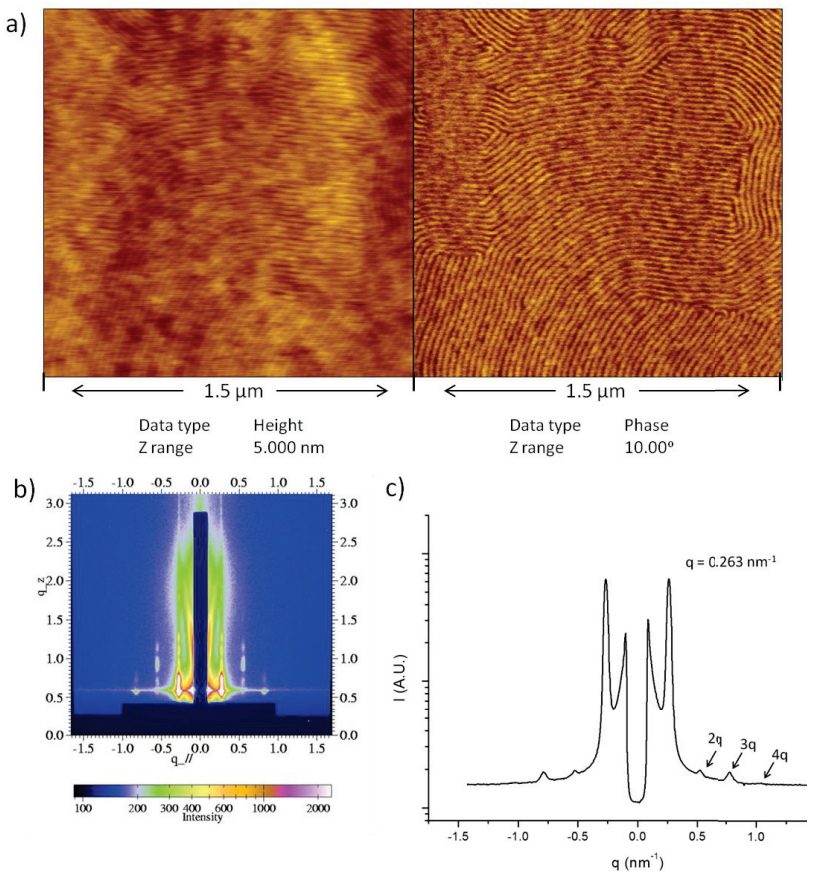

Figure 5.15 AFM characterization (a) of PEO-*b*-PtBA (18K, 72.3 wt% PtBA, PDI=1.12) film blended with 22 wt% L-tartaric acid, 10 wt% TPS-Tf and 0.5 wt% triethanol amine after thermal annealing at 90°C overnight. GISAXS spectrum (b) and integration (c) for the ordered film in (a).

A photomask was then applied by vacuum to make good contact with the ordered film. After UV exposure for 60 sec and a PEB at 110^{o}C for 10 sec, the area exposed to UV became completely disordered, while the area blocked by the mask still kept the ordered structure, as shown by AFM characterization in Figure 5.16b, d. GISAXS was again used to confirm the structures through the area-selective UV exposure and a PEB. An ordered PEO-*b*-PtBA/L-tartaric acid film with 10 wt% TPS-Tf became completely disordered after a 60 sec UV exposure and a 10 sec PEB at 110^{o}C, as observed in the GISAXS spectrum (Figure 5.16c). The ordered film maintained the ordering after a 10 sec baking at 110^{o}C without UV exposure, as shown by GISAXS measurement (Figure 5.16e), which rules out the possibility that polymer decomposition during baking causes the disordering. Finally, we used AFM to characterize the order-disorder edge to show the sharp submicron patterns of ordered and disordered regions. Figure 5.17 shows that a very clear pattern of the regions can be observed in a 1.5 micron by 1.5 micron AFM phase image (Figure 5.17a), and also on in a 3 micron by 3 micron AFM phase image (Figure 5.17c), with the optical microscopy image showing the scanning tip on the order-disorder boundary (Figure 5.17b). (Height images are shown in Figure 5.18.) The images suggest weak orientation of the lamellar structures near the edge of the patterns. While we did not investigate this observation further, domain orientation can often be induced by external or non-uniform fields, in this case a chemical potential gradient. There are also indications of spherical domains near the line edge in Figure 5.17. Spherical domains could emerge as a result of volume reduction of the PtBA-rich domain upon partial deprotection of PtBA, leading to an order-order transition. In any case, these images confirm that the combination of short PEB time, relatively high TPS-Tf loadings, and the

addition of trace-amount of amine inhibit acid diffusion and to achieve sharp order-disorder patterns on a submicron scale even when using a contact mask.

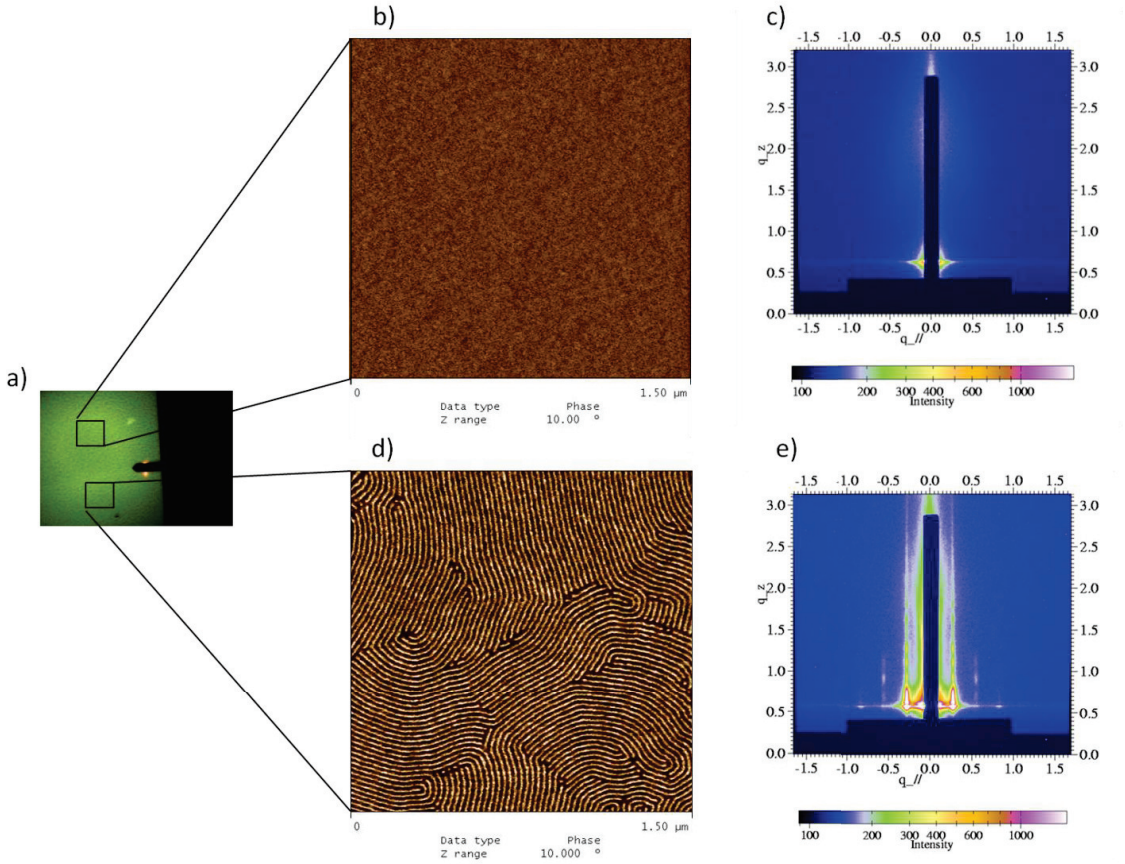

Figure 5.16 (a) Optical micrograph of the film from Figure 6 after area-selective UV (254 nm) exposure for 60 sec using a photomask and a PEB at 110°C for 10 sec showing two regions with a boundary. (b) The UV-exposed region at the top showed disordered structure, as characterized by AFM. (c) The GISAXS spectrum for the film from Figure 6 after UV (254 nm) flood exposure for 60 sec and PEB at 110°C for 10 sec. (d) The unexposed region kept its ordered structure, as characterized by AFM. (e) GISAXS spectrum for the film from Figure 5.15 after baking at 110°C for 10 sec without UV exposure.

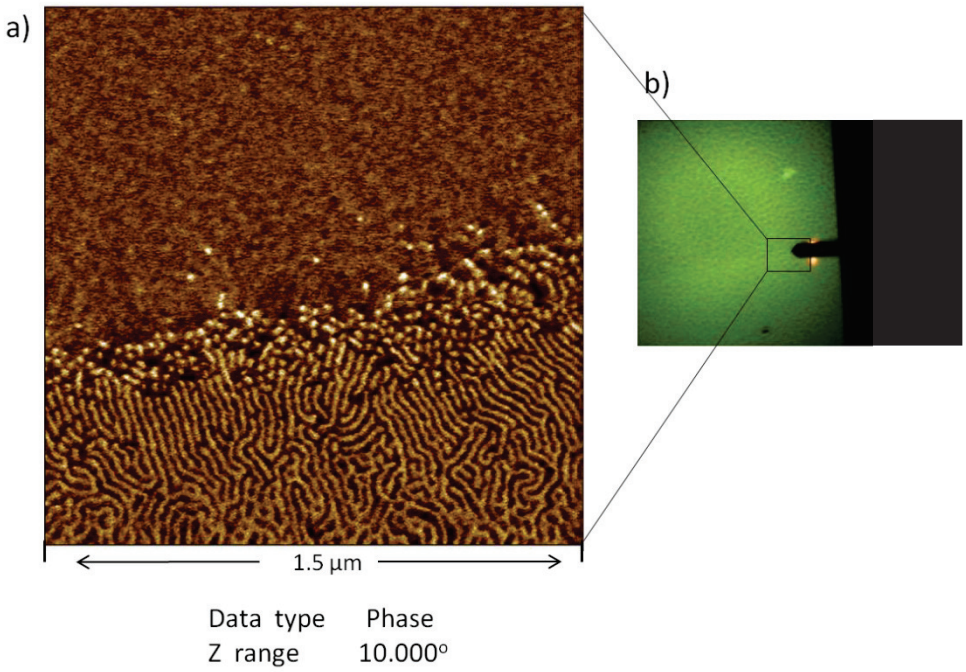

Figure 5.17 AFM characterization of the film from Figure 7 at the sharp edge of order-disorder pattern. (a) Phase image at the scale of 1.5 µm × 1.5 µm. (b) The optical microscope attached to the AFM instrument showed the sharp edge of order-disorder pattern during AFM scanning. (c) Phase image at the scale of 3 µm × 3 µm.

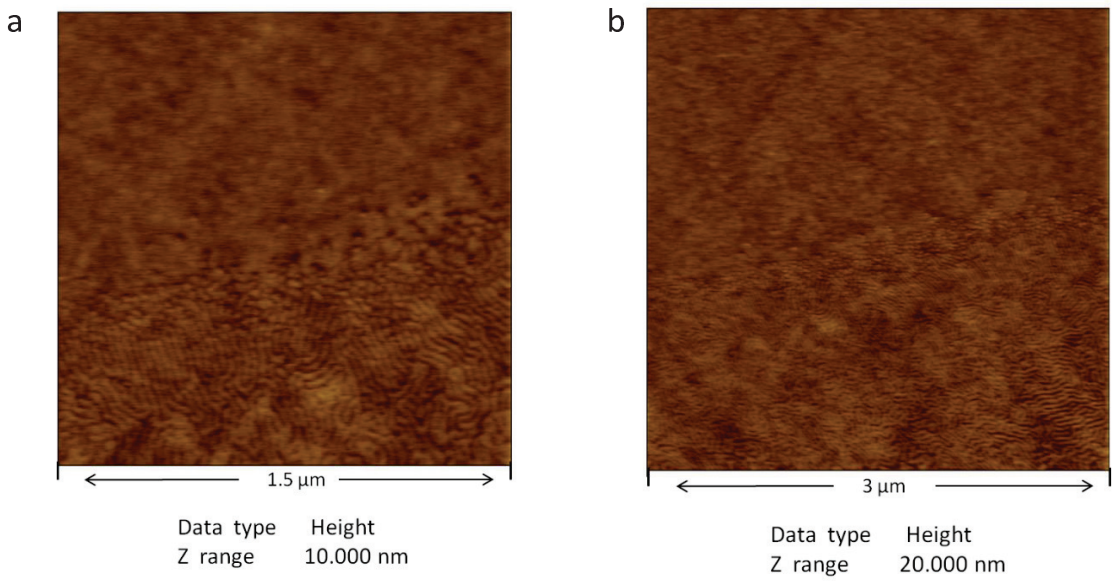

Figure 5.18 AFM characterization of the film from Figure 5.16 at the sharp edge of order-disorder pattern. Height image (a) at the scale of 1.5 µm × 1.5 µm. Height image (b) at the scale of 3 µm × 3 µm.

5.4 Conclusion

We demonstrate a method to achieve submicrometer patterns of well-ordered, microphase separated and fully disordered regions *via* photo-induced disorder in a block copolymer/additive film. In our example, chemically amplified deprotection of the tBA block in PEO-*b*-PtBA blended with tartaric acid to yield a PAA block induces compatibility of the components, resulting in phase mixing. In this system, the tartaric acid additive plays two important roles. First, it increases segregation strength in PEO-*b*-PtBA, enabling well-ordered systems at low BCP molecular weights. Low molecular weights in turn provide access to small domains spacings and relatively rapid order and disorder kinetics. Second, the presence of tartaric acid suppresses PEO crystallization, resulting in smooth films and eliminating the influence of PEO crystallization on the BCP morphology. The observation that both D and L tartaric acid enantiomers are effective

additives for these purposes alone, but not in combination where the interaction among the complementary enantiomers is strong relative to the interactions with the polymer segments, illustrates the importance of the additive-chain interactions in driving phase segregation strength.

We point out that the additive strategy in these systems has additional advantages not explored here. For example, one could choose an additive that exhibits strong etch resistance. Using the system design described here, the additive would be confined to the PEO-rich domains in the ordered BCP leaving the PtBA domains unmodified. By comparison the additive is uniformly distributed in the disordered phase. This may in turn enable selective etching of the PtBA domains in the ordered regions relative to both the PEO rich domains in the ordered regions and the phase mixed disordered regions, which also contain the additive. Because there are few constraints on additive selection beyond strong interaction with PEO and PAA generated upon deprotection of the PtBA block many other designs for the additive for a myriad of applications are possible.

CHAPTER 6

FORMATION OF HELICAL (H*) PHASE IN ACHIRAL BLOCK COPOLYMER INDUCED BY SMALL CHIRAL ADDITIVES

6.1 Introduction

Ordered nanostructures can be achieved using self-assembly of different molecular units, like nanoparticles,[199-204] nanowires,[205-210] nanorods,[211-214] nanotubes,[215-222] colloids,[223-225] block copolymers,[1-8, 226-227] *etc*. through non-covalent interactions. Among those molecular units, block copolymer has been studied thoroughly in recent years for its easily tunable geometry, including its size and shape. Especially, three dimensional (3-D) structures can be easily achieved through block copolymer self-assembly.[51, 158-160] Typically, based on the phase-diagram[9] of a diblock copolymer system, spherical, cylindrical, lamellar and gyroid morphologies are accessible through manipulating important parameters, like the number of repeat units (N), segregation strength (χ), block volume fraction (f), and even polydispersity index (PDI).[228-229] However, some biological inspired morphologies, for example helical superstructure, can not easily be generated from regular achiral block copolymer system.

Helical superstructure is an important structure which provides 3-D geometry for a variety of applications, especially metamaterials.[230-231] People have demonstrated the formation of helical structures in different length scales[232] in synthetic supramolecules, like chiral molecules,[233-236] helical chain conformations,[237-242] helical aggregations in solution,[243-247] *etc.* However, it is challenging to achieve highly 3-D packed nanohelices in bulk system. Previously, the Ho group[42-43] was using a chiral diblock copolymer

system, poly(styrene)-*b*-poly(L-lactide) (PS-*b*-PLLA), to achieve nanohelical superstructures as shown in Figure 6.1a. In this method, the chiral entity of PLLA block is a very important driving force for the final superstructures. The requirement for this chirality in the block copolymer backbone complicates the BCP synthesis and limits the versatility of functional blocks. The Jinnai group was using an achiral triblock terpolymer, polystyrene-*b*-polybutadiene-*b*-poly(methyl methacrylate) (SBM),[44] to achieve the helical morphology in bulk as shown in Figure 6.1b. However, the order and interactions of each selected block are very specific and the molecular weight range of each block is very narrow in this method. Moreover, there is no control over left or right- handed helices in this achiral triblock terpolymer system. Thus, the real applications are greatly limited by the complicated processes involved, making those methods only useful for scientific interests without any large-scale manufacturing possibility.

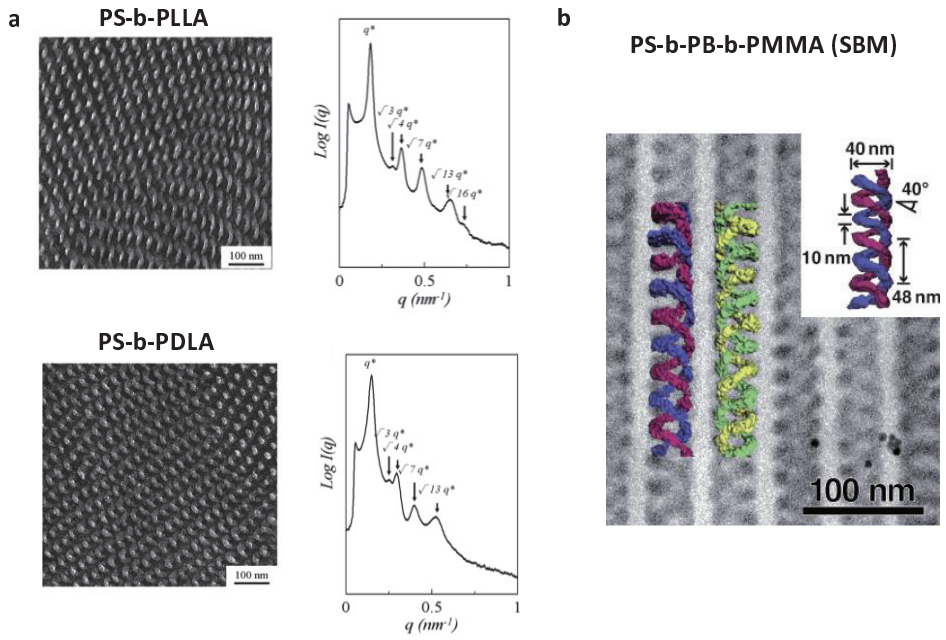

Figure 6.1 (a) Helical superstructures generated from chiral diblock copolymer PS-*b*-PLLA and PS-*b*-PDLA, adapted from Ref; [64] (b) Double helical structures formed in achiral terpolymer PS-*b*-PB-*b*-PMMA, adapted from Ref.[44]

In this chapter, we describe an alternative method, called additive driven self-assembly to achieve the nanohelical phase in an achiral block copolymer system. Additive driven self-assembly has been investigated in our group and also Chapter 5 as a method to enhance block copolymer phase separation. This method is based on the selective interaction between one segment of the block copolymer and the additives, like homopolymers,[37, 248] small functional molecules,[39-40] and nanoparticles[249-250] to increase the segregation strength of the system and generate ordered nanostructures for a variety of applications. In this chapter tartaric acid with two chiral centers is selected as the chiral additive to a PEO-based achiral diblock copolymer system, poly(ethylene oxide)-*b*-poly(tert-butyl acrylate) (PEO-*b*-PtBA).[251] The chiral information from the additive can be easily transferred into the achiral block copolymer backbone and at the same time increase the segregation strength of the system. The chirality can then be transferred into the phase of the supramolecule from the composite backbone to form nicely ordered 3D packed nanohelical superstructures as shown in Figure 6.2.

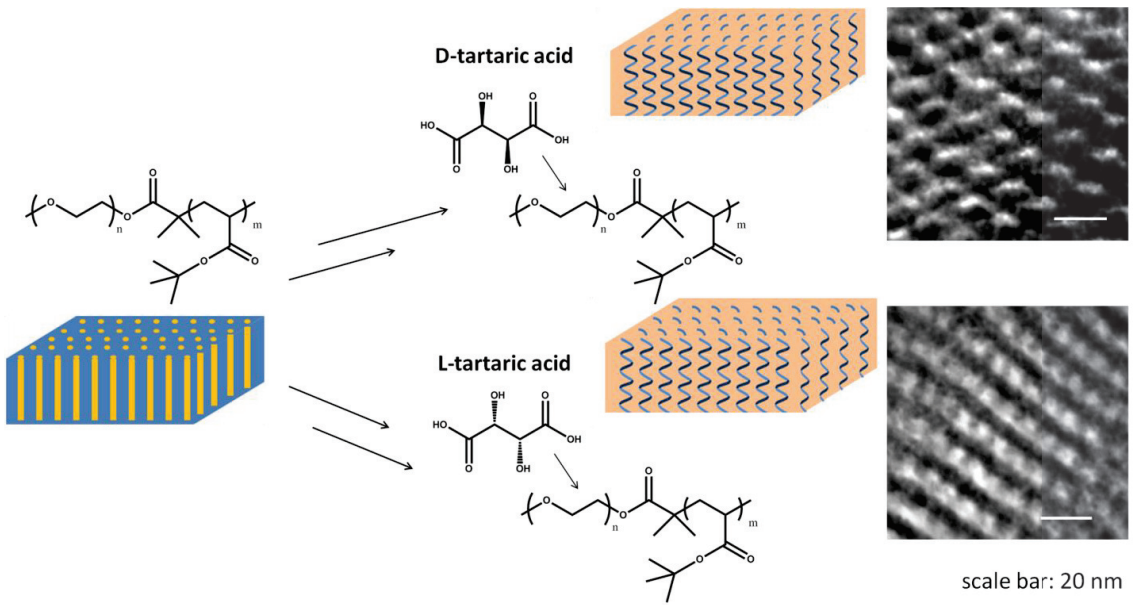

Figure 6.2 Formation of helical (H*) phase in achiral block copolymer, PEO-*b*-PtBA, induced by small chiral additives, tartaric acid.

6.2 Experimental

6.2.1 Materials

2-bromo-2-methylpropionyl bromide was bought from Sigma-Aldrich. *Tert*-butyl acrylate, copper(I) bromide(CuBr), copper(II) bromide, anisole and N,N,N',N',N''-pentamethyldiethylenetriamine (PMDETA) were bought from Acros Organics. Poly(ethylene glycol) methylether (5K, PDI=1.06 and 2K, PDI=1.08) was bought from Polymer Source. Ruthenium tetroxide, 0.5% stabilized aqueous solution was bought from Electron Microscopy Sciences.

6.2.2 Block copolymer synthesis

PEO end-group functionalization and PEO-*b*-PtBA block copolymer synthesis were performed following the same procedure as we used in previous work.[251] Atom transfer radical polymerization (ATRP) was used for the PEO-*b*-PtBA synthesis based on the established procedure.[93]

6.2.3 Polymer characterization

The synthesized block copolymers were characterized by Gel permeation chromatography (GPC) and 1H NMR spectroscopy. The detailed conditions for GPC and 1H NMR were the same as our previous work. [251]

Small-angle X-ray scattering (SAXS). PEO-*b*-PtBA was blended with tartaric acid at a given mass ratio in DMF or anhydrous ethanol and then drop-cast on glass slides dried at room temperature for DMF and baked at 60^{o}C for ethanol. Thermal annealing at 90^{o}C under vacuum for 36 hrs was then applied to those samples. After scraped from the glass slides, those dried bulk samples were then placed in the center of metal washers, sandwiched by Kapton film and placed on a vertical holder with a temperature controller.

The whole system of SAXS was under vacuum during measurement and the samples were equilibrated at 90°C for 20 min before measurement. The detailed condition for SAXS was the same as our previous work. [251]

Transmission electron microscopy (TEM). A JOEL 2000FX electron microscope was used for TEM measurement which operated at an accelerating voltage of 200 kV. A Leica Ultracut microtome was used to directly cut the bulk sample using a diamond knife conducted at a low temperature environment of -120°C and with the diamond knife at temperature of -110°C. The thin pieces of the samples were then detached from the diamond knife and transferred to copper grids with carbon films. The copper grids with the sample pieces were then stained with ruthenium tetroxide (0.5% stabilized aqueous solution) for about 10 min before TEM measurement.

6.3 Results and Discussion

Previously our group investigated how enantiopure tartaric acid effectively improves the ordering through the hydrogen bonding between the acid and the PEO block of the weakly segregated system, PEO-*b*-PtBA.[251] We determined that the hydrogen bonding between carboxylic acid of tartaric acid and the PEO block completely inhibits PEO crystallization and dramatically enhances the segregation strength of the system. This additive driven self-assembly can even induce order from a completely disordered system.[251] In this study PEO-*b*-PtBA with a molecular weight of 18K, PtBA weight percentage of 72.3% and a PDI of 1.12 was used for this chirality translation study, which was synthesized by end-group functionalization of PEO followed by atom transfer radical polymerization (ATRP). Bulk PEO-*b*-PtBA/D-tartaric acid composite samples were prepared through drop-casting on a glass slide from DMF solution (2.6 wt% of polymer)

at 60°C. After thermal annealing inside of a vacuum oven under 90°C for 36h, small angle X-ray scattering (SAXS) was used to characterize the self-assembled nanostructures in the bulk composite system with a variety of D-tartaric acid loading amounts. Figure 6.3a shows that very strong ordering was exhibited after thermal annealing upon blending 22 wt% D-tartaric acid (to polymer) into the system. The integration curve of the SAXS patterns in Figure 1b shows a very sharp first order peak followed by multiple high order peaks. The q value ratios of those scattering peaks are 1, √4, √7, √9, √13, √16, which is consistent with a cylindrical morphology. In order to more clearly characterize the nanostructure of the bulk sample, Transmission Electron Microscopy (TEM) was used to image the structure inside of the PEO-*b*-PtBA/tartaric acid composite. A cryo-microtoming process was required to cut the samples into thin pieces with the thickness of around 50 nm for TEM characterization. This process was conducted at a low temperature environment (-120°C), which is far below the glass transition temperature of PEO block, using a diamond knife with the temperature around -110°C. After detaching those thin pieces of the sample from the diamond knife on copper grids, ruthenium tetroxide (RuO_4) was used to stain the PEO domain to increase the contract of the two domains under TEM. As shown in Figure 6.3c, very nicely highly packed nanohelices with a right handed helical sense were clearly observed, with the pitch size of ~25 nm, which is consistent with the d-spacing observed in SAXS, using TEM. The chirality was successfully transferred from D-tartaric acid into the phase of the block copolymer/additive composite system. Previously, the Inai group[240, 242] has studied that chiral information can be transferred from chiral additive into achiral compound through the Domino effect to achieve helical conformation in peptide chain based on the

noncovalent interactions between the N-terminal amino groups in peptide backbone and the chiral carboxylic acids. Here, through the same Domino effect using hydrogen bonding interaction, the chiral information of D-tartaric acid can not only be successfully transferred into the achiral block copolymer PEO-*b*-PtBA backbone but also transferred into the phase of the block copolymer composite to form helical superstructure.

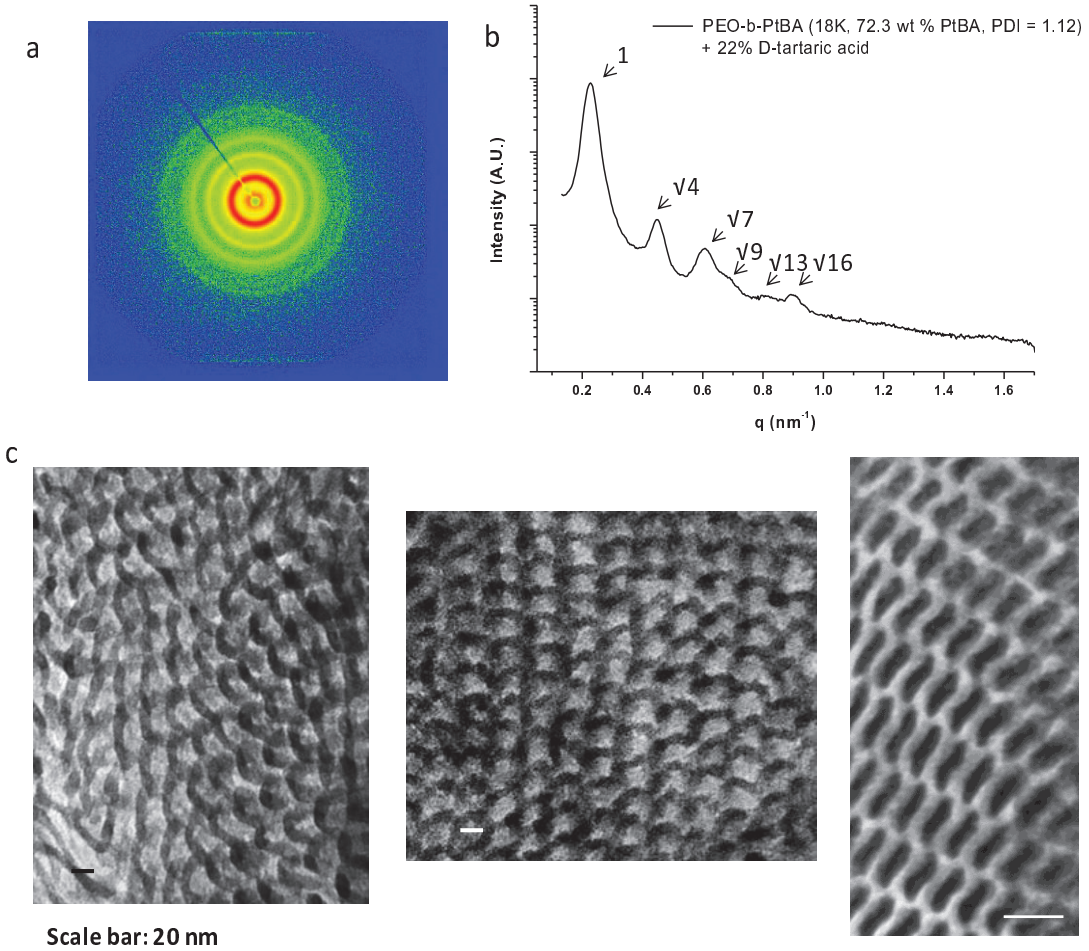

Figure 6.3 SAXS spectrum (a) and integration (b) of neat PEO-*b*-PtBA (18K, 72.3 wt% PtBA, PDI=1.12) blended with 22 wt% D-tartaric acid drop-cast from DMF. (b) TEM characterization of PEO-*b*-PtBA (18K, 72.3 wt% PtBA, PDI=1.12) blended with 22 wt% L-tartaric acid after cryo-microtoming and RuO_4 staining. All samples were annealed at 90°C for 36 hours before tests and all SAXS data were taken at 90°C above the melting point of PEO.

L-tartaric acid, as the opposite enantio-isomer of D-tartaric acid, was also investigated in this study. As shown in Figure 6.4a, SAXS for PEO-*b*-PtBA(18K, 72.3 wt% PtBA, PDI=1.12) blended with 22 wt% L-tartaric acid gives the same set of scattering peaks as the one with D-tartaric acid, with very similar d-spacing of around 27 nm. A control sample, neat PEO-*b*-PtBA (18K, 72.3 wt% PtBA, PDI=1.12) was also investigated using SAXS. The scattering peaks in Figure 6.4a for neat PEO-*b*-PtBA show ordering in the system with cylindrical morphology, but the non-obvious high order peaks indicate no long-range order. Furthermore, the d-spacing of neat PEO-*b*-PtBA sample is only 18.3 nm which is much smaller than those loaded with 22 wt% enantiopure tartaric acid, either L- or D-, indicating tartaric acid entering the matrix of the system to expand the geometry.

Again, TEM was used to image the structures of those samples after cryo-microtoming and RuO_4 Staining. Cylindrical morphology was clearly observed in the neat PEO-*b*-PtBA sample in TEM. Figure 6.4b shows the TEM image when the projection is perpendicular to the cylinder axis, while Figure 6.4c shows the TEM image when the projection is parallel to the cylinder axis. It is clear that the PEO (the dark region) is the minor domain as shown in the parallel projection. With the addition of L-tartaric acid in PEO-*b*-PtBA, the helical superstructure was again observed as shown in Figure 6.4d. It is very clear that the helix in the sample loaded with L-tartaric acid is in a left-handed sense compared with the right-handed helix in the sample loaded with D-tartaric acid as shown in Figure 6.4c, 6.4f, and also confirmed by 3D tomography in Figure 6.4h, 6.4i. The helix with tunable handedness changing from L-tartaric acid to D-

tartaric acid and the untwisted cylindrical morphology in neat PEO-*b*-PtBA confirm that this helical superstructure was transferred from the enantiopure tartaric acid additives.

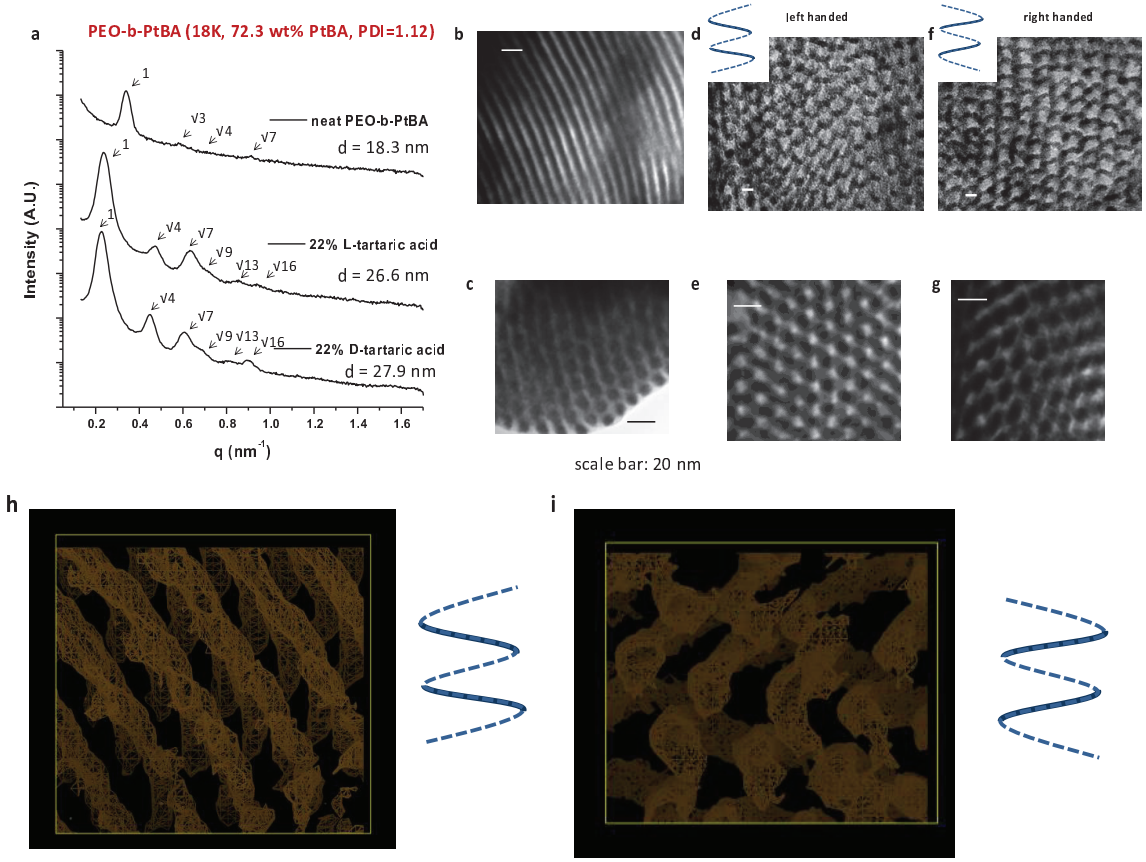

Figure 6.4 SAXS integrations (a) of neat PEO-*b*-PtBA (18K, 72.3 wt% PtBA, PDI=1.12), PEO-*b*-PtBA (18K, 72.3 wt% PtBA, PDI=1.12) blended with 22 wt% L-tartaric acid and with 22 wt% D-tartaric acid drop-cast from DMF. TEM characterization of neat PEO-*b*-PtBA (18K, 72.3 wt% PtBA, PDI=1.12) with projection perpendicular to the cylinder axis (b) and parallel to the axis (c), PEO-*b*-PtBA (18K, 72.3 wt% PtBA, PDI=1.12) blended with 22 wt% L-tartaric acid with projection perpendicular to the helix axis (d) and parallel to the axis (e), and PEO-*b*-PtBA (18K, 72.3 wt% PtBA, PDI=1.12) blended with 22 wt% D-tartaric acid with projection perpendicular to the helix axis (f) and parallel to the axis (g) after cryo-microtoming and RuO_4 staining. (h, i) 3D tomography for PEO-b-PtBA (18K, 72.3 wt% PtBA, PDI=1.12) blended with 22 wt% L-tartaric acid (h) and 22 wt% D-tartaric acid (i). All samples were annealed at 90°C for 36 hours before tests and all SAXS data were taken at 90°C above the melting point of PEO.

To better characterize the helical morphology in the PEO-*b*-PtBA/tartaric acid composite system, a rotatable sample holder was used to image the nanostructures from different angles. In Figure 6.5a and 6.5b, two TEM projection images of the same spot are shown during sample holder rotation. Figure 6.5a shows the micrograph of the plane projection with the direction parallel to the helix axis, while Figure 6.5b shows the micrograph of the plane projection with the sample holder rotating clockwise for 10^{o}. The projection with an angle 10^{o} away from the direction parallel to the helix axis in Figure 6.5b shows one helix linked with other adjacent helices, which helps to prove the formation of the 3-D helical structure in our system. Figure 6.5c shows interesting substructures observed in the sample with 22 wt% L-tartaric acid loading. Parallel lines were observed with a linewidth smaller than 1 nm in the dark regions, which is the PEO domain with L-tartaric acid as shown in Figure 6.5c. These substructures look very similar to DNA base-pairs in the double helix structures, which implies how the helices form in our system.

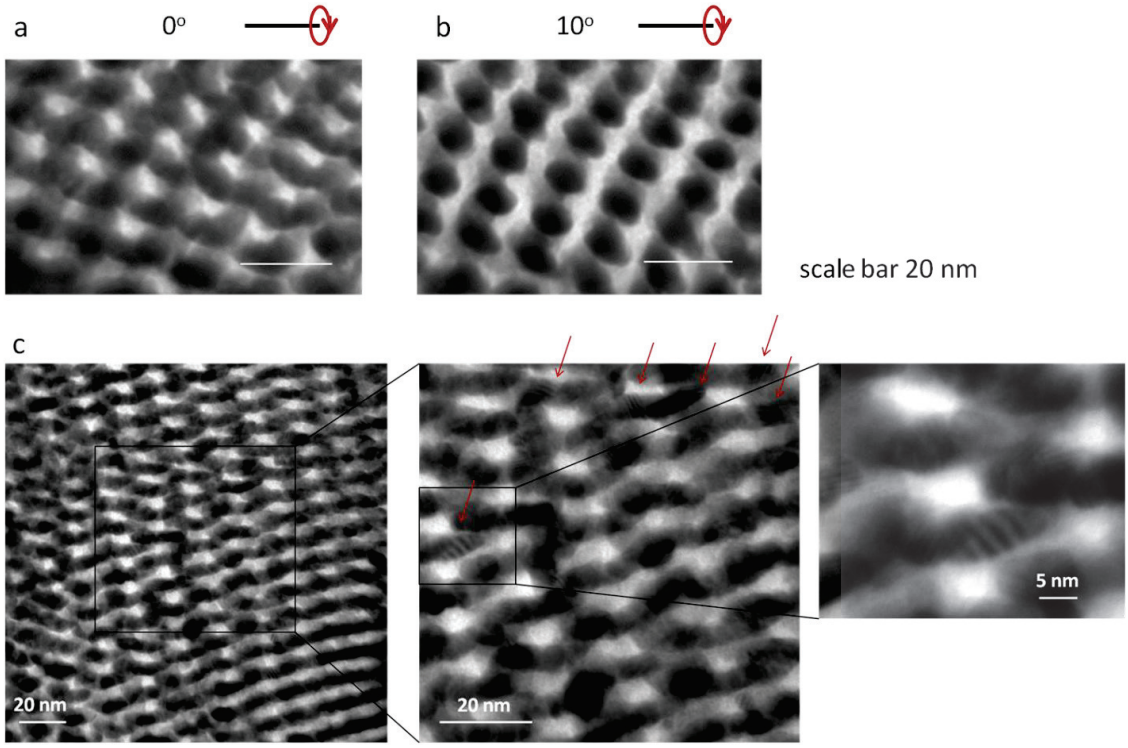

Figure 6.5 TEM characterization of PEO-*b*-PtBA (18K, 72.3 wt% PtBA, PDI=1.12) blended with 22 wt% L-tartaric acid with relative sample holder tilting angle as 0° (a) and after 10° clockwise rotation (b). Substructures (c) observed in TEM of PEO-*b*-PtBA (18K, 72.3 wt% PtBA, PDI=1.12) blended with 22 wt% L-tartaric acid.

In order to test the versatility of this chiral additive-driven helical superstructure formation, PEO-*b*-PtBA with different molecular weights and weight percentages were used to rule out the possibility that the helical superstrucuture can only be formed in PEO-*b*-PtBA with a very small window in the phase-diagram. Thus, the PEO-*b*-PtBA with a molecular weight of 13.9K, PtBA weight percentage of 64%, and a PDI of 1.12 was used, which was also synthesized through PEO end-group functionalization followed by ATRP. Figure 6.6a shows that the neat PEO-*b*-PtBA (13.9K, 64 wt% PtBA and PDI 1.12) is originally weakly segregated with a d-spacing around 18 nm. The addition of enantiopure tartaric acid, either L or D, again dramatically improved the ordering as shown in Figure 6.6a with increased d-spacing of 21~22 nm. The ratios of the q values of

those scattering peaks are also 1, √4, √7, √9, √13, √16. The interesting phenomenon is that with the addition of the racemic tartaric acid, no ordering improvement was observed even with an increased racemic acid loading amount as shown in Figure 6.6[251] The reason is that a racemic heteropair structure formed for racemic tartaric acid with the lowest energy level identified by phase pair identity density functional theory simulations,[252] which was also discussed in our previous work.[251] TEM was used to image the nanostructures inside of the new composites with enantiopure tartaric acids blended as the additives after staining with RuO_4 with the dark area showing PEO domain. Again right-handed helices were observed in the PEO-*b*-PtBA (13.9K, 64 wt% PtBA and PDI 1.12) blended with L-tartaric acid and left-handed helices for D-tartaric acid. A detailed study about the order-order transition during the loading of D-tartaric acid in PEO-*b*-PtBA (13.9K, 64 wt% PtBA and PDI 1.12) using SAXS is shown in Figure 6.7. Cylinder to lamellae transition was observed in SAXS with D-tartaric acid loading from 0 wt% to 10 wt% and lamellae to cylinder (twist) transition from 10 wt% to 20 wt% of D-tartaric acid loading. This order –order transition with increased D-tartaric acid loading amount helps to prove the phase inverse in the helix structure with 25 wt% D, or L-tartaric acid loading.

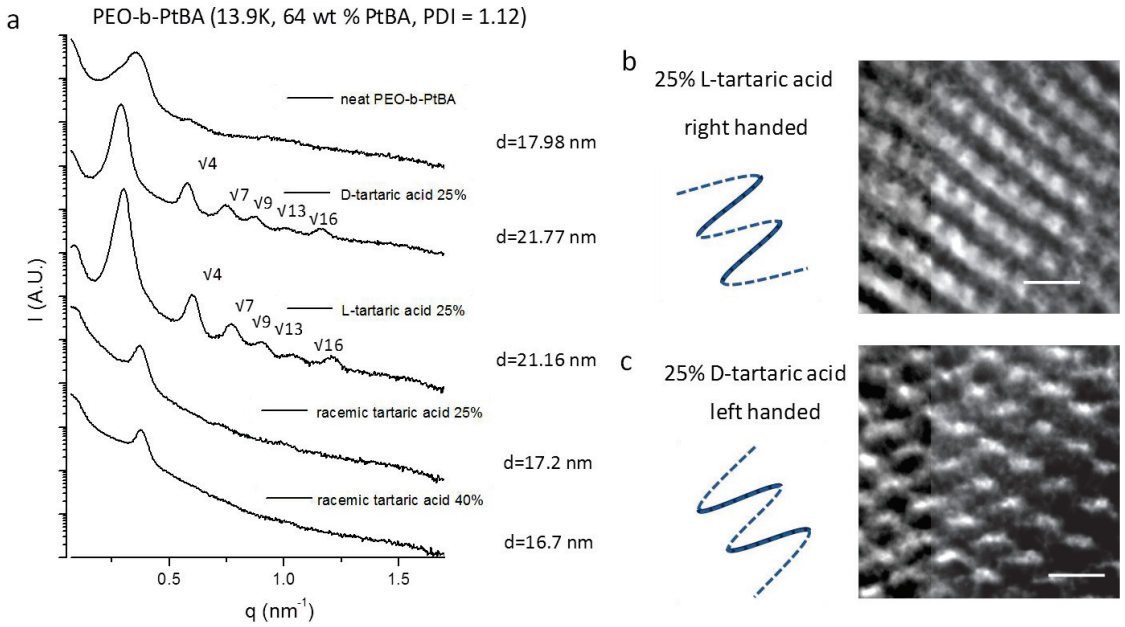

Figure 6.6 SAXS integrations (a) of neat PEO-*b*-PtBA (13.9K, 64 wt% PtBA and PDI 1.12), PEO-*b*-PtBA (18K, 72.3 wt% PtBA, PDI=1.12) blended with 25 wt% D-tartaric acid, 25 wt% L-tartaric acid, 25 wt% racemic tartaric acid, and 40 wt% racemic tartaric acid drop-cast from ethanol. TEM characterization of PEO-*b*-PtBA (13.9K, 64 wt% PtBA and PDI 1.12) blended with 25 wt% L-tartaric acid (b), and PEO-*b*-PtBA (13.9K, 64 wt% PtBA and PDI 1.12) blended with 25 wt% D-tartaric acid (c) after cryo-microtoming and RuO_4 staining. All samples were annealed at 90°C for 36 hours before tests and all SAXS data were taken at 90°C above the melting point of PEO.

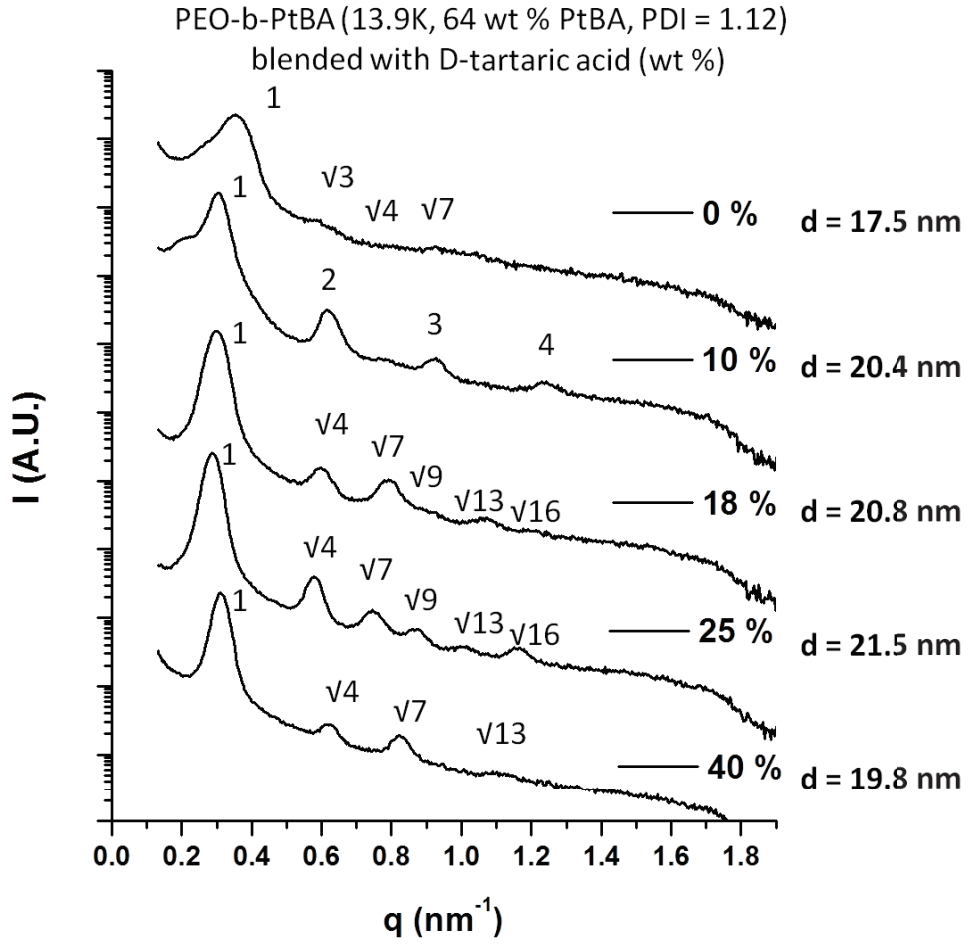

Figure 6.7 SAXS integrations of neat PEO-*b*-PtBA (13.9K, 64 wt% PtBA and PDI 1.12), PEO-*b*-PtBA (18K, 72.3 wt% PtBA, PDI=1.12) blended with 10 wt% D-tartaric acid, 18 wt% D-tartaric acid, 25 wt% D-tartaric acid, and 40 wt% D-tartaric acid drop-cast from ethanol.

The PEO-*b*-PtBA with 9.2K 46.6 wt% PtBA originally is ordered with only one order peak showing a d-spacing of around 13 nm. With 40 wt% L-tartaric acid loading, more high order peaks in SAXS were observed showing lamellae morphology assigned by the ratios of q values of those scattering peaks. To image the actual nanostructure, TEM was again applied after cryo-microtoming and followed by RuO_4 staining. However, no twisting for lamellar morphology was observed in TEM as shown in Figure 6.8, which might be due to the fact that the drive-force of enantiopure tartaric acid is not enough to

twist a lamellar morphology to form a helical phase. Twisting was also not observed in the PS-*b*-PDLA system for lamellae morphology. [253-254]

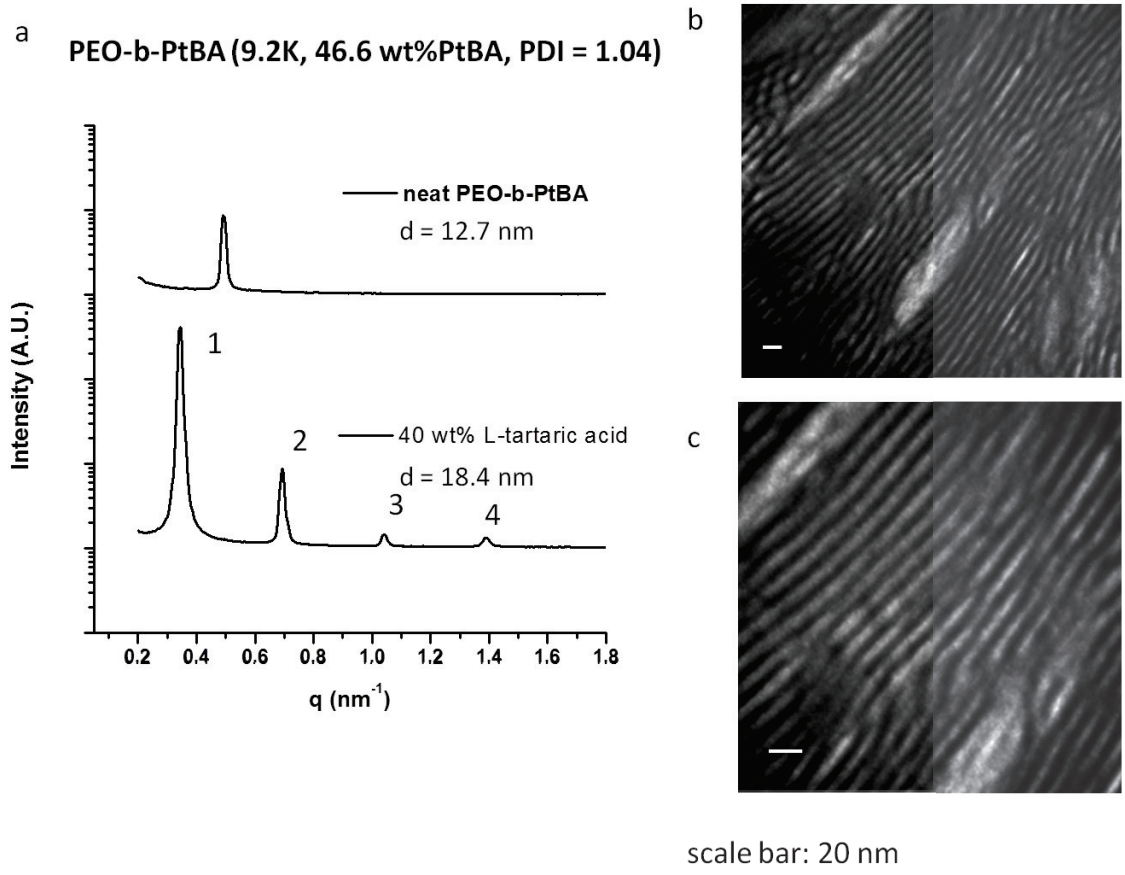

Figure 6.8 SAXS integrations (a) of neat PEO-*b*-PtBA (9.2K, 46.6 wt% PtBA and PDI 1.04), PEO-*b*-PtBA (9.2K, 46.6 wt% PtBA and PDI 1.04) blended with 40 wt% L-tartaric acid drop-cast from ethanol. TEM characterization of PEO-*b*-PtBA (9.2K, 46.6 wt% PtBA and PDI 1.04) blended with 25 wt% L-tartaric acid (b, c) after cryo-microtoming and RuO_4 staining. All samples were annealed at 90°C for 36 hours before tests and all SAXS data were taken at 90°C above the melting point of PEO.

6.4 Conclusion

To conclude, in this chapter we describe a novel method to achieve nanohelical phase in a bulk achiral block copolymer system by blending small chiral additives. We demonstrate that the chiral block copolymer backbone is not necessary for helical phase

formation. In our method, the hydrogen bonding between the additives and one of the blocks can help transfer the chirality from the additives into the polymer through the Domino effect. The chirality in the backbone of the supramolecules can then be transferred into the phase to form the nanohelical superstructure. Our methods can tolerate block copolymers with a relatively large window of molecular weight and volume ratio. We also show that phase reverse can happen upon loading tartaric acid in helical phase formation. No twisting was observed for lamellar morphology with chiral driving force, which is consistent with previous studies in other systems.

We point out that this chiral additive strategy provides an alternative way to achieve helical phase avoiding using the chiral block copolymer PS-*b*-PLLA and also the triblock terpolymers SBM with very specific volume ratios. Thus, using the system designed here, achiral block copolymers with different functionalities can be incorporated in this method, which can dramatically broaden the potential application of the nanohelical phase. Order-disorder transition can be applied for PtBA block upon being deprotected into PAA to form hierarchical patterns[251] with the helical superstructure. Other blocks can also be chosen instead of PtBA, for example UV-degradable block poly(methyl methacrylate) (PMMA), high etch resistance block polydimethylsiloxane (PDMS) and ionic conducting block polystyrenesulfonate (PSS) to make broad applications of the helical nanostrucuture possible.

CHAPTER 7

ULTRA-HIGH LOADING OF NANOPARTICLES IN ORDERED BLOCK COPOLYMER COMPOSITES

7.1 Introduction

Polymer/inorganic hybrid materials with well ordered structures have attracted enormous attention in recent years due to their many potential applications, including microelectronics, energy conversion, photonic devices, and sensors. [1, 250, 255-263] The utility of these hybrid materials for a specific application is often dependent not only on the size, shape, and orientation of the ordered domains, but also on the loading of the active nanoparticle (NP) constituent. Despite a significant amount of research,[168, 264-271] straightforward, general methods for achieving the latter goal are lacking.

The realization of ordered block copolymer/NP systems results from an energy balance between enthalpic and entropic contributions: the enthalpic contribution is controlled by the interaction between the additive and the block copolymer segments, while the entropic contribution arises in part from the chain stretching penalty for accommodating NPs.[41, 272] To date, most studies of NP incorporation in BCPs have involved NP ligands that are chemically identical to one of the blocks, yielding an enthapically neutral interaction, or NP ligands that exhibit weak interactions with the target domain.[168, 264-271] In these cases, the entropic penalty for NP incorporation can easily dominate the system resulting in low NP loadings, particle aggregation/macrophase separation, or loss of order.

To achieve high loading of the NPs while maintaining ordered structures, the BCP/NP system needs to be optimized in order to either be enthalpically favorable or to reduce the entropic penalties for NP incorporation. The Xu group[272] took the latter approach to relieve entropic penalties in a composite system by introducing 3-n-pentadecyl phenol or 4-(4'-octylphenyl)azophenol into poly(styrene-block-4-phenylpyridine) hosts for NPs functionalized with alkane ligands as shown in Figure 7.1b. The polar head groups of the additives hydrogen bond with the PVP block of the copolymer to supramolecular assemblies bearing alkane comb structures, which in turn interact with the alkane ligands of the NPs through dispersion interactions. While the NP ligand interactions with the polymer assemblies are weak, the creation of the comb structure, which contains many additional chain ends, reduces the entropic penalty for NP incorporation.

To date, surprisingly few studies[41, 273-276] have focused on the use of strong, favorable enthalpic interactions between the BCP and NP ligands to offset the entropic chain stretching penalty. Wisener's group demonstrated co-assembly of metal NPs coated with an organic shell comprised of ionic liquid coatings and specially designed poly(isoprene-block-dimethylaminoethyl methacrylate) BCPs for the purpose of creating mesoporous metal assembles,[273] however their system employed very specific chemistries and cumbersome processing. More recently, our group developed an approach called additive-driven self-assembly,[37-39] to achieve strong microphase segregation in block copolymers that are otherwise disordered or weakly segregated by blending them with homopolymers,[37] small molecule additives[39-40], or nanoparticles.[41] We demonstrated that selective H-bonding interactions between the additives and one

block of the block copolymer can effectively enhance the segregation strength of the system. This method offers a general approach to well-ordered polymer/NP composites by blending nanoparticles, which are functionalized with short H-bond-donating ligands, with block copolymers containing H-bond-accepting segments.[41] In one study we used 4-hydroxythiophenol-functionalized Au (Au-OH) NPs as the H-bond-donating additives and the PEO blocks of Pluronic surfactant block copolymers poly(ethylene oxide)-block-poly(propylene oxide)-block poly(ethylene oxide) (PEO-*b*-PPO-*b*-PEO) and poly(ethylene oxide)-*b*-polystyrene (PEO-*b*-PS) diblock copolymers as the H-bond-accepting segments as shown in Figure 7.1a. Well ordered composites with Au-OH NP loadings of about 0.77 (weight ratio of Au NPs relative to PEO) were achieved using otherwise disordered or weakly segregated block copolymers hosts.

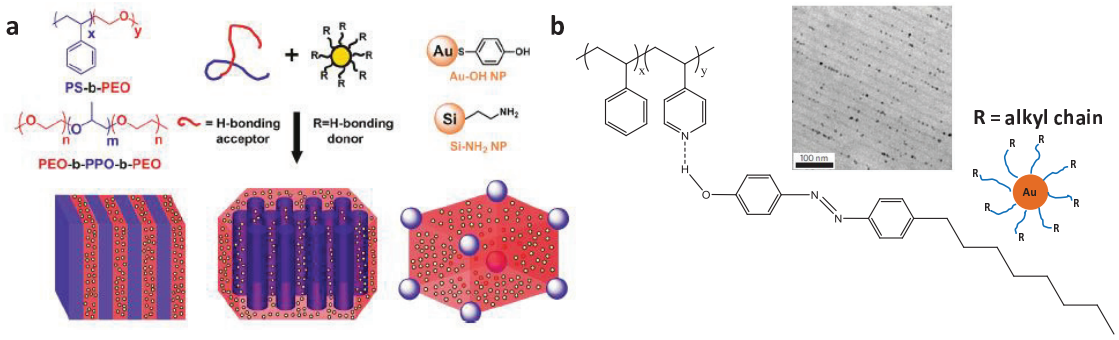

Figure 7.1 (a) Nanoparticle assembly in block copolymer composites through enthalpic interaction enhancement between ligands of nanoparticles and the host domain, adapted from Ref; [41] (b) Nanoparticle assembly in block copolymer composites directed by small molecules, adapted from Ref.[272]

In this chapter, we report a method for the ultrahigh loading of NPs in well-ordered block copolymer/additive systems through the consideration of both enthalpic and entropic factors. By incorporating small molecule additives (organic acids) that interact with both the NP ligand and one segment of the block copolymer host, the NP

loading limit is dramatically increased. The role of the organic acid is three-fold. First, it acts as an H-bond-donating additive to induce microphase separation in otherwise disordered or weakly segregated systems; the segregation strength of the block copolymer system is enhanced through the selective interaction of the acid with the PEO block. This interaction generates ordered structures in even low molecular weight systems. Additionally, the volume fractions of the systems can be tuned by varying the acid loading, providing a facile means for achieving the desired morphology. Second, the acid can provide additional H-bond-accepting sites in a well-segregated amphiphilic system. The multiple carboxylic acids groups of the acid molecule make confinement of additional H-bond-donating NPs in the hydrophilic domain possible. The much stronger H-bonding interaction between carboxylic acid groups of the acid and the hydroxyl groups of the ligands of NPs enhances the favorable interaction between the NPs and hydrophilic domain. Third, the small additives in the PEO domain help alleviate the entropic penalties associated with NP incorporation by both increasing the configurational entropy of the system and by reducing the conformational entropy loss by swelling of the BCP domains. In this context the tartaric acid plays the role of a selective solvent in a BCP composite system.[277] Thus, ultra-high metal content and precise particle distribution in the BCP system can be achieved with improved ordering.

7.2 Experimental

7.2.1 Materials

Poly(ethylene oxide-*b*-*tert*-butyl acrylate) (PEO-*b*-PtBA) diblock copolymer was synthesized using atom transfer radical polymerization (ATRP) following the established procedures,[93] with slight modifications; D-tartaric acid was purchased from Sigma-

Aldrich; Au-OH nanoparticles (NPs) with the diameter of 2-3 nm functionalized with 4-hydroxythiophenol were synthesized following the established procedures.[278] Ruthenium tetraoxide (RuO_4) 0.5 wt% aqueous solution was purchased from Electron Microscopy Sciences.

7.2.2 Preparation of bulk samples for small-angle X-ray

PEO-*b*-PtBA, D-tartaric acid, and Au-OH NPs were blended at a given mass ratio in dimethylformamide (DMF) of a certain weight percentage (BCP concentration of 2~3 wt%). After dropped cast from the DMF solution onto glass slides, dried at room temperature (r.t.), annealed for 36 h at 90°C under vacuum, and then cooled to r.t. under vacuum, the bulk samples were scraped off the glass slides, and then evenly placed in the center of metal washers sandwiched by Kapton film.

7.2.3 Characterization

Small angle X-ray scattering (SAXS). The samples were placed on a heated vertical holder which was equilibrated at 90°C for about 20 min under vacuum. The whole system was under vacuum during the measurements which were done at UMass Amherst using an in-house setup from Molecular Metrology Inc. (presently sold as Rigaku S-Max3000) with the wavelength of 0.1542 nm and sample to detector distance of 1477 mm.

Transmission electron microscopy (TEM). Cryo-microtoming was used to cut the bulk sample into pieces with the thickness of 50 nm, which is thin enough for electron beam going through, with the cutting atmosphere temperature of -120°C and knife temperature of -110°C below the glass transition temperature (Tg) of PEO block. A JOEL 2000FX electron microscope which was operating at 200 kV was used. The samples are

either without any staining, or stained using ruthenium tetraoxide (RuO_4) with the vapor concentration of 2 ml 0.5 wt% aqueous solution in 250 ml jar for 3 minutes and 10 minutes.

Thermogravimetric analysis (TGA) was performed on a TGA 500 thermogravimetric analyzer heating at a rate of 10 °C/min from room temperature to 800^{o}C under a continuous purge of nitrogen.

7.3 Results and Discussion

We used enantiopure tartaric acid, which was used in our previous studies of disordering transitions for hierarchical pattern formation, as the organic acid additive.[251] Tartaric acid is a chiral acid that contains two stereocenters in its backbone as well as multiple H-bond-donating and H-bond-accepting groups, including carboxylic acid and hydroxyl groups as shown in Figure 7.2c. Here, enantiopure D-tartaric acid was used rather than racemic tartaric acid because the enantiomers in the racemic mixture interact more strongly with each other than they do with the ether groups of the PEO block.[251] We used poly(ethylene oxide-block-*tert*-butyl acrylate) PEO-*b*-PtBA (Figure 7.2a) as the BCP host and gold NPs functionalized with 4-hydroxythiophenol (Au-OH) as the nanoparticle additives (Figure 7.2b). In Figure 7.2d we illustrate that blending D-tartaric acid into the PEO-*b*-PtBA BCP system creates additional H-bond-accepting groups in the hydrophilic PEO domain.

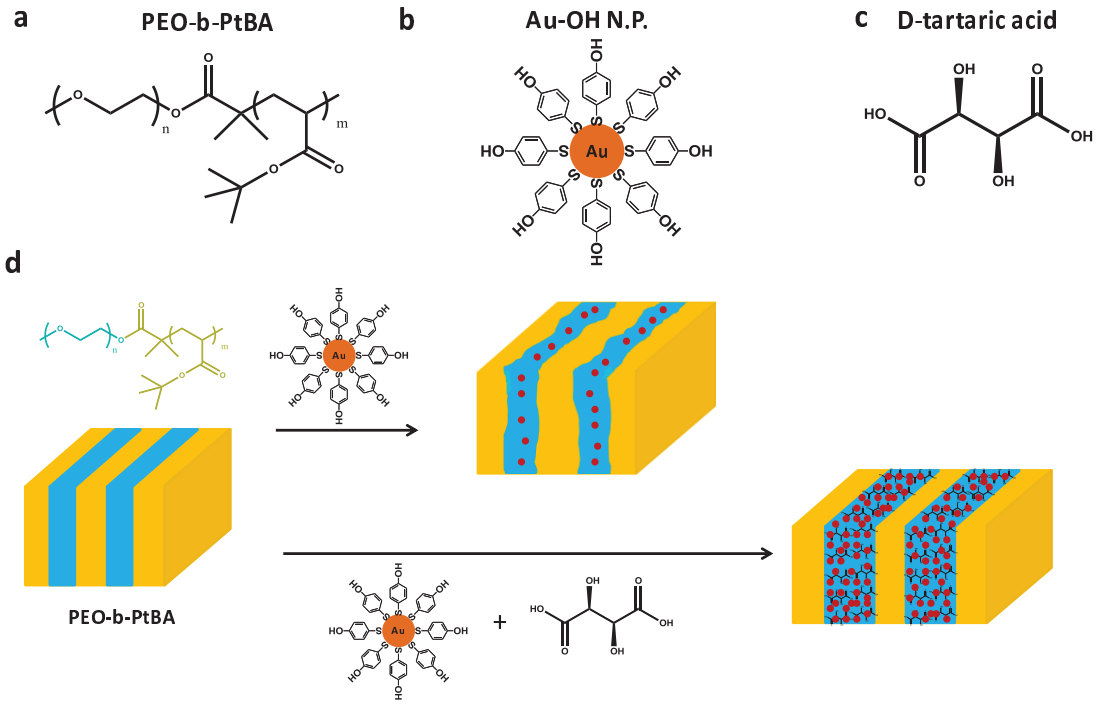

Figure 7.2 Structures of PEO-*b*-PtBA (a), Au-OH NPs with 4-hydroxythiophenol as ligands (b) and D-tartaric acid (c); (d) Schematic demonstration of PEO-*b*-PtBA blended with only Au-OH NPs and Au-OH NPs together with D-tartaric acid.

For consistency, we express the composition of the hydrophilic domain (PEO : tartaric acid) as the mass ratio of PEO to tartaric acid. We express loadings of Au NPs within composites by the mass ratio of Au NPs to either neat PEO block or the PEO block plus tartaric acid. These are denoted as Au NPs : PEO or Au NPs : (PEO+tartaric acid). Thermogravimetric analysis (TGA) indicated that the Au-OH NPs used in this study contain ~72% Au by weight, the balance is ligand.[41] Using this information, Au loadings relative to a variety of basis can be calculated. We use TGA to verify these calculations by computing the Au mass fractions of the ordered composites (vide infra).

PEO-*b*-PtBA BCP with a molecular weight of 18K, 72.3 wt % PtBA, and PDI of 1.12 (denoted as PEO5K-*b*-PtBA13K) was used as the host. Au (Au-OH) NPs with the

diameters of ca. 2-3 nm functionalized with 4-hydroxythiophenol were synthesized using the same procedure as our previous study[41] following the literature procedures with slight modification.[278] The small angle x-ray scattering (SAXS) profile for neat PEO5K-*b*-PtBA13K is shown in Figure 7.3a, and the higher order reflections indicate an ordered cylindrical morphology, with a d-spacing of 18.5 nm. By blending Au-OH NPs (Au NPs : PEO, 1.08 : 1), into PEO5K-*b*-PtBA13K, the d-spacing was increased from 18.5 nm to 22.1 nm. However, the scattering peaks were heavily attenuated with a large increase in the full width at half maximum intensity, indicating significant weakening in the strength of segregation. The loss in intensity occurs despite an expected increase in the electron density contrast of the two domains. By contrast, the addition of D-tartaric acid (PEO : tartaric acid, 56 : 44) into the system with the same amount of Au NPs (Au NPs : PEO, 1.08 : 1 or Au NPs : (PEO+tartaric acid), 0.60 : 1) yielded well-defined scattering peaks (Figure 7.3a), revealing a lamellar morphology as indicated by the ratios of the multiple higher-order peaks to the primary peak (1:2:3:4:5:6) and a d-spacing of 28.7 nm. The well-resolved higher-order peaks confirm the excellent ordering with good electron density contrast between the two domains, indicating that the NPs were selectively confined to one domain. Not surprisingly, the ultra-high loading of the additives changes the volume fraction of the system and can lead transitions between ordered morphologies. We further demonstrated that Au-OH NPs with the amount as high as 1 : 1 (Au NPs : (PEO+tartaric acid)), can be loaded in PEO5K-*b*-PtBA13K as shown in the Figure 7.3a.

Transmission electron microscopy (TEM) was used to characterize the detailed structure of the system and to confirm the location of the NPs. The TEM images in Figure 7.3b show the well-ordered lamellar morphology of the sample without any

staining. Individual nanoparticles that are densely packed and confined in one domain are clearly resolved in the image. Ruthenium tetraoxide (RuO4) vapor (2 ml 0.5 wt% solution in 250 ml jar) was used to stain the PEO domain (Figure 7.3c and 7.3d). The clear contrast in both TEM images helps confirm that the nanoparticles were confined solely to the PEO domain.

To achieve ultra-high Au content of the composite system, we used a PEO-*b*-PtBA BCP with higher PEO volume fraction as the loading substrate. The molecular weight of the PtBA block in the new copolymer (denoted as PEO5K-*b*-PtBA4.2K) with a PDI of 1.04, was reduced to 4.2K (from 13K) while the molecular weight of the PEO block was maintained at 5K. D-tartaric acid (PEO : tartaric acid, 58 : 42) was added into the system to allow for the ultra-high loading of NPs. Both TEM and SAXS were again used to confirm the loading of Au-OH nanoparticles. As shown in Figure 3a, ordered lamellar morphology was observed in TEM for the sample with Au-OH NPs loading amount as high as 1.07 : 1 (Au NPs : (PEO+tartaric acid)). The SAXS profiles in Figure 7.4b show that ordering peaks were clearly observed even with the Au-OH NPs were added at a loading of 1.50 : 1 (Au NPs : (PEO+tartaric acid)). A meaningful comparison to NP loadings in our previous study requires consideration of NP loading with respect to the both PEO mass in the copolymer and the total mass of the target domain, which includes tartaric acid in the present study. The weight ratio of Au-OH NPs to PEO block is up to 2.63 in this study compared to 0.77 in the previous study. When normalized for the mass of all organic compounds in hydrophilic domain (PEO plus D-tartaric acid if any) the ratio is up to 1.5 for this study, nearly twice the ratio of 0.77 achieved in our previous study.

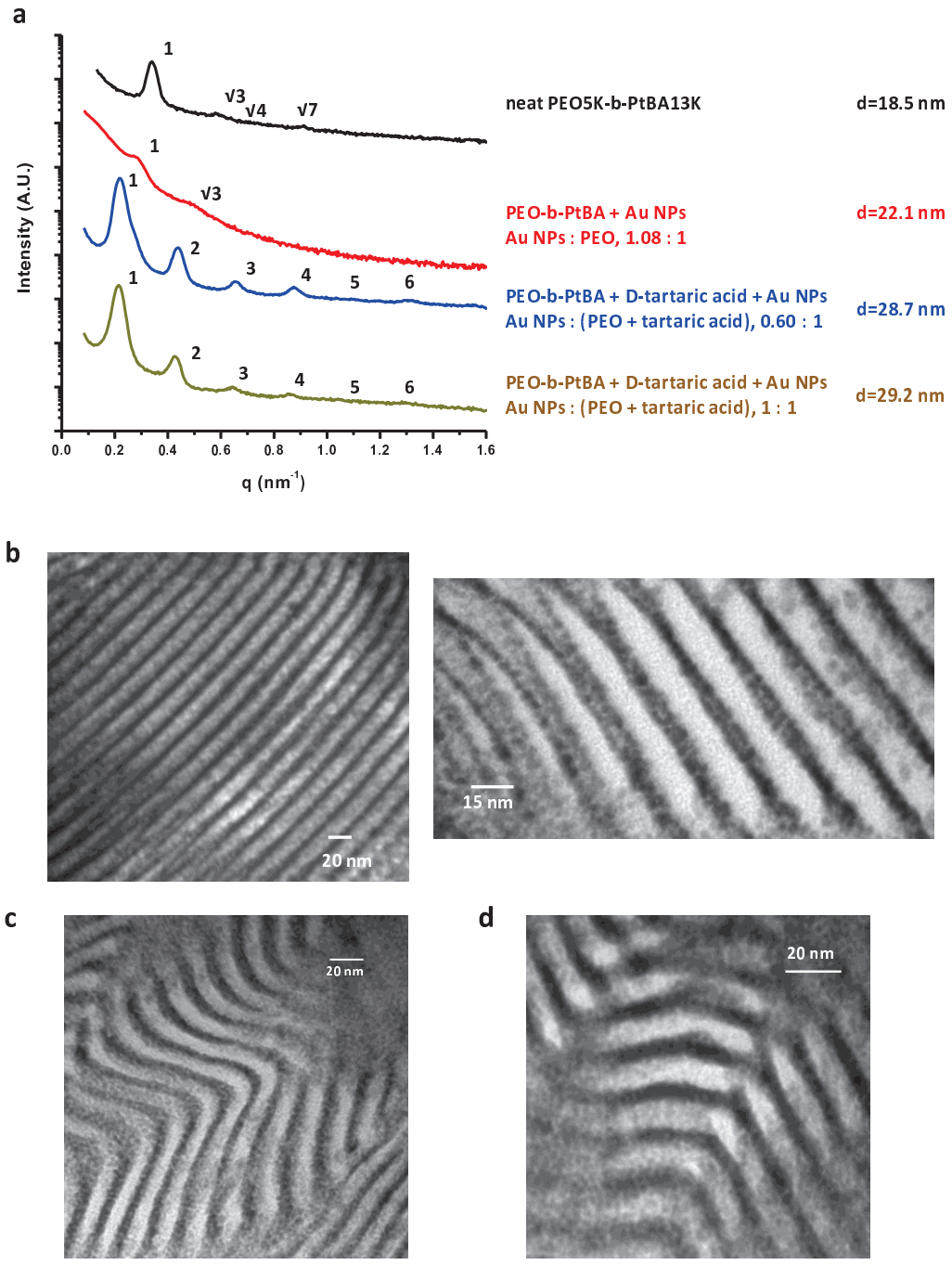

Figure 7.3 (a) SAXS profiles of neat PEO-*b*-PtBA (18K, 72.3 wt % PtBA, PDI = 1.12); PEO-*b*-PtBA blended with Au-OH NPs (Au NPs : PEO, 1.08 : 1); PEO-*b*-PtBA + D-tartaric acid (PEO : tartaric acid, 56 : 44) blended with Au-OH NPs (Au NPs : (PEO+tartaric acid), 0.60 : 1); PEO-*b*-PtBA + D-tartaric acid (PEO : tartaric acid, 56 : 44) blended with Au-OH NPs (Au NPs : (PEO+tartaric acid), 1 : 1). (b~d) TEM images of PEO-*b*-PtBA (18K, 72.3 wt % PtBA, PDI = 1.12) + D-tartaric acid (PEO : tartaric acid, 56 : 44) blended with Au NPs (Au NPs : (PEO+tartaric acid), 0.60 : 1), after cryo-microtoming without staining (b), with RuO4 staining for 3 min (c), and with RuO4 staining for 10 min (d).

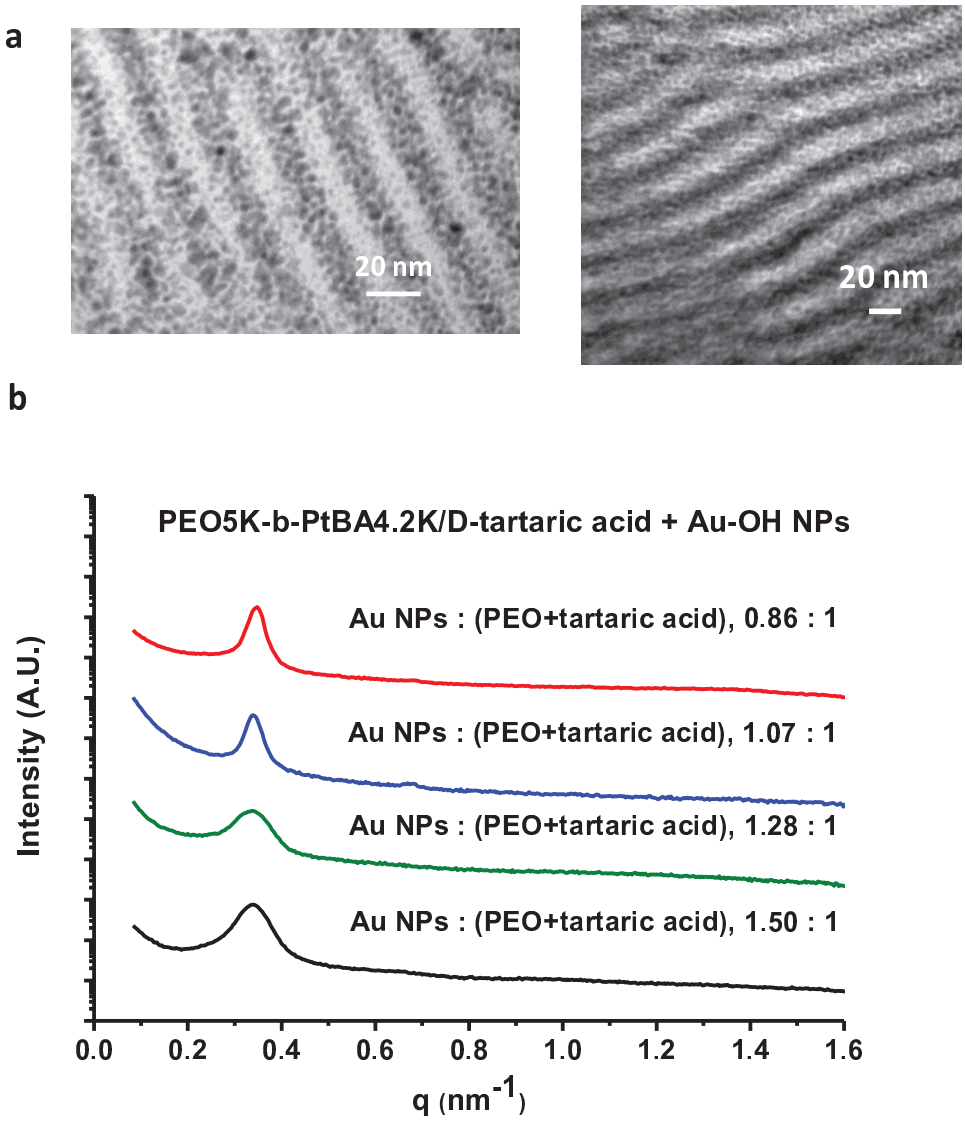

Figure 7.4 (a) TEM images of PEO-*b*-PtBA (9.2K, 46.6 wt% PtBA, PDI = 1.04) + D-tartaric acid (PEO: tartaric acid, 58 : 42) blended with Au-OH NPs (Au NPs : (PEO+tartaric acid), 1.07 : 1). (b) SAXS profiles of PEO-*b*-PtBA+D-tartaric acid (PEO : tartaric acid, 58 : 42) blended with different amounts of Au-OH NPs (Au NPs : (PEO+tartaric acid), 0.86 : 1, 1.07 : 1, 1.28 : 1, 1.50 : 1).

TGA was used to confirm inorganic content in the system. The Au content in the Au-OH NPs used here is ~72 wt%.[41] With Au-OH NP, 0.86 of Au NPs : (PEO+tartaric acid), loaded into a PEO5K-*b*-PtBA4.2K/D-tartaric acid (PEO : tartaric acid, 58 : 42) composite system, the calculated Au content of the total compound is 26%. The

experimental result from TGA in Figure 7.5a showed that the inorganic compounds that remained after heating to 800°C made up ~28% of the compound. With Au-OH NPs (Au NPs : (PEO+tartaric acid), 1.28 : 1) loaded, the calculated Au content should be 39%, while the experimental result from TGA in Figure 7.5b gave the percentage of inorganic compounds left to be about 42%. A control experiment in Figure 4c shows that about 3% of the neat PEO5K-*b*-PtBA4.2K/D-tartaric acid composite (PEO : tartaric acid, 58 : 42) is left after heating without any NP loading due to the carbonization of the organic compounds in the system. After subtracting the carbonization residue in each case, all the experimental Au-OH contents match well with the calculated results.

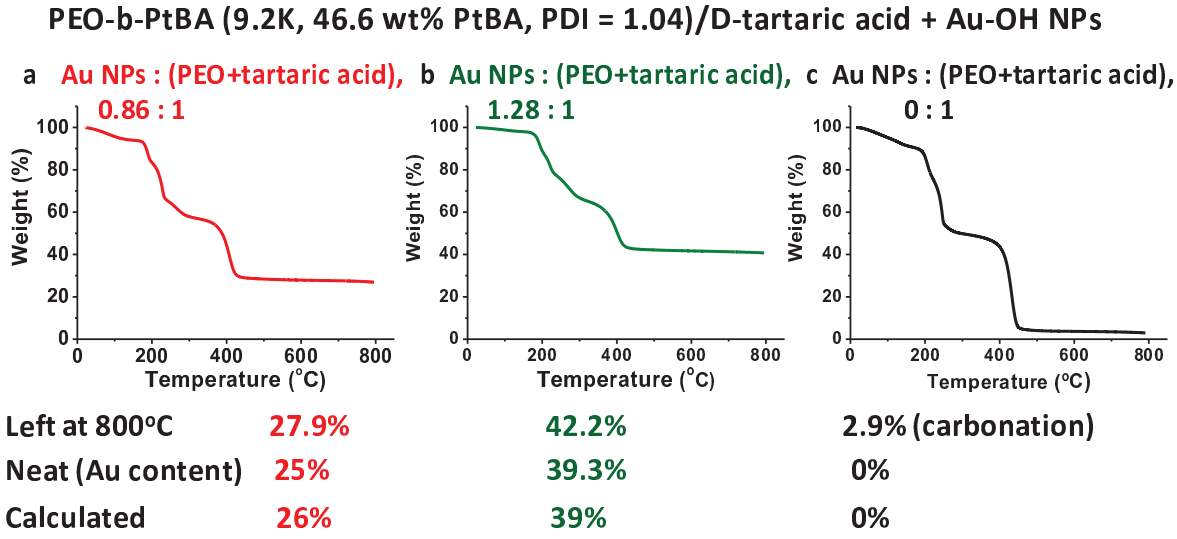

Figure 7.5 TGA of PEO-*b*-PtBA (9.2K, 46.6 wt% PtBA, PDI = 1.04) + D-tartaric acid (PEO : tartaric acid, 58 : 42) blended with different amounts of Au-OH NPs (Au NPs : (PEO+tartaric acid), 0.86 : 1 (a), 1.28 : 1 (b), 0 : 1 (c)). For (a) 27.9% remaining after 800°C with 25% Au (measured), 26% Au (calculated); for (b) 42.2% remaining after 800°C with 39,3% Au (measured), 39% Au (calculated); for (c) 2.9% remaining after 800°C, 0% Au (measured), 0% Au (calculated).

To further illustrate the concept, we studied morphology and d-spacing development in the PEO-*b*-PtBA composite system through the comparison of neat PEO-*b*-PtBA, PEO-*b*-PtBA blended with only D-tartaric acid, and PEO-*b*-PtBA blended with both D-tartaric acid and Au-OH NPs. The SAXS profiles in Figure 7.6 show that ordering was dramatically improved after blending D-tartaric acid (PEO : tartaric acid, 58 : 42) into the neat PEO-*b*-PtBA (PEO5K-*b*-PtBA4.2K). The ratios of ordering peaks to the primary peak are 1:2:3:4, indicating lamellar morphology. The d-spacing was also dramatically increased from 12.7 nm to 17.5 nm. DSC and WAXS studies in our previous work[251] showed that the interaction between D-tartaric acid and PEO domain was strong enough to inhibit the crystallization of PEO, indicating that the D-tartaric acid resided in the PEO domain. By blending an additional Au-OH NPs with the loading amount, 1.07 : 1 (Au NPs : (PEO+tartaric acid)), into the system, the d-spacing increased to 18.6 nm.

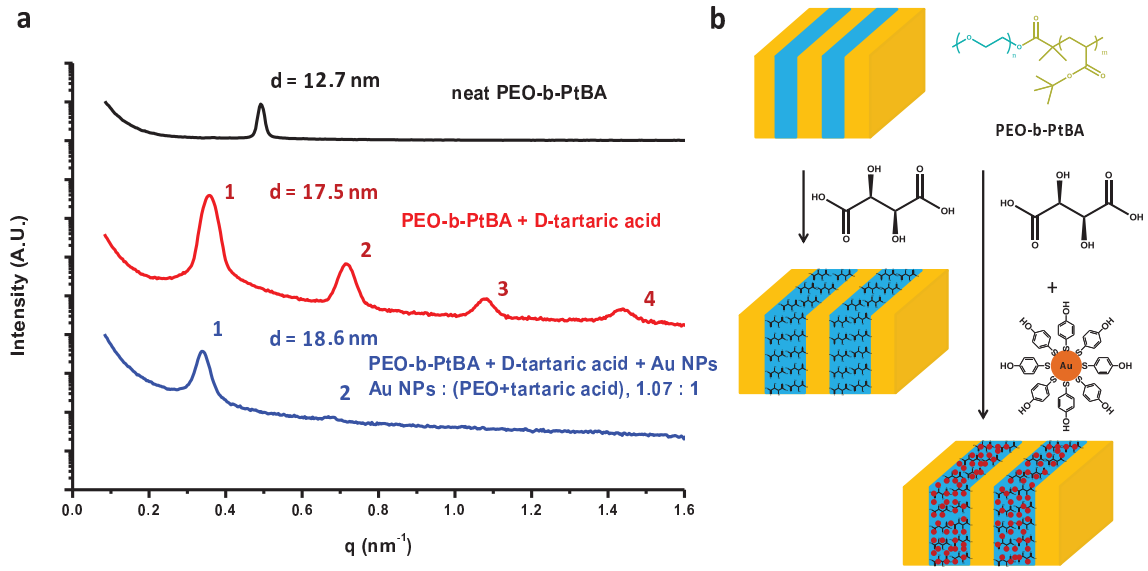

Figure 7.6(a) SAXS profiles of neat PEO-*b*-PtBA (9.2K, 46.6 wt% PtBA, PDI = 1.04); PEO-*b*-PtBA + D-tartaric acid (PEO : tartaric acid, 58 : 42); PEO-*b*-PtBA + D-tartaric acid (PEO : tartaric acid, 58 : 42) blended with Au-OH NPs (Au NPs : (PEO+tartaric acid), 1.07 : 1); (b) Schematic representation of PEO-*b*-PtBA blended only with D-tartaric acid and D-tartaric acid together with Au-OH NPs .

7.4 Conclusion

In conclusion, we have demonstrated a simple and efficient pathway for the fabrication of well ordered organic/metal hybrid materials with ultra-high NP content. In introduction of small molecule additives that hydrogen bond with the nanoparticle ligands and one segment of the block copolymer host enables high loading of NPs is well ordered composites through the introduction of favorable enthalpic interactions, increases in segregation strength and mitigation of entropic penalties for NP incorporation. High NP loading are essential for many applications of ordered polymer/NP composites. We further note that this method provides advantages for the practical fabrication of well-ordered functional hybrid nanomaterials via large-scale manufacturing (e.g. roll-to-roll coating).

CHAPTER 8

FINAL COMMENTS AND OUTLOOK

In this work, functional nanomaterials have been fabricated through manipulating and replicating block copolymer 3D structures. Mesoporous silica films with large pores of tunable geometry were fabricated through a supercritical fluid infusion process. The film structure can be excellently controlled due to the separation of template organization and silica network formation. By tuning the molecular weight, volume fraction of the segments, and PDI of the block copolymer, pore size can be controlled; high molecular weight and high PDI polymer templates can be used to create ultra-large pores in mesoporous silica films. Modifying the film thickness and annealing conditions can optimize the morphology and direct the orientation of cylindrical pores and packing method of spherical pores.

Directed self-assembly onto topographic guiding patterns, fabricated via photolithography, was used to achieve cylindrical alignment in PS-*b*-PtBA. A supercritical carbon dioxide infusion process and subsequent calcination step were then used to precisely replicate the pre-formed 3-D structures of the PS-*b*-PtBA films into mesoporous silica films, creating well aligned mesochannels. By separating the structure formation step from the silica condensation step in this process, 1-D alignment of cylinders in the template can be more easily controlled. In addition to AFM and TEM analysis, GISAXS was used to confirm the long-range alignment of the mesochannels over a large area. Control experiments not only helped confirm the reliability of GISAXS

methods in the alignment measurement, but also gave important parameters in the geometry of the topographic patterns on the substrates for alignment in this system.

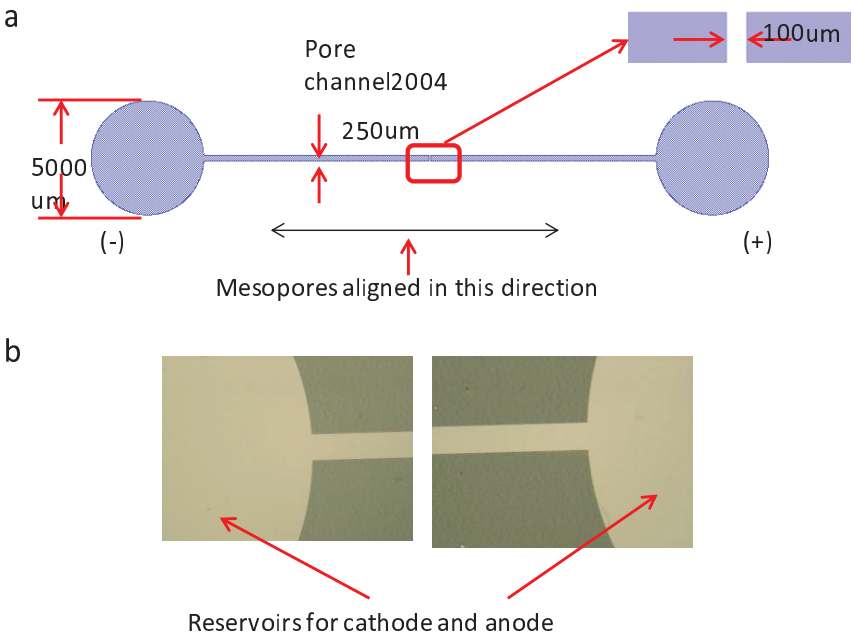

Figure 8.1 (a) Schematic demonstration of the microfluidic device for DNA separation. (b) Optical microscopy images of the reservoirs for cathode and anode after photolithography.

Potential applications of well-aligned mesochannels inside mesoporous silica films will be investigated. For example, DNA separation device can be built up based on the massively aligned mesochannels as shown in Figure 8.1. Two reservoirs which are linked by a channel can be fabricated using photolithography on the mesoporous silica film. The direction of the reservoir channel is aligned with the mesochannels as shown in Figure 8.1a. The center of the reservoir channel contains a block comprised of the mesoporous silica with well-aligned open-ended mesochannels. By applying an electric field between the two reservoirs containing charged DNA solution, only the DNA with a radius of gyration smaller than the pore diameter can move through the block from one

reservoir to the other, otherwise it will be excluded. This device will be ideal for DNA separation based on size and charge properties.

Bicontinuous mesoporous silica films have also been fabricated in supercritical CO_2 by replicating the gyroid morphology in PS-*b*-PtBA films. The orientation of the gyroid morphology with the [211] face parallel to the substrate was confirmed by AFM and GISAXS. Important lattice parameters were also calculated based on the obtained GISAXS results. The bicontinuous structure inside of the mesoporous silica films bypass the difficulties involved in the alignment of a cylindrical morphology to provide accessible channels. This makes the mesoporous silica film with bicontinuous channels a very good candidate for separation membranes.

A method to achieve submicrometer patterns of order-disordered regions through photo-induced disorder in a PEO-*b*-PtBA/tartaric acid was also presented. The chemically amplified deprotection of the tBA block transform the PtBA into PAA to induce a disordering transition of the system. The roles of the tartaric acid additive are two folds. First, it enhances the segregation strength of PEO-*b*-PtBA through the selective interaction with PEO block via hydrogen bonding. Second, PEO crystallization is completely suppressed by tartaric acid, making the formation of high-resolution patterns possible. Area-selective UV exposure was used to achieve the order-disorder hierarchical patterns by blending photo-acid generator and using a photo-mask. The suppression of acid diffusion was investigated in order to obtain high-resolution patterns. Conditions optimization for a swift disordering transition during post-exposure baking was tracked by GISAXS and a trace-amount of base quencher blended into the system successfully inhibited the acid diffusion, achieving submicron order-disorder hierarchical patterns.

The potential applications of using this additive strategy were also discussed. As shown in Figure 8.2, a high-etch-resistance additive, for example molecular glass, would be confined in the PEO-rich domains in the ordered regions while being evenly dispersed in the disordered regions of the BCP films. This would lead to selective etching of the PtBA domains only in the ordered regions, leaving hierarchical patterns for semiconductor applications. Different kinds of molecular glass with the cross-linking reagent tetra methoxymethyl glycoluril (TMMGU) will be used as the additives to be blended with PEO-*b*-PtBA. Two molecular glasses will be initially chosen in this study: MG2OH and MGCOOH as shown in Figure 8.3a, c. Bulk samples of PEO-*b*-PtBA blended with different amounts of additive will be made and annealed at 90°C for 36 h under vacuum. SAXS will be used to characterize the morphology in the bulk system to select the appropriate additive and amount.

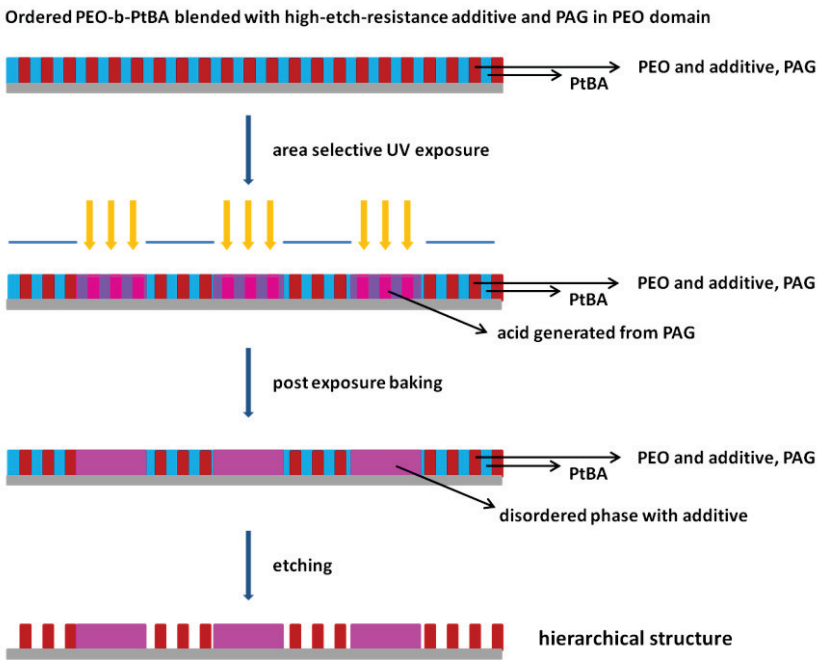

Figure 8.2 Schematic illustration of the process of hierarchical structure formation through etching from order-disorder patterns containing additive that exhibits strong etch resistance.

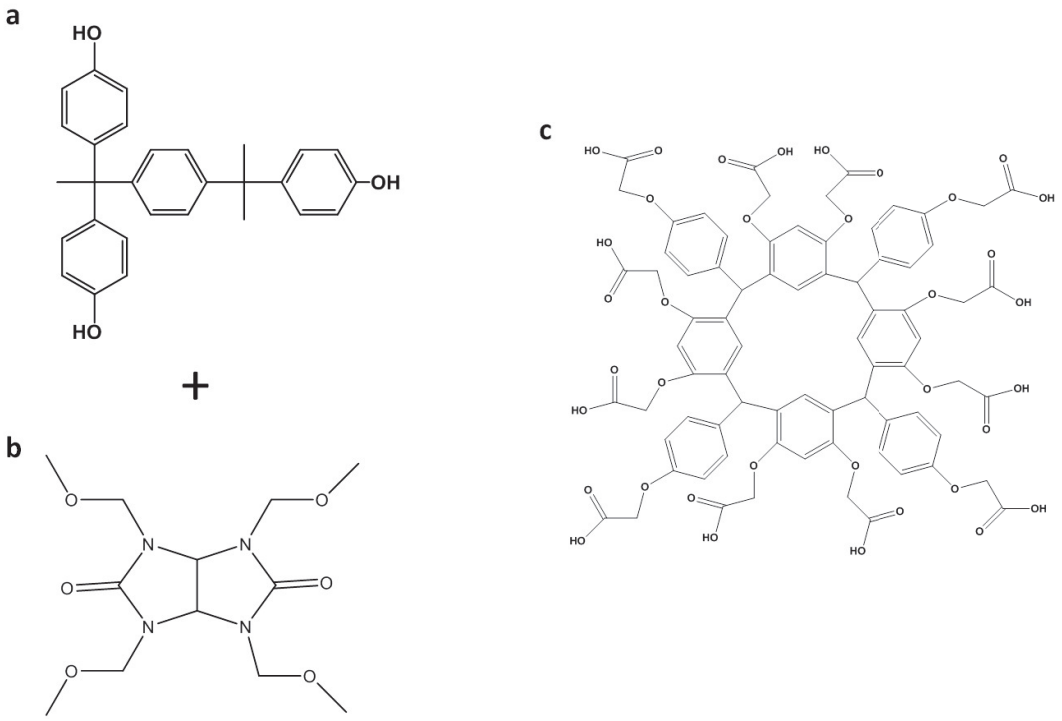

Figure 8.3 The structures for (a) MG2OH, (b) TMMGU and (c) MGCOOH.

The formation of nanohelical phase in a bulk achiral block copolymer system by blending small chiral additives was presented. The hydrogen bonding between the additives and one of the blocks helps transfer the chirality from the additives to the polymer through the Domino effect. The handedness of those helices can be simply tuned by using appropriate enantiomers of tartaric acid. We note that a chiral block copolymer backbone is not required for achieving helical phase. This method can also create helical superstructures in block copolymers with a relatively large window of molecular weight and volume ratio. Thus, the chiral block copolymer PS-*b*-PLLA and also the triblock terpolymers SBM with very specific volume ratios are not necessary for nanohelical phase formation. The hierarchical patterns with helical superstructures can be achieved

through a order-disorder transition by utilizing a photoacid generator. Also, different functional blocks can be selected rather than PtBA for different applications, such as UV-degradable block poly(methyl methacrylate) (PMMA), high etch resistance block polydimethylsiloxane (PDMS) or ionic conducting block polystyrenesulfonate (PSS).

Finally, an efficient approach for well ordered organic/metal hybrid materials with ultra-high NP content was presented. This method used small molecule additives, tartaric acid, that can hydrogen bond with one segment of the block copolymer host and the nanoparticle ligands to increase the NP loading limit while maintaining the ordered structure of the system. The functions of the nanoparticle are three folds: introducing favorable enthalpic interactions, enhancing the segregation strength, and alleviating the entropic penalties for NP incorporation. We note here that this method provides advantages for the practical fabrication of well-ordered functional hybrid nanomaterials through large-scale manufacturing, for example roll-to-roll coating. Free standing gold lines could also be created by transferring this method from a bulk system into thin films, which would be an ideal approach for a variety of applications.

BIBLIOGRAPHY

1. Lopes, W. A.; Jaeger, H. M. *Nature* **2001,** 414, 735-738.

2. Thurn-Albrecht, T.; Schotter, J.; Kästle, G. A.; Emley, N.; Shibauchi, T.; Krusin-Elbaum, L.; Guarini, K.; Black, C. T.; Tuominen, M. T.; Russell, T. P. *Science* **2000,** 290, 2126-2129.

3. Hamley, I. W. *Angew. Chem. Int. Ed.* **2003,** 42, 1692-1712.

4. Lazzari, M.; López-Quintela, M. A. *Adv. Mater.* **2003,** 15, 1583-1594.

5. Hawker, C. J.; Russell, T. P. *MRS Bull.* **2005,** 30, 952-966.

6. Park, M.; Harrison, C.; Chaikin, P. M.; Register, R. A.; Adamson, D. H. *Science* **1997,** 276, 1401-1404.

7. Cheng, J. Y.; Ross, C. A.; Smith, H. I.; Thomas, E. L. *Adv. Mater.* **2006,** 18, 2505-2521.

8. Stoykovich, M. P.; Nealey, P. F. *Mater. Today* **2006,** 9, 20-29.

9. Bates, F. S. *Science* **1991,** 251, 898-905.

10. Niu, S.; Saraf, R. F. *Macromolecules* **2003,** 36, 2428-2440.

11. Kim, S. H.; Misner, M. J.; Xu, T.; Kimura, M.; Russell, T. P. *Adv. Mater.* **2004,** 16, 226-231.

12. Kim, S.; Briber, R. M.; Karim, A.; Jones, R. L.; Kim, H. C. *Macromolecules* **2007,** 40, 4102-4105.

13. Bang, J.; Kim, B. J.; Stein, G. E.; Russell, T. P.; Li, X.; Wang, J.; Kramer, E. J.; Hawker, C. J. *Macromolecules* **2007,** 40, 7019-7025.

14. van Zoelen, W.; Asumaa, T.; Ruokolainen, J.; Ikkala, O.; ten Brinke, G. *Macromolecules* **2008,** 41, 3199-3208.

15. Phillip, W. A.; Hillmyer, M. A.; Cussler, E. L. *Macromolecules* **2010,** 43, 7763-7770.

16. Albert, J. N. L.; Bogart, T. D.; Lewis, R. L.; Beers, K. L.; Fasolka, M. J.; Hutchison, J. B.; Vogt, B. D.; Epps, T. H. *Nano Lett.* **2011,** 11, 1351-1357.

17. Morkved, T. L.; Lu, M.; Urbas, A. M.; Ehrichs, E. E.; Jaeger, H. M.; Mansky, P.; Russell, T. P. *Science* **1996,** 273, 931-933.

18. Ashok, B.; Muthukumar, M.; Russell, T. P. *J. Chem. Phys.* **2001,** 115, 1559-1564.

19. Xu, T.; Zhu, Y.; Gido, S. P.; Russell, T. P. *Macromolecules* **2004,** 37, 2625-2629.

20. Lyakhova, K. S.; Zvelindovsky, A. V.; Sevink, G. J. A. *Macromolecules* **2006,** 39, 3024-3037.

21. Kim, H.-C.; Park, S.-M.; Hinsberg, W. D. *Chem. Rev.* **2009,** 110, 146-177.

22. Hong, S. W.; Huh, J.; Gu, X.; Lee, D. H.; Jo, W. H.; Park, S.; Xu, T.; Russell, T. P. *Proc. Natl. Acad. Sci. USA* **2012,** 109, 1402-1406.

23. Park, S.; Lee, D. H.; Xu, J.; Kim, B.; Hong, S. W.; Jeong, U.; Xu, T.; Russell, T. P. *Science* **2009,** 323, 1030-1033.

24. Cheng, J. Y.; Mayes, A. M.; Ross, C. A. *Nat. Mater.* **2004,** 3, 823-828.

25. Sundrani, D.; Darling, S. B.; Sibener, S. J. *Nano Lett.* **2003,** 4, 273-276.

26. Sundrani, D.; Darling, S. B.; Sibener, S. J. *Langmuir* **2004,** 20, 5091-5099.

27. Sundrani, D.; Sibener, S. J. *Macromolecules* **2002,** 35, 8531-8539.

28. Park, S. M.; Stoykovich, M. P.; Ruiz, R.; Zhang, Y.; Black, C. T.; Nealey, P. F. *Adv. Mater.* **2007,** 19, 607-611.

29. Ruiz, R.; Ruiz, N.; Zhang, Y.; Sandstrom, R. L.; Black, C. T. *Adv. Mater.* **2007,** 19, 2157-2162.

30. Son, J. G.; Hannon, A. F.; Gotrik, K. W.; Alexander-Katz, A.; Ross, C. A. *Adv. Mater.* **2011,** 23, 634-639.

31. Xu, J.; Russell, T. P.; Ocko, B. M.; Checco, A. *Soft Matter* **2011,** 7, 3915-3919.

32. Russell, T. P.; Coulon, G.; Deline, V. R.; Miller, D. C. *Macromolecules* **1989,** 22, 4600-4606.

33. Green, P. F.; Christensen, T. M.; Russell, T. P. *Macromolecules* **1991,** 24, 252-255.

34. Smith, A. P.; Sehgal, A.; Douglas, J. F.; Karim, A.; Amis, E. J. *Macromol. Rapid. Commun.* **2003,** 24, 131-135.

35. Han, E.; Stuen, K. O.; Leolukman, M.; Liu, C.-C.; Nealey, P. F.; Gopalan, P. *Macromolecules* **2009,** 42, 4896-4901.

36. Choi, S.; Kim, E.; Ahn, H.; Naidu, S.; Lee, Y.; Ryu, D. Y.; Hawker, C. J.; Russell, T. P. *Soft Matter.* **2012,** 8, 3463-3469.

37. Tirumala, V. R.; Daga, V.; Bosse, A. W.; Romang, A.; Ilavsky, J.; Lin, E. K.; Watkins, J. J. *Macromolecules* **2008,** 41, 7978-7985.

38. Tirumala, V. R.; Romang, A.; Agarwal, S.; Lin, E. K.; Watkins, J. J. *Adv. Mater.* **2008,** 20, 1603-1608.

39. Daga, V. K.; Watkins, J. J. *Macromolecules* **2010,** 43, 9990-9997.

40. Daga, V. K.; Anderson, E. R.; Gido, S. P.; Watkins, J. J. *Macromolecules* **2011,** 44, 6793-6799.

41. Lin, Y.; Daga, V. K.; Anderson, E. R.; Gido, S. P.; Watkins, J. J. *J. Am. Chem. Soc.* **2011,** 133, 6513-6516.

42. Ho, R.-M.; Chiang, Y.-W.; Tsai, C.-C.; Lin, C.-C.; Ko, B.-T.; Huang, B.-H. *J. Am. Chem. Soc.* **2004,** 126, 2704-2705.

43. Ho, R.-M.; Li, M.-C.; Lin, S.-C.; Wang, H.-F.; Lee, Y.-D.; Hasegawa, H.; Thomas, E. L. *J. Am. Chem. Soc.* **2012,** 134, 10974-10986.

44. Jinnai, H.; Kaneko, T.; Matsunaga, K.; Abetz, C.; Abetz, V. *Soft Matter* **2009,** 5, 2042-2046.

45. Zhu, Y.; Müller, T. E.; Lercher, J. A. *Adv. Funct. Mater.* **2008,** 18, 3427-3433.

46. Volksen, W.; Miller, R. D.; Dubois, G. *Chem. Rev.* **2009,** 110, 56-110.

47. Wang, Z.; Wang, H.; Mitra, A.; Huang, L.; Yan, Y. *Adv. Mater.* **2001,** 13, 746-749.

48. Seraji, S.; Wu, Y.; Forbess, M.; Limmer, S. J.; Chou, T.; Cao, G. Z. *Adv. Mater.* **2000,** 12, 1695-1698.

49. Baskaran, S.; Liu, J.; Domansky, K.; Kohler, N.; Li, X.; Coyle, C.; Fryxell, G. E.; Thevuthasan, S.; Williford, R. E. *Adv. Mater.* **2000,** 12, 291-294.

50. Crossland, E. J. W.; Nedelcu, M.; Ducati, C.; Ludwigs, S.; Hillmyer, M. A.; Steiner, U.; Snaith, H. J. *Nano Lett.* **2008,** 9, 2813-2819.

51. Crossland, E. J. W.; Kamperman, M.; Nedelcu, M.; Ducati, C.; Wiesner, U.; Smilgies, D. M.; Toombes, G. E. S.; Hillmyer, M. A.; Ludwigs, S.; Steiner, U.; Snaith, H. J. *Nano Lett.* **2008,** 9, 2807-2812.

52. Jose, R.; Thavasi, V.; Ramakrishna, S. *J. Am. Ceram. Soc.* **2009,** 92, 289-301.

53. O'Regan, B.; Gratzel, M. *Nature* **1991,** 353, 737-740.

54. Park, D.-H.; Nishiyama, N.; Egashira, Y.; Ueyama, K. *Ind. Eng. Chem. Res.* **2001,** 40, 6105-6110.

55. Guliants, V. V.; Carreon, M. A.; Lin, Y. S. *J. Membr. Sci.* **2004,** 235, 53-72.

56. Joo, J.; Shim, J.; Seo, H.; Jung, N.; Wiesner, U.; Lee, J.; Jeon, S. *Anal. Chem.* **2010,** 82, 3032-3037.

57. Ogawa, M.; Kuroda, K.; Mori, J.-i. *Chem. Commun.* **2000**, 2441.

58. Kageyama, K.; Tamazawa, J.-i.; Aida, T. *Science* **1999,** 285, 2113-2115.

59. Liu, A. M.; Hidajat, K.; Kawi, S.; Zhao, D. Y. *Chem. Commun.* **2000**, 1145-1146.

60. Nooney, R. I.; Kalyanaraman, M.; Kennedy, G.; Maginn, E. J. *Langmuir* **2000,** 17, 528-533.

61. Liu, X.; Wang, R.; Xia, Y.; He, Y.; Zhang, T. *Sens. Lett.* **2011,** 9, 698-702.

62. Domansky, K.; Liu, J.; Wang, L.-Q.; Engelhard, M. H.; Baskaran, S. *J. Mater. Res.* **2001,** 16, 2810-2816.

63. Gomez-Vega, J. M.; Iyoshi, M.; Kim, K. Y.; Hozumi, A.; Sugimura, H.; Takai, O. *Thin Solid Films* **2001,** 398-399, 615-620.

64. Wang, X.-P.; Li, X.; Onuma, K.; Ito, A.; Sogo, Y.; Kosuge, K.; Oyane, A. *J. Mater. Chem.* **2010,** 20, 6437-6445.

65. Li, X.; Wang, X.; He, D.; Shi, J. *J. Mater. Chem.* **2008,** 18.

66. Alberius, P. C. A.; Frindell, K. L.; Hayward, R. C.; Kramer, E. J.; Stucky, G. D.; Chmelka, B. F. *Chem. Mater.* **2002,** 14, 3284-3294.

67. Bagshaw, S. A.; Prouzet, E.; Pinnavaia, T. J. *Science* **1995,** 269, 1242.

68. Attard, G. S.; Glyde, J. C.; Goltner, C. G. *Nature* **1995,** 378, 366-368.

69. Templin, M.; Franck, A.; Du Chesne, A.; Leist, H.; Zhang, Y.; Ulrich, R.; Schadler, V.; Wiesner, U. *Science* **1997,** 278, 1795.

70. Dongyuan, Z.; Chmelka, B. F.; Stucky, G. D. *Science* **1998,** 279, 548.

71. Lu, Y.; Fan, H.; Stump, A.; Ward, T. L.; Rieker, T.; Brinker, C. J. *Nature* **1999,** 398, 223.

72. Göltner, C. G.; Henke, S.; Weissenberger, M. C.; Antonietti, M. *Angew. Chem. Int. Ed.* **1998,** 37, 613-616.

73. Honma, I.; Zhou, H. S.; Kundu, D.; Endo, A. *Adv. Mater.* **2000,** 12, 1529-1533.

74. Klotz, M.; Ayral, A.; Guizard, C.; Cot, L. *J. Mater. Chem.* **2000,** 10.

75. Deng, Y.; Yu, T.; Wan, Y.; Shi, Y.; Meng, Y.; Gu, D.; Zhang, L.; Huang, Y.; Liu, C.; Wu, X.; Zhao, D. *J. Am. Chem. Soc.* **2007,** 129, 1690-1697.

76. Huang, L.; Yan, X.; Kruk, M. *Langmuir* **2010,** 26, 14871-14878.

77. Ma, G.; Yan, X.; Li, Y.; Xiao, L.; Huang, Z.; Lu, Y.; Fan, J. *J. Am. Chem. Soc.* **2010,** 132, 9596-9597.

78. Chen, L.; Zhu, G.; Zhang, D.; Zhao, H.; Guo, M.; Shi, W.; Qiu, S. *J. Mater. Chem.* **2009,** 19, 2013-2017.

79. Boissiere, C.; Grosso, D.; Chaumonnot, A.; Nicole, L.; Sanchez, C. *Advanced Materials* **2011,** 23, 599-623.

80. Guillemot, F.; Brunet-Bruneau, A.; Bourgeat-Lami, E.; Gacoin, T.; Barthel, E.; Boilot, J. P. *Chemistry of Materials* **2010,** 22, 2822-2828.

81. Rühle, B.; Davies, M.; Lebold, T.; Bräuchle, C.; Bein, T. *ACS Nano* **2012,** 6, 1948-1960.

82. Fan, R.; Huh, S.; Yan, R.; Arnold, J.; Yang, P. *Nat Mater* **2008,** 7, 303-307.

83. Kirstein, J.; Platschek, B.; Jung, C.; Brown, R.; Bein, T.; Brauchle, C. *Nat Mater* **2007,** 6, 303-310.

84. Wu, C.-W.; Ohsuna, T.; Edura, T.; Kuroda, K. *Angewandte Chemie International Edition* **2007,** 46, 5364-5368.

85. Pai, R. A.; Humayun, R.; Schulberg, M. T.; Sengupta, A.; Sun, J.-N.; Watkins, J. J. *Science* **2004,** 303, 507-510.

86. Pai, R. A.; Watkins, J. J. *Adv. Mater.* **2006,** 18, 241-245.

87. Gupta, R. R.; RamachandraRao, V. S.; Watkins, J. J. *Macromolecules* **2003,** 36, 1295-1303.

88. Gupta, R. R.; Lavery, K. A.; Francis, T. J.; Webster, J. R. P.; Smith, G. S.; Russell, T. P.; Watkins, J. J. *Macromolecules* **2002,** 36, 346-352.

89. Nagarajan, S.; Li, M.; Pai, R. A.; Bosworth, J. K.; Busch, P.; Smilgies, D. M.; Ober, C. K.; Russell, T. P.; Watkins, J. J. *Adv. Mater.* **2008,** 20, 246-251.

90. Chen, H.-T.; Crosby, T. A.; Park, M.-H.; Nagarajan, S.; Rotello, V. M.; Watkins, J. J. *J. Mater. Chem.* **2009,** 19, 70-74.

91. Nagarajan, S.; Bosworth, J. K.; Ober, C. K.; Russell, T. P.; Watkins, J. J. *Chem. Mater.* **2007,** 20, 604-606.

92. Nagarajan, S.; Russell, T. P.; Watkins, J. J. *Advanced Functional Materials* **2009,** 19, 2728-2734.

93. Davis, K. A.; Charleux, B.; Matyjaszewski, K. *J. Polym. Sci. A Polym. Chem.* **2000,** 38, 2274-2283.

94. Romang, A. H.; Watkins, J. J. *Chemical Reviews* **2009,** 110, 459-478.

95. Tirumala, V. R.; Pai, R. A.; Agarwal, S.; Testa, J. J.; Bhatnagar, G.; Romang, A. H.; Chandler, C.; Gorman, B. P.; Jones, R. L.; Lin, E. K.; Watkins, J. J. *Chemistry of Materials* **2007,** 19, 5868-5874.

96. Lynd, N. A.; Meuler, A. J.; Hillmyer, M. A. *Prog. Polym. Sci.* **2008,** 33, 875-893.

97. Sides, S. W.; Fredrickson, G. H. *J. Chem. Phys.* **2004,** 121, 4974-4986.

98. Cooke, D. M.; Shi, A.-C. *Macromolecules* **2006,** 39, 6661-6671.

99. van Dijk, M. A.; van den Berg, R. *Macromolecules* **1995,** 28, 6773-6778.

100. Suh, K. Y.; Kim, Y. S.; Lee, H. H. *J. Chem. Phys.* **1998,** 108, 1253-1256.

101. Matsen, M. W.; Bates, F. S. *Macromolecules* **1996,** 29, 1091-1098.

102. Semenov, A. N. *Macromolecules* **1989,** 22, 2849-2851.

103. Matsen, M. W.; Bates, F. S. *J. Chem. Phys.* **1997,** 106, 2436.

104. Sakamoto, N.; Hashimoto, T.; Han, C. D.; Kim, D.; Vaidya, N. Y. *Macromolecules* **1997,** 30, 1621.

105. Sakamoto, N.; Hashimoto, T. *Macromolecules* **1998,** 31, 8493.

106. Dormidontova, E. E.; Lodge, T. P. *Macromolecules* **2001,** 34, 9143.

107. Huang, Y.-Y.; Hsu, J.-Y.; Chen, H.-L.; Hashimoto, T. *Macromolecules* **2007,** 40, 406-409.

108. Lodge, T. P.; Bang, J.; Park, M. J.; Char, K. *Phys. Rev. Lett.* **2004,** 92, 145501.

109. Matsen, M. W. *Journal of Physics: Condensed Matter* **2002,** 14, R21.

110. Wu, K. C. W.; Jiang, X.; Yamauchi, Y. *J. Mater. Chem.* **2011,** 21, 8934-8939.

111. Fukuoka, A.; Miyata, H.; Kuroda, K. *Chem. Commun.* **2003**, 284-285.

112. Molenkamp, W. C.; Watanabe, M.; Miyata, H.; Tolbert, S. H. *J. Am. Chem. Soc.* **2004,** 126, 4476-4477.

113. Martini, I. B.; Craig, I. M.; Molenkamp, W. C.; Miyata, H.; Tolbert, S. H.; Schwartz, B. J. *Nat. Nanotechnol.* **2007,** 2, 647-652.

114. Tolbert, S. H.; Firouzi, A.; Stucky, G. D.; Chmelka, B. F. *Science* **1997,** 278, 264-268.

115. Hillhouse, H. W.; Okubo, T.; van, E. J. W.; Tsapatsis, M. *Chem. Mater.* **1997,** 9, 1505-1507.

116. Walcarius, A.; Sibottier, E.; Etienne, M.; Ghanbaja, J. *Nat. Mater.* **2007,** 6, 602-608.

117. Miyata, H.; Kuroda, K. *J. Am. Chem. Soc.* **1999,** 121, 7618-7624.

118. Suzuki, T.; Kanno, Y.; Morioka, Y.; Kuroda, K. *Chem. Commun.* **2008**, 3284-3286.

119. Yang, H.; Kuperman, A.; Coombs, N.; Mamiche-Afara, S.; Ozin, G. A. *Nature* **1996,** 379, 703-5.

120. Miyata, H.; Kuroda, K. *Chem. Mater.* **2000,** 12, 49-54.

121. Miyata, H.; Noma, T.; Watanabe, M.; Kuroda, K. *Chem. Mater.* **2002,** 14, 766-772.

122. Miyata, H. *Microporous Mesoporous Mater.* **2007,** 101, 296-302.

123. Su, B.; Lu, X.; Lu, Q. *J. Am. Chem. Soc.* **2008,** 130, 14356-14357.

124. Kim, H.-C.; Park, S.-M.; Hinsberg, W. D. *Chem. Rev.* **2010,** 110, 146-177.

125. Sundrani, D.; Darling, S. B.; Sibener, S. J. *Nano Lett.* **2004,** 4, 273-276.

126. Park, S.; Lee, D. H.; Xu, J.; Kim, B.; Hong, S. W.; Jeong, U.; Xu, T.; Russell, T. P. *Science* **2009,** 323, 1030-1033.

127. Cheng, J. Y.; Mayes, A. M.; Ross, C. A. *Nat. Mater.* **2004,** 3, 823-828.

128. Stoykovich, M. P.; Muller, M.; Kim, S. O.; Solak, H. H.; Edwards, E. W.; de Pablo, J. J.; Nealey, P. F. *Science* **2005,** 308, 1442-1446.

129. Xu, J.; Park, S.; Wang, S.; Russell, T. P.; Ocko, B. M.; Checco, A. *Adv. Mater.* **2010,** 22, 2268-2272.

130. Ouk Kim, S.; Solak, H. H.; Stoykovich, M. P.; Ferrier, N. J.; de Pablo, J. J.; Nealey, P. F. *Nature* **2003,** 424, 411-414.

131. Sundrani, D.; Darling, S. B.; Sibener, S. J. *Langmuir* **2004,** 20, 5091-5099.

132. Sundrani, D.; Sibener, S. J. *Macromolecules* **2002,** 35, 8531-8539.

133. Park, S.-M.; Stoykovich, M. P.; Ruiz, R.; Zhang, Y.; Black, C. T.; Nealey, P. F. *Adv. Mater.* **2007,** 19, 607-611.

134. Ruiz, R.; Ruiz, N.; Robert, Y. Z.; Sandstrom, L.; Black, C. T. *Adv. Mater.* **2007,** 19, 2157-2162.

135. Son, J. G.; Hannon, A. F.; Gotrik, K. W.; Alexander-Katz, A.; Ross, C. A. *Adv. Mater.* **2011,** 23, 634-639.

136. Kim, S. O.; Solak, H. H.; Stoykovich, M. P.; Ferrier, N. J.; de, P. J. J.; Nealey, P. F. *Nature* **2003,** 424, 411-414.

137. Stoykovich, M. P.; Mueller, M.; Kim, S. O.; Solak, H. H.; Edwards, E. W.; de, P. J. J.; Nealey, P. F. *Science* **2005,** 308, 1442-1446.

138. Ruiz, R.; Kang, H.; Detcheverry, F. A.; Dobisz, E.; Kercher, D. S.; Albrecht, T. R.; de, P. J. J.; Nealey, P. F. *Science* **2008,** 321, 936-939.

139. Yan, M.; Gibaud, A. *Journal of Applied Crystallography* **2007,** 40, 1050-1055.

140. Rueda, D. R.; Martín-Fabiani, I.; Soccio, M.; Alayo, N.; Pérez-Murano, F.; Rebollar, E.; García-Gutiérrez, M. C.; Castillejo, M.; Ezquerra, T. A. *Journal of Applied Crystallography* **2012,** 45, 1038-1045.

141. Singh, G.; Yager, K. G.; Berry, B.; Kim, H.-C.; Karim, A. *ACS Nano* **2012,** 6, 10335-10342.

142. Tang, C.; Tracz, A.; Kruk, M.; Zhang, R.; Smilgies, D.-M.; Matyjaszewski, K.; Kowalewski, T. *J. Am. Chem. Soc.* **2005,** 127, 6918-6919.

143. Guliants, V. V.; Carreon, M. A.; Lin, Y. S. *J. Membr. Sci.* **2004,** 235, 53-72.

144. Park, D.-H.; Nishiyama, N.; Egashira, Y.; Ueyama, K. *Ind. Eng. Chem. Res.* **2001,** 40, 6105-6110.

145. Chen, H.-T.; Crosby, T. A.; Park, M.-H.; Nagarajan, S.; Rotello, V. M.; Watkins, J. J. *J. Mater. Chem.* **2009,** 19, 70-74.

146. Crossland, E. J. W.; Nedelcu, M.; Ducati, C.; Ludwigs, S.; Hillmyer, M. A.; Steiner, U.; Snaith, H. J. *Nano Lett.* **2009,** 9, 2813-2819.

147. Crossland, E. J. W.; Kamperman, M.; Nedelcu, M.; Ducati, C.; Wiesner, U.; Smilgies, D.-M.; Toombes, G. E. S.; Hillmyer, M. A.; Ludwigs, S.; Steiner, U.; Snaith, H. J. *Nano Lett.* **2009,** 9, 2807-2812.

148. Duan, C.; Majumdar, A. *Nat Nano* **2010,** 5, 848-852.

149. Gomez-Vega, J. M.; Iyoshi, M.; Kim, K. Y.; Hozumi, A.; Sugimura, H.; Takai, O. *Thin Solid Films* **2001,** 398-399, 615-620.

150. Wang, X.-P.; Li, X.; Onuma, K.; Ito, A.; Sogo, Y.; Kosuge, K.; Oyane, A. *J. Mater. Chem.* **2010,** 20, 6437-6445.

151. Fasolka, M. J.; Mayes, A. M. *Annual Review of Materials Research* **2001,** 31, 323-355.

152. Park, C.; Yoon, J.; Thomas, E. L. *Polymer* **2003,** 44, 6725-6760.

153. Krausch, G.; Magerle, R. *Advanced Materials* **2002,** 14, 1579-1583.

154. Hawker, C. J.; T.P.Russell. *MRS Bull* **2005,** 30, 952.

155. Li, M.; Coenjarts, C. A.; Ober, C. K. *Adv. Polym. Sci.* **2005,** 190, 183-226.

156. Yao, L.; Woll, A. R.; Watkins, J. J. *Macromolecules* **2013**.

157. Bates, F. S. *Science* **1991,** 251, 898-905.

158. Chan, V. Z.-H.; Hoffman, J.; Lee, V. Y.; Iatrou, H.; Avgeropoulos, A.; Hadjichristidis, N.; Miller, R. D.; Thomas, E. L. *Science* **1999,** 286, 1716-1719.

159. Urade, V. N.; Wei, T.-C.; Tate, M. P.; Kowalski, J. D.; Hillhouse, H. W. *Chem. Mater.* **2007,** 19, 768-777.

160. Hayward, R. C.; Alberius, P. C. A.; Kramer, E. J.; Chmelka, B. F. *Langmuir* **2004,** 20, 5998-6004.

161. Davis, K. A.; Charleux, B.; Matyjaszewski, K. *Journal of Polymer Science Part A: Polymer Chemistry* **2000,** 38, 2274-2283.

162. Zhou, S.; Chu, B. *Macromolecules* **1998,** 31, 7746-7755.

163. Buhler, E.; Dobrynin, A. V.; DeSimone, J. M.; Rubinstein, M. *Macromolecules* **1998,** 31, 7347-7355.

164. Cavicchi, K. A.; Berthiaume, K. J.; Russell, T. P. *Polymer* **2005,** 46, 11635-11639.

165. Alfredsson, V.; Anderson, M. W. *Chem. Mater.* **1996,** 8, 1141-6.

166. Monnier, A.; Schuth, F.; Huo, Q.; Kumar, D.; Margolese, D.; Maxwell, R. S.; Stucky, G. D.; Krishnamurty, M.; Petroff, P.; et, a. *Science* **1993,** 261, 1299-303.

167. Vartuli, J. C.; Schmitt, K. D.; Kresge, C. T.; Roth, W. J.; Leonowicz, M. E.; McCullen, S. B.; Hellring, S. D.; Beck, J. S.; Schlenker, J. L.; et, a. *Chem. Mater.* **1994,** 6, 2317-26.

168. Lee, B.; Park, I.; Yoon, J.; Park, S.; Kim, J.; Kim, K.-W.; Chang, T.; Ree, M. *Macromolecules* **2005,** 38, 4311-4323.

169. Jin, S.; Yoon, J.; Heo, K.; Park, H. W.; Kim, J.; Kim, K. W.; Shin, T. J.; Chang, T.; Ree, M. *J. Appl. Crystallogr.* **2007,** 40, 950-958.

170. Barber Jr, R. P.; Gomez, R. D.; Herman, W. N.; Romero, D. B. *Org. Electron.* **2006,** 7, 508-513.

171. Barrau, S.; Heiser, T.; Richard, F.; Brochon, C.; Ngov, C.; van de Wetering, K.; Hadziioannou, G.; Anokhin, D. V.; Ivanov, D. A. *Macromolecules* **2008,** 41, 2701-2710.

172. Yang, C.; Lee, J. K.; Heeger, A. J.; Wudl, F. *J. Mater. Chem.* **2009,** 19, 5416-5423.

173. Urbas, A.; Sharp, R.; Fink, Y.; Thomas, E. L.; Xenidou, M.; Fetters, L. J. *Adv. Mater.* **2000,** 12, 812-814.

174. Urbas, A.; Fink, Y.; Thomas, E. L. *Macromolecules* **1999,** 32, 4748-4750.

175. Daga, V. K.; Schwartz, E. L.; Chandler, C. M.; Lee, J.-K.; Lin, Y.; Ober, C. K.; Watkins, J. J. *Nano Lett.* **2011,** 11, 1153-1160.

176. Morikawa, Y.; Kondo, T.; Nagano, S.; Seki, T. *Chem. Mater.* **2007,** 19, 1540-1542.

177. Chen, W.; Wang, J.-Y.; Zhao, W.; Li, L.; Wei, X.; Balazs, A. C.; Matyjaszewski, K.; Russell, T. P. *J. Am. Chem. Soc.* **2011,** 133, 17217-17224.

178. Rosenhauer, R.; Fischer, T.; Stumpe, J.; Giménez, R.; Piñol, M.; Serrano, J. L.; Viñuales, A.; Broer, D. *Macromolecules* **2005,** 38, 2213-2222.

179. Yu, H.; Iyoda, T.; Ikeda, T. *J. Am. Chem. Soc.* **2006,** 128, 11010-11011.

180. Morikawa, Y.; Nagano, S.; Watanabe, K.; Kamata, K.; Iyoda, T.; Seki, T. *Adv. Mater.* **2006,** 18, 883-886.

181. Tran-Cong-Miyata, Q.; Nishigami, S.; Ito, T.; Komatsu, S.; Norisuye, T. *Nat. Mater.* **2004,** 3, 448-451.

182. Inoue, K.; Komatsu, S.; Trinh, X.-A.; Norisuye, T.; Tran-Cong-Miyata, Q. *J. Polym. Sci., Part B: Polym. Phys.* **2005,** 43, 2898-2913.

183. Trinh, X.-A.; Fukuda, J.; Adachi, Y.; Nakanishi, H.; Norisuye, T.; Tran-Cong-Miyata, Q. *Macromolecules* **2007,** 40, 5566-5574.

184. Lestel, L.; Guegan, P.; Boileau, S.; Cheradame, H.; Laupretre, F. *Macromolecules* **1992,** 25, 6024-8.

185. Cypcar, C. C.; Camelio, P.; Lazzeri, V.; Mathias, L. J.; Waegell, B. *Macromolecules* **1996,** 29, 8954-8959.

186. Ruokolainen, J.; Mäkinen, R.; Torkkeli, M.; Mäkelä, T.; Serimaa, R.; Brinke, G. t.; Ikkala, O. *Science* **1998,** 280, 557-560.

187. Ruokolainen, J.; Saariaho, M.; Ikkala, O.; ten Brinke, G.; Thomas, E. L.; Torkkeli, M.; Serimaa, R. *Macromolecules* **1999,** 32, 1152-1158.

188. Bondzic, S.; de Wit, J.; Polushkin, E.; Schouten, A. J.; ten Brinke, G.; Ruokolainen, J.; Ikkala, O.; Dolbnya, I.; Bras, W. *Macromolecules* **2004,** 37, 9517-9524.

189. Epps, T. H.; Bailey, T. S.; Waletzko, R.; Bates, F. S. *Macromolecules* **2003,** 36, 2873-2881.

190. Epps, T. H.; Bailey, T. S.; Pham, H. D.; Bates, F. S. *Chem. Mater.* **2002,** 14, 1706-1714.

191. Santagata, N. M.; Lakhani, A. M.; Davis, B. F.; Luo, P.; Buongiorno Nardelli, M.; Pearl, T. P. *J. Phys. Chem. C* **2010,** 114, 8917-8925.

192. Ito, H. *Adv. Polym. Sci.* **2005,** 172, 37-245.

193. Hinsberg, W.; Houle, F.; Wallraff, G.; Sanchez, M.; Morrison, M.; Hoffnagle, J.; Ito, H.; Nguyen, C.; Larson, C. E.; Brock, P. J.; Breyta, G. *J. Photopolym. Sci. Technol.* **1999,** 12, 649-662.

194. Hinsberg, W. D.; Houle, F. A.; Sanchez, M. I.; Wallraff, G. M. *IBM J. Res. Dev.* **2001,** 45, 667-681.

195. Houle, F. A.; Hinsberg, W. D.; Morrison, M.; Sanchez, M. I.; Wallraff, G.; Larson, C.; Hoffnagle, J. *J. Vac. Sci. Technol. B* **2000,** 18, 1874-1885.

196. Houle, F. A.; Hinsberg, W. D.; Sanchez, M. I.; Hoffnagle, J. A. *J. Vac. Sci. Technol. B* **2002,** 20, 924-931.

197. Michaelson, T. B.; Pawloski, A. R.; Acheta, A.; Nishimura, Y.; Willson, C. G. *Proc. SPIE* **2005**, 368-379.

198. Houle, F. A.; Hinsberg, W. D.; Sanchez, M. I. *J. Vac. Sci. Technol. B* **2004,** 22, 747-757.

199. Li, M.; Schnablegger, H.; Mann, S. *Nature* **1999,** 402, 393-395.

200. Zeng, H.; Li, J.; Liu, J. P.; Wang, Z. L.; Sun, S. H. *Nature* **2002,** 420, 395-398.

201. Kotov, N. A.; Dekany, I.; Fendler, J. H. *J. Phys. Chem.* **1995,** 99, 13065-13069.

202. Claridge, S. A.; Mastroianni, A. J.; Au, Y. B.; Liang, H. W.; Micheel, C. M.; Frechet, J. M. J.; Alivisatos, A. P. *J. Am. Chem. Soc.* **2008,** 130, 9598-9605.

203. Shevchenko, E. V.; Kortright, J. B.; Talapin, D. V.; Aloni, S.; Alivisatos, A. P. *Adv. Mater.* **2007,** 19, 4183-4188.

204. Westcott, S. L.; Oldenburg, S. J.; Lee, T. R.; Halas, N. J. *Langmuir* **1998,** 14, 5396-5401.

205. Lu, W.; Lieber, C. M. *J. Phys. D-Appl. Phys.* **2006,** 39, R387-R406.

206. Cui, Y.; Lieber, C. M. *Science* **2001,** 291, 851-853.

207. Huang, Y.; Duan, X. F.; Wei, Q. Q.; Lieber, C. M. *Science* **2001,** 291, 630-633.

208. Javey, A.; Nam, S.; Friedman, R. S.; Yan, H.; Lieber, C. M. *Nano Lett.* **2007,** 7, 773-777.

209. Briseno, A. L.; Mannsfeld, S. C. B.; Reese, C.; Hancock, J. M.; Xiong, Y.; Jenekhe, S. A.; Bao, Z.; Xia, Y. N. *Nano Lett.* **2007,** 7, 2847-2853.

210. Briseno, A. L.; Mannsfeld, S. C. B.; Jenekhe, S. A.; Bao, Z.; Xia, Y. N. *Mater. Today* **2008,** 11, 38-47.

211. Rivest, J. B.; Swisher, S. L.; Fong, L. K.; Zheng, H. M.; Alivisatos, A. P. *ACS Nano* **2011,** 5, 3811-3816.

212. Colfen, H.; Mann, S. *Angew. Chem. Int. Edit.* **2003,** 42, 2350-2365.

213. Pacholski, C.; Kornowski, A.; Weller, H. *Angew. Chem. Int. Edit.* **2002,** 41, 1188-1191.

214. Baker, J. L.; Widmer-Cooper, A.; Toney, M. F.; Geissler, P. L.; Alivisatos, A. P. *Nano Lett.* **2010,** 10, 195-201.

215. Barrena, E.; Zhang, X. N.; Mbenkum, B. N.; Lohmueller, T.; Krauss, T. N.; Kelsch, M.; van Aken, P. A.; Spatz, J. P.; Dosch, H. *ChemPhysChem* **2008,** 9, 1114-1116.

216. Fan, S. S.; Chapline, M. G.; Franklin, N. R.; Tombler, T. W.; Cassell, A. M.; Dai, H. J. *Science* **1999,** 283, 512-514.

217. Dai, H. J. *Accounts Chem. Res.* **2002,** 35, 1035-1044.

218. Reches, M.; Gazit, E. *Science* **2003,** 300, 625-627.

219. Bong, D. T.; Clark, T. D.; Granja, J. R.; Ghadiri, M. R. *Angew. Chem. Int. Edit.* **2001,** 40, 988-1011.

220. Park, S.; Lim, J. H.; Chung, S. W.; Mirkin, C. A. *Science* **2004,** 303, 348-351.

221. Macak, J. M.; Tsuchiya, H.; Taveira, L.; Aldabergerova, S.; Schmuki, P. *Angew. Chem. Int. Edit.* **2005,** 44, 7463-7465.

222. Richard, C.; Balavoine, F.; Schultz, P.; Ebbesen, T. W.; Mioskowski, C. *Science* **2003,** 300, 775-778.

223. Chen, Q.; Bae, S. C.; Granick, S. *Nature* **2011,** 469, 381-384.

224. Yan, J.; Bloom, M.; Bae, S. C.; Luijten, E.; Granick, S. *Nature* **2012,** 491, 578-581.

225. Freeman, R. G.; Grabar, K. C.; Allison, K. J.; Bright, R. M.; Davis, J. A.; Guthrie, A. P.; Hommer, M. B.; Jackson, M. A.; Smith, P. C.; Walter, D. G.; Natan, M. J. *Science* **1995,** 267, 1629-1632.

226. Glass, R.; Moller, M.; Spatz, J. P. *Nanotechnology* **2003,** 14, 1153-1160.

227. Kim, S. H.; Misner, M. J.; Xu, T.; Kimura, M.; Russell, T. P. *Adv. Mater.* **2004,** 16, 226-+.

228. Schmitt, A. L.; Mahanthappa, M. K. *Soft Matter* **2012,** 8, 2294-2303.

229. Widin, J. M.; Schmitt, A. K.; Schmitt, A. L.; Im, K.; Mahanthappa, M. K. *J. Am. Chem. Soc.* **2012,** 134, 3834-3844.

230. Valentine, J.; Zhang, S.; Zentgraf, T.; Ulin-Avila, E.; Genov, D. A.; Bartal, G.; Zhang, X. *Nature* **2008,** 455, 376-379.

231. Vignolini, S.; Yufa, N. A.; Cunha, P. S.; Guldin, S.; Rushkin, I.; Stefik, M.; Hur, K.; Wiesner, U.; Baumberg, J. J.; Steiner, U. *Adv. Mater.* **2012,** 24, OP23-OP27.

232. Yashima, E.; Maeda, K.; Iida, H.; Furusho, Y.; Nagai, K. *Chem. Rev.* **2009,** 109, 6102-6211.

233. Hoshikawa, N.; Yamamoto, C.; Hotta, Y.; Okamoto, Y. *Polym. J* **2006,** 38, 1258-1266.

234. Miyake, G. M.; Mariott, W. R.; Chen, E. Y. X. *J. Am. Chem. Soc.* **2007,** 129, 6724-6725.

235. Kamer, P. C. J.; Cleij, M. C.; Nolte, R. J. M.; Harada, T.; Hezemans, A. M. F.; Drenth, W. *J. Am. Chem. Soc.* **1988,** 110, 1581-1587.

236. Cornelissen, J.; Donners, J.; de Gelder, R.; Graswinckel, W. S.; Metselaar, G. A.; Rowan, A. E.; Sommerdijk, N.; Nolte, R. J. M. *Science* **2001,** 293, 676-680.

237. Nomura, R.; Fukushima, Y.; Nakako, H.; Masuda, T. *J. Am. Chem. Soc.* **2000,** 122, 8830-8836.

238. Pijper, D.; Feringa, B. L. *Soft Matter* **2008,** 4, 1349-1372.

239. Yashima, E.; Maeda, K.; Nishimura, T. *Chem.-Eur. J.* **2004,** 10, 42-51.

240. Inai, Y.; Tagawa, K.; Takasu, A.; Hirabayashi, T.; Oshikawa, T.; Yamashita, M. *J. Am. Chem. Soc.* **2000,** 122, 11731-11732.

241. Komori, H.; Inai, Y. *J. Phys. Chem. A* **2006,** 110, 9099-9107.

242. Ousaka, N.; Inai, Y. *J. Org. Chem.* **2009,** 74, 1429-1439.

243. Dupont, J.; Liu, G. J.; Niihara, K.; Kimoto, R.; Jinnai, H. *Angew. Chem. Int. Edit.* **2009,** 48, 6144-6147.

244. Cornelissen, J.; Fischer, M.; Sommerdijk, N.; Nolte, R. J. M. *Science* **1998,** 280, 1427-1430.

245. Malashkevich, V. N.; Kammerer, R. A.; Efimov, V. P.; Schulthess, T.; Engel, J. *Science* **1996,** 274, 761-765.

246. Li, C. Y.; Cheng, S. Z. D.; Ge, J. J.; Bai, F.; Zhang, J. Z.; Mann, I. K.; Chien, L. C.; Harris, F. W.; Lotz, B. *J. Am. Chem. Soc.* **2000,** 122, 72-79.

247. Yan, Y.; Yu, Z.; Huang, Y. W.; Yuan, W. X.; Wei, Z. X. *Adv. Mater.* **2007,** 19, 3353-3357.

248. Tirumala, V. R.; Romang, A.; Agarwal, S.; Lin, E. K.; Watkins, J. J. *Adv. Mater.* **2008,** 20, 1603-1608.

249. Lin, Y.; Daga, V. K.; Anderson, E. R.; Gido, S. P.; Watkins, J. J. *J. Am. Chem. Soc.* **2011,** 133, 6513-6516.

250. Wei, Q.; Lin, Y.; Anderson, E. R.; Briseno, A. L.; Gido, S. P.; Watkins, J. J. *ACS Nano* **2012,** 6, 1188-1194.

251. Yao, L.; Watkins, J. J. *ACS Nano* **2013,** 7, 1513-1523.

252. Santagata, N. M.; Lakhani, A. M.; Davis, B. F.; Luo, P.; Buongiorno Nardelli, M.; Pearl, T. P. *J. Phys. Chem. C* **2010,** 114, 8917-8925.

253. Zhao, W.; Liu, F.; Wei, X.; Chen, D.; Grason, G. M.; Russell, T. P. *Macromolecules* **2013,** 46, 474-483.

254. Zhao, W.; Chen, D.; Grason, G. M.; Russell, T. P. *Macromolecules* **2013,** 46, 455-462.

255. Boal, A. K.; Ilhan, F.; DeRouchey, J. E.; Thurn-Albrecht, T.; Russell, T. P.; Rotello, V. M. *Nature* **2000,** 404, 746-748.

256. Huynh, W. U.; Dittmer, J. J.; Alivisatos, A. P. *Science* **2002,** 295, 2425-2427.

257. Balazs, A. C.; Emrick, T.; Russell, T. P. *Science* **2006,** 314, 1107-1110.

258. Rancatore, B. J.; Mauldin, C. E.; Tung, S.-H.; Wang, C.; Hexemer, A.; Strzalka, J.; Fréchet, J. M. J.; Xu, T. *ACS Nano* **2010,** 4, 2721-2729.

259. Rosa, C. D.; Auriemma, F.; Girolamo, R. D.; Pepe, G. P.; Napolitano, T.; Scaldaferri, R. *Adv. Mater.* **2010,** 22, 5414-5419.

260. Lin, Y.; Wei, Q.; Qian, G.; Yao, L.; Watkins, J. J. *Macromolecules* **2012,** 45, 8665-8673.

261. Lu, G.; Li, L.; Yang, X. *Small* **2008,** 4, 601-606.

262. Kim, H.; Kobayashi, S.; AbdurRahim, M. A.; Zhang, M. J.; Khusainova, A.; Hillmyer, M. A.; Abdala, A. A.; Macosko, C. W. *Polymer* **2011,** 52, 1837-1846.

263. Zhang, K.; Wang, Y.; Hillmyer, M. A.; Francis, L. F. *Biomaterials* **2004,** 25, 2489-2500.

264. Gaines, M. K.; Smith, S. D.; Samseth, J.; Bockstaller, M. R.; Thompson, R. B.; Rasmussen, K. O.; Spontak, R. J. *Soft Matter* **2008,** 4, 1609-1612.

265. Kang, H.; Detcheverry, F. A.; Mangham, A. N.; Stoykovich, M. P.; Daoulas, K. C.; Hamers, R. J.; Müller, M.; de Pablo, J. J.; Nealey, P. F. *Phys. Rev. Lett.* **2008,** 100, 148303.

266. Chiu, J. J.; Kim, B. J.; Kramer, E. J.; Pine, D. J. *J. Am. Chem. Soc.* **2005,** 127, 5036-5037.

267. Costanzo, P. J.; Beyer, F. L. *Macromolecules* **2007,** 40, 3996-4001.

268. Chiu, J. J.; Kim, B. J.; Yi, G.-R.; Bang, J.; Kramer, E. J.; Pine, D. J. *Macromolecules* **2007,** 40, 3361-3365.

269. Matsen, M. W.; Thompson, R. B. *Macromolecules* **2008,** 41, 1853-1860.

270. Zou, S.; Hong, R.; Emrick, T.; Walker, G. C. *Langmuir* **2007,** 23, 1612-1614.

271. Kim, B. J.; Bang, J.; Hawker, C. J.; Kramer, E. J. *Macromolecules* **2006,** 39, 4108-4114.

272. Zhao, Y.; Thorkelsson, K.; Mastroianni, A. J.; Schilling, T.; Luther, J. M.; Rancatore, B. J.; Matsunaga, K.; Jinnai, H.; Wu, Y.; Poulsen, D.; Frechet, J. M. J.; Paul Alivisatos, A.; Xu, T. *Nature Mater.* **2009,** 8, 979-985.

273. Warren, S. C.; Messina, L. C.; Slaughter, L. S.; Kamperman, M.; Zhou, Q.; Gruner, S. M.; DiSalvo, F. J.; Wiesner, U. *Science* **2008,** 320, 1748-1752.

274. Noro, A.; Higuchi, K.; Sageshima, Y.; Matsushita, Y. *Macromolecules* **2012,** 45, 8013-8020.

275. Jang, S. G.; Khan, A.; Hawker, C. J.; Kramer, E. J. *Macromolecules* **2012,** 45, 1553-1561.

276. Jang, S. G.; Kramer, E. J.; Hawker, C. J. *J. Am. Chem. Soc.* **2011,** 133, 16986-16996.

277. Sarkar, B.; Alexandridis, P. *Langmuir* **2012,** 28, 15975-15986.

278. Brust, M.; Fink, J.; Bethell, D.; Schiffrin, D. J.; Kiely, C. *Chem. Commun.* **1995**, 1655-1656.